The Quantitative Analysis and Modification of Colloidal Nanoparticle Surfaces and Structures

John Andrew Ritchhart

A dissertation
submitted in partial fulfillment of the
requirements for the degree of

Doctor of Philosophy

University of Washington
2020

Reading Committee:
Brandi Cossairt, Chair
Daniel Gamelin
Dianne Xiao

Program Authorized to Offer Degree:
Chemistry

University of Washington

Abstract

The Quantitative Analysis and Modification of Colloidal Nanoparticle Surfaces and Structures

John Andrew Ritchhart

Chair of the Supervisory Committee:
Prof. Brandi M. Cossairt
Department of Chemistry

Nanoparticles have consumed the attention of inorganic and materials chemists for decades owing to both their tremendous breadth in composition, size, and shape, as well as the many exceptional physical and chemical properties which derive therefrom. Organic and metallic nanoparticles are exceptional classes of materials, but of particular interest to us are nanoparticles produced from semiconducting compositions. Nanoparticles derived from combinations of group II and VI or III and V elements on the sub 10 nm scale are commonly referred to as quantum dots (QDs). Quantum dots have attracted a great deal of attention as the result of potent emergent properties arising from their quantum scale as well as the many benefits and applications of solution processability. Quantum dot research has led to a generational advance in numerous

technologies and real-world applications including bio-sensing, catalysis, light harvesting, solid-state lighting, and displays. Continued development of the physicochemical properties of QDs promises a more technologically advanced and a greener future.

One of the most poorly understood and yet functionally-critical properties of nanomaterials is their surface. Surfaces of bulk materials do not appreciably contribute to most of the material's physical properties such as the band gap, absorptivity, or charge mobility. By contrast the surface of a nanoparticle is paramount to its physical as well as chemical properties. While size predominantly dictates the bandgap via the quantum confinement effect in QDs, the surface speciation ultimately decides charge trapping, transfer, solubility, and all manner of chemical reactivity. These varied implications of the surface represent both a responsibility and an opportunity to the chemist. The responsibility lies in identifying and characterizing the surface even though such measurements are often exceptionally difficult. However, if the surface can be well understood and controlled it holds the invaluable opportunity to tune the desired properties of the nanomaterial in ways not available through other means. Post-synthetic surface modification represents one of the most readily accessible and tractable methods for producing high-quality quantum dots with specific, engineered applications in mind. Our work in the Cossairt Lab has been exceptionally well poised to tackle this problem using atomistic and precise synthetic methodology.

Understanding the surface properties of quantum dots is also a critical step towards extending synthesis across length scales through the formation of mesocrystalline assemblies. Mesocrystals can be described as macroscopic pseudo-crystals and assemblies of nanomaterial units. Such assemblies offer not only another method of tuning the material properties, but a handle with which to create products for real-world problems that cannot be adequately solved by solution or amorphous film phases of matter. Just as the cytoplasm of a light harvesting plant cell contains a delicate assembly of countless microscopic components, future applications of quantum dots too must be built up from the nanoscale and incorporated into greater structures to extract their usefulness. By transcending the nanoscopic scale and engineering these structures across scales researchers can begin to tackle more problems with a greater degree of control and rational design. In order to achieve this though, one must simultaneously understand and control the critical interface of every nanoparticle: the surface.

In Chapter One of this thesis conceptualizations of nanoparticle surfaces will be reviewed in a greater detail. The discussion will be focused on II-VI and III-V materials, especially InP as it is the predominant focus of this body of work. An overview of mesocrystals and across length scale design will also be examined here. Chapter Two will focus on a quantitative investigation of ligand speciation and exchange at the surface of InP nanoparticles. This topic was thoroughly examined using atomically precise InP clusters and a combination of ^{1}H NMR and ^{31}P NMR spectroscopy as well in-situ SAXS via synchrotron. The controlled manipulation of InP surfaces is further examined in Chapter Three where manipulation of the nanoparticle surface is shown to give rise to control over nanoparticle crystal phase and growth profiles. Finally, Chapter Four will continue manipulations of the quantum dot surface towards the formation of mesocrystalline assemblies. Mechanisms of mesocrystalline material formation as well as preliminary applications towards photocatalysis will be discussed.

Table of Contents

List of Figures

List of Schemes

List of Tables

Chapter 1. A review of semiconductor nanoparticle surfaces

1.1 Introduction

Nanoparticles of all material compositions whether organic polymer, metal, semiconducting, or insulating exhibit changed properties that distinguish them as unique materials despite being compositionally identical to their respective bulk counterparts.[1–4] The common denominator and source of these differences is often the nanoparticle surface. Consider a uniform bulk, cubic crystal 1 μm in size, such a crystal would contain on the order of 1×10^{12} atoms and only 0.06% of those atoms would be distinctive surface atoms. By contrast sub 10 nm nanoparticles contain on the order of 100 to 1000 atoms with surface to volume ratios as high as 30%. This dramatic change in size and surface area causes extreme changes to practically all physical and chemical properties including changes in crystal structure, melting point, magnetism, charge mobilities, defect moieties, catalytic activity, and redox potentials.[5–9] In addition to altered properties it is the *emergent* properties of nanomaterials that have garnered a great deal of sustained interest, including the extreme electric field effects of metallic nanoparticles and the quantum confinement effects of semiconducting nanoparticles.[10,11]

Semiconducting materials are defined by their band gap, a 0.1 – 3.0 eV gap between the HOMO and the LUMO often arising from pairing cationic and anionic metal and non-metal atoms in their composition, e.g. Cd^{2+} and Se^{2-} forming CdSe or In^{3+} and P^{3-} forming InP. Upon electrical or photoexcitation, energetic electrons and holes in these materials characteristically give rise to excitons; these are coupled charge pairs that do not Coulombically recombine, similar in concept to the electron and nucleus of a hydrogen atom. The characteristic distance of this attraction differs between materials and is known as the Bohr exciton radius. In semiconducting nanoparticles when the particle radius is decreased below the Bohr radius the quantum confinement effect is observed (Figure 1.1). By confining the exciton wavefunction, the observed bandgap of a given material is steadily increased. Particles in this regime are subsequently referred to as quantum dots (QDs).

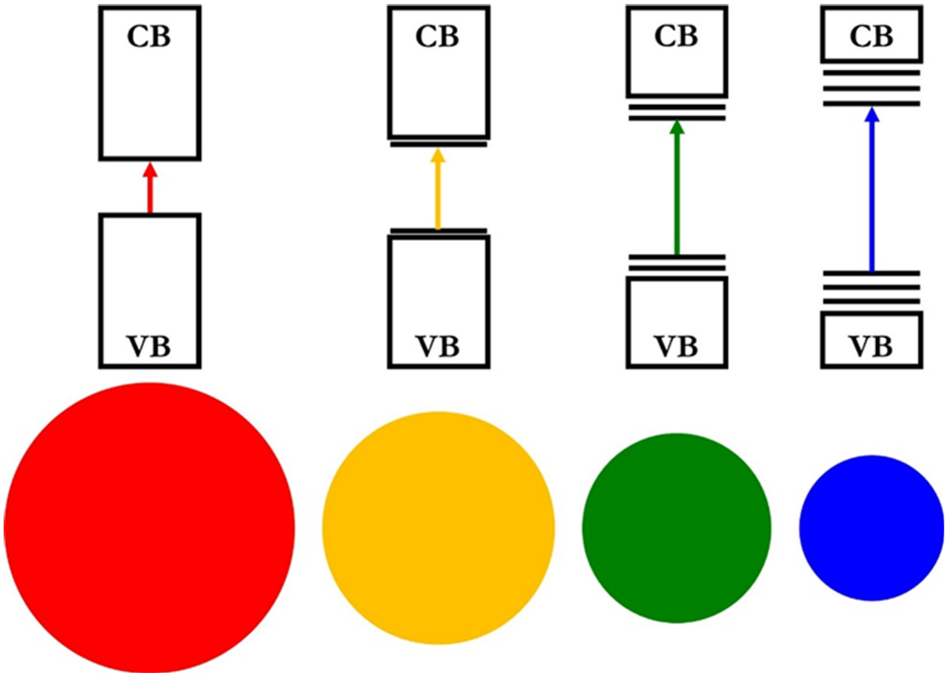

Figure 1.1. Effect of nanoparticle size on material band gap and intra-gap states as a result of the quantum confinement effect.

To fully understand the implications of this effect on a QD's chemical properties and behavior one must consider the effects of the surface. In a bulk semiconductor the small amount of surface atoms contributes negligibly to the QD's electronic properties, and in the absence of a junction, bulk electronic properties are well-described by pseudo-infinite Bloch molecular orbitals defined by the bulk structure.[12,13] In the nano-regime however, band edges are perturbed by the quantum confinement effect and under-coordinated surface atoms contribute intra-gap electronic states. Such states are the topic of a great deal of theoretical, spectroscopic, and crystallographic work.[8,14–16] These effects combine to cause the observable electronic and chemical behavior of a quantum dot to be inextricably tied to the nature of the surface. Quantitative understanding of a nanoparticle surface must be considered a prerequisite for any rational application of quantum dot science or technology.

1.2 Ligands and the atomistic quantum dot surface model

The synthetic strategies and reagents used to prepare QDs vary widely between materials and have advanced greatly over time.[1,17,18] While the effects of these synthetic differences are discussed in section 1.3, one universal factor that must first be addressed is ligation at the quantum dot surface. Individual nanoparticles are stabilized during and after growth by ligand molecules.[17,19,20] Commonly used moieties include carboxylates, phosphonates, thiolates, amines, and phosphines. These ligands serve to stabilize under-coordinated surface atoms, prevent aggregation during nanoparticle growth, and promote colloidal solubility. Many metal-ligand interactions have been well-studied for small molecules in the organometallic literature.[21–23] While this serves as a guide to understanding ligand-metal interactions at the nanoparticle surface, understanding these interactions quantitatively has been a long standing challenge in quantum dot research. This challenge arises both from the complexity of large, non-uniform surfaces and analytical limitations. There are dozens of commonly used organic and inorganic ligands and hundreds of quantum dot precursors that are frequently mixed in many syntheses, resulting in a broad and complex scope of reported ligation motifs.[24,25] Moreover there are a limited number of methods and techniques with which to analyze a nanoparticle's surface. Commonly used techniques include transmission electron microscopy (TEM), nuclear magnetic resonance spectroscopy (NMR), X-ray photoelectron spectroscopy (XPS), X-ray diffraction (XRD), Infra-red (IR), UV-Vis, and fluorescence spectroscopies. However, many of these techniques not only lack the ability to resolve surface and bulk differences but convolute greatly from even small amounts of nanoparticle or ligand polydispersity, with single crystal X-ray diffraction being limited to a select few examples.[26–28] As a result, in spite of the tremendous importance of surface analysis, exact surface quantification remains a challenging issue in quantum dot research.

A qualitative conceptualization of a typical quantum dot can be described as a nearly stoichiometric particle with a metal-rich surface that is passivated by surfactant ligands (Figure 1.2).[29]

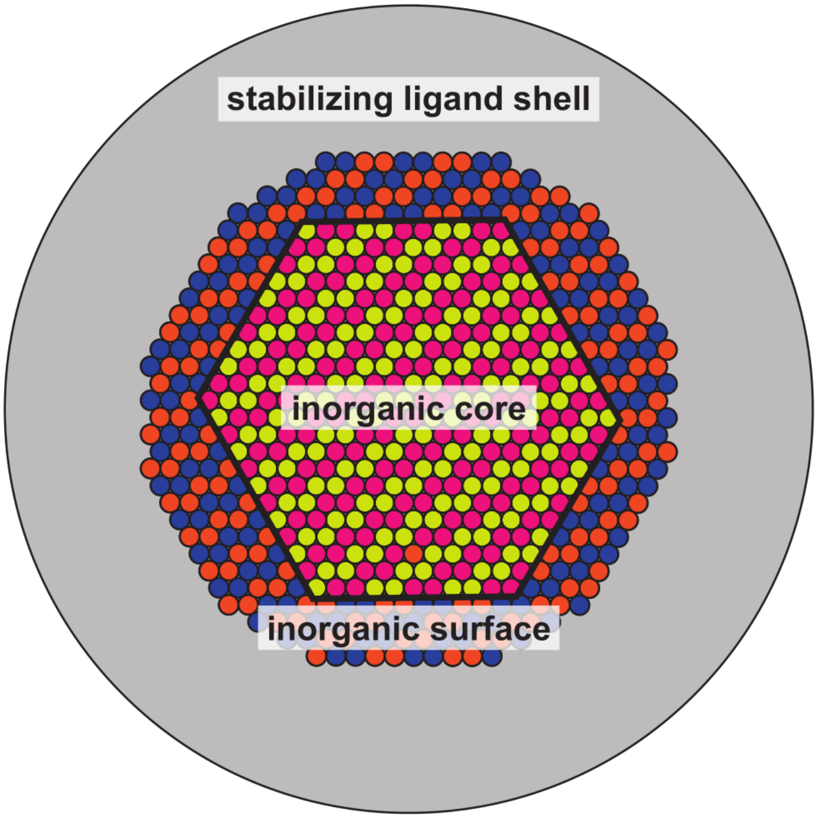

Figure 1.2. Cartoon depiction of an approximately stoichiometric nanoparticle with a crystalline core, distinct surface environment, and layer of ligand surfactant.

Surface ligands are commonly referred to as belonging to one of three classes depending on their general binding behavior: X-type charged ligands which bind covalently such as carboxylate, L-type ligands which bind datively such as amine, or Z-type neutral organometallic molecules which bind datively such as $Cd(COOR)_2$. Salts and other outer-sphere charge balancing species are not generally considered ligands and are usually the result of stripping away or under-passivation of the initial ligand layer.[30] In addition to these binding motifs there are many highly relevant factors to nanoparticle ligation that may be quantified including the number of ligands per particle, facet-specific binding, binding mode and denticity, binding strength, electronic influence, stability, and equilibria with other species.[19,31–35] Moreover, these behaviors can vary greatly for the same ligand between material systems. For example, whereas amines stabilize Cd chalcogenides, they retard the growth of and decompose InP[20,25]. The organometallic analogy can only go so far to investigate many of these points. In small molecules charge balancing and valence filling greatly dictate ligand behavior. By contrast it has been shown that nanoparticle surfaces are highly dynamic and can stabilize missing ligands and charges via surface defects.[15] These surface defects generally are localized and result in intra-band gap electronic states which can radically alter a particle's electronic behavior.[36–38] Finding and addressing such states is an imperative goal when designing quantum dots for emissive applications, for example. Likewise, distinct surface states play a key role in the catalytic activity of quantum dots.

One of the greatest tools in investigating at the level of detail demanded by this complexity is single crystal X-ray diffraction spectroscopy. Ensemble polydispersity of nanocrystals normally makes this impossible. In select cases however, small molecularly precise nanocrystals called clusters in conjunction with crystallographic measurements represent the "gold standard" in investigating nanomaterial surfaces with the same certainty seen in organometallic chemistry for decades. Unfortunately crystal structures remain elusive for most observable cluster species, especially for semiconducting material systems. Working with clusters as model systems however remains a tractable approach with atomistic precision for studying nanocrystal surfaces and behaviors across many methods.[39] Ultimately care must be taken in an almost case-by-case basis to carefully consider and understand how the surface of a quantum dot is both synthesized and treated for any given application or system.

1.3 Synthetic and post-synthetic control over quantum dot surfaces

Early investigations into synthesizing quantum dots often involved formation in a solid matrix or polymer stabilized solution.[40,41] These systems provided great insight into the novel optical and electronic properties of semiconducting nanoparticles but could only be studied using solid state methods, and by modern standards the quality (i.e., crystallinity, polydispersity, etc.) of the materials was quite low. By introducing coordinating solvents such as oleylamine and trioctlyphosphine, colloidal synthetic routes became widespread, and it was quickly recognized that coordinating surfactants had a great impact on controlling particle size and monodispersity, as well influencing optoelectronic behavior and defect densities.[17,38] At this time, reproducibility was a problem facing the field. Buhro and others demonstrated that impurities in commonly used solvents such as trioctyl phosphine oxide (TOPO) were preferentially binding surfactants and had tremendous impact on nanocrystal morphology during synthesis.[42] This revelation set the foundation for the field of ligand mediated nanocrystal shape control and affirmed the importance of careful solvent and surfactant consideration. Combined with procedural refinements, colloidal synthesis became and has remained the primary method for producing many types of high quality nanoparticles.

Modern QD syntheses typically aim to optimize ensemble monodispersity and minimize defects that negatively affect optoelectronic properties. This is often performed by designing conditions to achieve a LaMer type growth profile using a combination of high concentration and temperature.[43,44] Long-chain fatty acids, amines, and phosphines with high solubility in organic solvents and high temperature stability such as oleic acid, oleylamine, and trioctlyphosphine are commonly used in many different modern material syntheses. These reagents are commercially available and can be readily used in the preparation of organometallic precursors in many cases. As a result, highly monodisperse colloidal syntheses currently exist for a wide variety of materials. Optimizing for monodispersity however does not ensure the high-quality optoelectronic properties of a quantum dot. In many cases effectively monodisperse solutions can have so many surface defects as to have < 1% fluorescence quantum yield as is commonly observed during InP QD synthesis for example.[45] It has been shown that at high temperatures carboxylates can decompose to form water, as a result it is very likely that the high temperatures required to form monodisperse QDs unavoidably introduce oxidative defects.[46] Straightforward optimizations to synthetic variables such as temperature and reagent purity cannot entirely eliminate such a problem, instead post-synthetic strategies are a promising and more generally applicable alternative.

Post-synthetic modifications typically involve chemical treatment or shelling of the nanocrystal or both.[1,24,36,38,47–49] Type I shells have been shown to pacify surface defects including vacancies and under-passivation. Using large band gap type I shells in this manner is a common approach for making high quantum yield nanoparticles of various compositions. The method has several drawbacks however. Finding a compatible shelling material and scalable conditions that will shell without damaging the starting nanocrystals is non-trivial. Moreover, shelling cannot repair all types of defects and has been shown to cause strain related defects and undesired optoelectronic effects as well.[50,51]

A more broadly defined approach to nanoparticle surface modification involves the post synthetic treatment with small molecules. Owen et al. for example have shown that treatment with Z-type metal-ligand molecules can effectively, post-synthetically passivate certain surface defects relating to undercoordination.[44] Similar treatments have shown improvements in quantum yields for other materials with treatment by HF being a common example.[52] Ion treatment by the addition of additional metal ions such as Zn and Cd have also been explored as methods of targeting and repairing specific surface traps.[38] The addition of supplemental L-type ligand to improve solubility is also reported in several cases.[18,53] The addition or substitution of ligands has become an increasingly studied method in nanoparticle chemistry. By using this method one may optimize monodispersity with highly soluble fatty acid based ligands and separately optimize for the desired system afterwards. For example it has been shown by Talapin, Bawendi, and Kagan that conductivity of nanoparticle films can be increased dramatically by substituting shorter ligands, ligands which could fundamentally not be used in bottom up syntheses.[54] In extreme cases ligands have been removed altogether using alkylating reagents, either as an intermediate step in ligand exchange or to produce optimal electronic coupling of the quantum dot to a substrate.[55] Such systems are strictly only obtainable through post-synthetic means. Given the tremendous impact of the nanoparticle surface on its properties, controlling that surface is a primary objective of any materials chemist. Considering the difficulties and complexities of quantum dot synthesis it is imperative to be aware of and control the surface from the earliest stages of synthesis, and in order to produce the most useful materials possible continue to study and modify the surface post synthetically as well.

1.4 The surface chemistry of mesocrystals

Nanocrystal surfaces also play a tremendous role in thinking about nanoscale synthesis across length scales. In this regard, a rapidly growing field within nanomaterial chemistry over the last decade has been the study of mesocrystals, their assembly, novel properties, and surface chemistry. Mesocrystals can be described as assemblies of nanocrystals often with pseudo crystalline packing or order up to macroscopic length scales.[56] These structures were first appreciated in the field of biomineralization,[57] but the principle has since been drastically expanded upon using a wide variety of metal, semiconducting, and mineral nanoparticles. Understanding the surface chemistry at work in driving the formation of mesocrystals and related hybrid structures has been a critical foundation of the research effort. Surface effects are key in driving the ordered assembly process which has been shown to occur in different systems between crystalline facets,[57] ligand shell interactions,[58,59] and through direct covalent bridging.[60] In all these cases understanding and control of surface chemistry is critical towards directing the assembly process. It has been shown that the produced assemblies often exhibit novel or increased electronic properties through near-field interactions between particles.[61,62] One exceptionally useful application for which mesocrystals may be ideal is heterogeneous photocatalysis. Mesocrystal structures combine naturally active nanocrystals to form stable, extremely high surface area structures with excellent catalytic activity and turnover.[63] The effectiveness of photocatalytic activity in this type of system has recently gained interest as the electronic communication afforded by the electronically interconnected particles can result in effective (de)localization of photogenerated charges.[64,65] One of our longstanding research efforts is to take full advantage of this motif to enable highly efficient, and robust photocatalysts for green chemical transformations.

1.5 References

(1) Reiss, P.; Protière, M.; Li, L. Core/Shell Semiconductor Nanocrystals. *Small* **2009**, *5* (2), 154–168. https://doi.org/10.1002/smll.200800841.

(2) Rao, J. P.; Geckeler, K. E. Polymer Nanoparticles: Preparation Techniques and Size-Control Parameters. *Prog. Polym. Sci.* **2011**, *36* (7), 887–913. https://doi.org/10.1016/j.progpolymsci.2011.01.001.

(3) Mody, V. V.; Siwale, R.; Singh, A.; Mody, H. R. Introduction to Metallic Nanoparticles. *J. Pharm. Bioallied Sci.* **2010**, *2* (4), 282–289. https://doi.org/10.4103/0975-7406.72127.

(4) Fernández-Garcia, M.; Rodriguez, J. A. Metal Oxide Nanoparticles. 60.

(5) Hines, D. A.; Kamat, P. V. Recent Advances in Quantum Dot Surface Chemistry. *ACS Appl. Mater. Interfaces* **2014**, *6* (5), 3041–3057. https://doi.org/10.1021/am405196u.

(6) Giansante, C. Surface Chemistry Control of Colloidal Quantum Dot Band Gap. *J. Phys. Chem. C* **2018**, *122* (31), 18110–18116. https://doi.org/10.1021/acs.jpcc.8b05124.

(7) Kroupa, D. M.; Vörös, M.; Brawand, N. P.; McNichols, B. W.; Miller, E. M.; Gu, J.; Nozik, A. J.; Sellinger, A.; Galli, G.; Beard, M. C. Tuning Colloidal Quantum Dot Band Edge Positions through Solution-Phase Surface Chemistry Modification. *Nat. Commun.* **2017**, *8*, 15257. https://doi.org/10.1038/ncomms15257.

(8) Giansante, C.; Infante, I. Surface Traps in Colloidal Quantum Dots: A Combined Experimental and Theoretical Perspective. *J. Phys. Chem. Lett.* **2017**, *8* (20), 5209–5215. https://doi.org/10.1021/acs.jpclett.7b02193.

(9) Rossetti, R.; Brus, L. Electron-Hole Recombination Emission as a Probe of Surface Chemistry in Aqueous Cadmium Sulfide Colloids. *J. Phys. Chem.* **1982**, *86* (23), 4470–4472. https://doi.org/10.1021/j100220a003.

(10) Tian, F.; Bonnier, F.; Casey, A.; Shanahan, A. E.; Byrne, H. J. Surface Enhanced Raman Scattering with Gold Nanoparticles: Effect of Particle Shape. *Anal. Methods* **2014**, *6* (22), 9116–9123. https://doi.org/10.1039/C4AY02112F.

(11) Yanhong, L.; Dejun, W.; Qidong, Z.; Min, Y.; Qinglin, Z. A Study of Quantum Confinement Properties of Photogenerated Charges in ZnO Nanoparticles by Surface Photovoltage Spectroscopy. *J. Phys. Chem. B* **2004**, *108* (10), 3202–3206. https://doi.org/10.1021/jp037201k.

(12) Baltz, R. v.; Klingshirn, C. F. Semiconductor Bloch Equations. In *Semiconductor Optics*; Klingshirn, C. F., Ed.; Graduate Texts in Physics; Springer: Berlin, Heidelberg, 2012; pp 813–833. https://doi.org/10.1007/978-3-642-28362-8_27.

(13) *The Electronic Structure and Chemistry of Solids*; Oxford University Press: Oxford, New York, 1987.

(14) Fuhr, A. S.; Yun, H. J.; Makarov, N. S.; Li, H.; McDaniel, H.; Klimov, V. I. Light Emission Mechanisms in CuInS2 Quantum Dots Evaluated by Spectral Electrochemistry. *ACS Photonics* **2017**, *4* (10), 2425–2435. https://doi.org/10.1021/acsphotonics.7b00560.

(15) Brawand, N. P.; Goldey, M. B.; Vörös, M.; Galli, G. Defect States and Charge Transport in Quantum Dot Solids. *Chem. Mater.* **2017**, *29* (3), 1255–1262. https://doi.org/10.1021/acs.chemmater.6b04631.

(16) Chen, L. X.; Liu, T.; Thurnauer, M. C.; Csencsits, R.; Rajh, T. Fe2O3 Nanoparticle Structures Investigated by X-Ray Absorption Near-Edge Structure, Surface Modifications, and Model Calculations. *J. Phys. Chem. B* **2002**, *106* (34), 8539–8546. https://doi.org/10.1021/jp025544x.

(17) Murray, C. B.; Norris, D. J.; Bawendi, M. G. Synthesis and Characterization of Nearly Monodisperse CdE (E = Sulfur, Selenium, Tellurium) Semiconductor Nanocrystallites. *J. Am. Chem. Soc.* **1993**, *115* (19), 8706–8715. https://doi.org/10.1021/ja00072a025.

(18) Bang, E.; Choi, Y.; Cho, J.; Suh, Y.-H.; Ban, H. W.; Son, J. S.; Park, J. Large-Scale Synthesis of Highly Luminescent InP@ZnS Quantum Dots Using Elemental Phosphorus Precursor. *Chem. Mater.* **2017**, *29* (10), 4236–4243. https://doi.org/10.1021/acs.chemmater.7b00254.

(19) Peng, Z. A.; Peng, X. Mechanisms of the Shape Evolution of CdSe Nanocrystals. *J. Am. Chem. Soc.* **2001**, *123* (7), 1389–1395. https://doi.org/10.1021/ja0027766.

(20) Gary, D. C.; Petrone, A.; Li, X.; Cossairt, B. M. Investigating the Role of Amine in InP Nanocrystal Synthesis: Destabilizing Cluster Intermediates by Z-Type Ligand Displacement. *Chem. Commun.* **2017**, *53* (1), 161–164. https://doi.org/10.1039/C6CC07952K.

(21) Crabtree, R. H. *The Organometallic Chemistry of the Transition Metals*, 5 edition.; Wiley: Hoboken, N.J, 2009.

(22) Fey, N.; Orpen, A. G.; Harvey, J. N. Building Ligand Knowledge Bases for Organometallic Chemistry: Computational Description of Phosphorus(III)-Donor Ligands and the Metal–Phosphorus Bond. *Coord. Chem. Rev.* **2009**, *253* (5), 704–722. https://doi.org/10.1016/j.ccr.2008.04.017.

(23) Omae, Iwao. Organometallic Intramolecular-Coordination Compounds Containing a Nitrogen Donor Ligand. *Chem. Rev.* **1979**, *79* (4), 287–321. https://doi.org/10.1021/cr60320a001.

(24) Zhou, J.; Liu, Y.; Tang, J.; Tang, W. Surface Ligands Engineering of Semiconductor Quantum Dots for Chemosensory and Biological Applications. *Mater. Today* **2017**, *20* (7), 360–376. https://doi.org/10.1016/j.mattod.2017.02.006.

(25) Green, M. The Nature of Quantum Dot Capping Ligands. *J. Mater. Chem.* **2010**, *20* (28), 5797–5809. https://doi.org/10.1039/C0JM00007H.

(26) Cossairt, B. M.; Owen, J. S. CdSe Clusters: At the Interface of Small Molecules and Quantum Dots. *Chem. Mater.* **2011**, *23* (12), 3114–3119. https://doi.org/10.1021/cm2008686.

(27) Gary, D. C.; Terban, M. W.; Billinge, S. J. L.; Cossairt, B. M. Two-Step Nucleation and Growth of InP Quantum Dots via Magic-Sized Cluster Intermediates. *Chem. Mater.* **2015**, *27* (4), 1432–1441. https://doi.org/10.1021/acs.chemmater.5b00286.

(28) Bürgi, T. Properties of the Gold–Sulphur Interface: From Self-Assembled Monolayers to Clusters. *Nanoscale* **2015**, *7* (38), 15553–15567. https://doi.org/10.1039/C5NR03497C.

(29) Owen, J. The Coordination Chemistry of Nanocrystal Surfaces. *Science* **2015**, *347* (6222), 615–616. https://doi.org/10.1126/science.1259924.

(30) Chang, C. M.; Orchard, K. L.; Martindale, B. C. M.; Reisner, E. Ligand Removal from CdS Quantum Dots for Enhanced Photocatalytic H2 Generation in PH Neutral Water. *J. Mater. Chem. A* **2016**, *4* (8), 2856–2862. https://doi.org/10.1039/C5TA04136H.

(31) Anderson, N. C.; Hendricks, M. P.; Choi, J. J.; Owen, J. S. Ligand Exchange and the Stoichiometry of Metal Chalcogenide Nanocrystals: Spectroscopic Observation of Facile Metal-Carboxylate Displacement and Binding. *J. Am. Chem. Soc.* **2013**, *135* (49), 18536–18548. https://doi.org/10.1021/ja4086758.

(32) Knauf, R. R.; Lennox, J. C.; Dempsey, J. L. Quantifying Ligand Exchange Reactions at CdSe Nanocrystal Surfaces. *Chem. Mater.* **2016**, *28* (13), 4762–4770. https://doi.org/10.1021/acs.chemmater.6b01827.

(33) Xie, L.; Shen, Y.; Franke, D.; Sebastián, V.; Bawendi, M. G.; Jensen, K. F. Characterization of Indium Phosphide Quantum Dot Growth Intermediates Using MALDI-TOF Mass Spectrometry. *J. Am. Chem. Soc.* **2016**, *138* (41), 13469–13472. https://doi.org/10.1021/jacs.6b06468.

(34) Zhao, Q.; Kulik, H. J. Electronic Structure Origins of Surface-Dependent Growth in III–V Quantum Dots. *Chem. Mater.* **2018**. https://doi.org/10.1021/acs.chemmater.8b03125.

(35) Barngrover, B. M.; Aikens, C. M. The Golden Pathway to Thiolate-Stabilized Nanoparticles: Following the Formation of Gold(I) Thiolate from Gold(III) Chloride. *J. Am. Chem. Soc.* **2012**, *134* (30), 12590–12595. https://doi.org/10.1021/ja303050s.

(36) Asai, K.; Yamaki, T.; Seki, S.; Ishigure, K.; Shibata, H. Surface Treatment Effect of Ion Irradiation on Size-Quantized Semiconductor Particles Incorporated into LB Films. *Thin Solid Films* **1996**, *284–285*, 541–544. https://doi.org/10.1016/S0040-6090(95)08387-1.

(37) Weiss, E. A. Organic Molecules as Tools To Control the Growth, Surface Structure, and Redox Activity of Colloidal Quantum Dots. *Acc. Chem. Res.* **2013**, *46* (11), 2607–2615. https://doi.org/10.1021/ar400078u.

(38) Stein, J. L.; Holden, W. M.; Venkatesh, A.; Mundy, M. E.; Rossini, A. J.; Seidler, G. T.; Cossairt, B. M. Probing Surface Defects of InP Quantum Dots Using Phosphorus Kα and Kβ X-Ray Emission Spectroscopy. *Chem. Mater.* **2018**. https://doi.org/10.1021/acs.chemmater.8b02590.

(39) Cossairt, B. M.; Owen, J. S. CdSe Clusters: At the Interface of Small Molecules and Quantum Dots. *Chem. Mater.* **2011**, *23* (12), 3114–3119. https://doi.org/10.1021/cm2008686.

(40) Wang, Y.; Herron, N. Nanometer-Sized Semiconductor Clusters: Materials Synthesis, Quantum Size Effects, and Photophysical Properties. *J. Phys. Chem.* **1991**, *95* (2), 525–532.

(41) Kagan, C. R.; Murray, C. B.; Nirmal, M.; Bawendi, M. G. Electronic Energy Transfer in CdSe Quantum Dot Solids. *Phys. Rev. Lett.* **1996**, *76* (9), 4.

(42) Wang, F.; Tang, R.; Kao, J. L.-F.; Dingman, S. D.; Buhro, W. E. Spectroscopic Identification of Tri- *n* -Octylphosphine Oxide (TOPO) Impurities and Elucidation of Their Roles in Cadmium Selenide Quantum-Wire Growth. *J. Am. Chem. Soc.* **2009**, *131* (13), 4983–4994. https://doi.org/10.1021/ja900191n.

(43) Enright, M. J.; Ritchhart, A.; Cossairt, B. M. Nucleation and Growth of Colloidal Semiconductor Nanoparticles. In *Encyclopedia of Inorganic and Bioinorganic Chemistry*; American Cancer Society, 2020; pp 1–11. https://doi.org/10.1002/9781119951438.eibc2723.

(44) Owen, J. S.; Park, J.; Trudeau, P.-E.; Alivisatos, A. P. Reaction Chemistry and Ligand Exchange at Cadmium−Selenide Nanocrystal Surfaces. *J. Am. Chem. Soc.* **2008**, *130* (37), 12279–12281. https://doi.org/10.1021/ja804414f.

(45) Stein, J. L.; Steimle, M. I.; Terban, M. W.; Petrone, A.; Billinge, S. J. L.; Li, X.; Cossairt, B. M. Cation Exchange Induced Transformation of InP Magic-Sized Clusters. *Chem. Mater.* **2017**, *29* (18), 7984–7992. https://doi.org/10.1021/acs.chemmater.7b03075.

(46) Xie, L.; Harris, D. K.; Bawendi, M. G.; Jensen, K. F. Effect of Trace Water on the Growth of Indium Phosphide Quantum Dots. *Chem. Mater.* **2015**, *27* (14), 5058–5063. https://doi.org/10.1021/acs.chemmater.5b01626.

(47) Shea-Rohwer, L. E.; Martin, J. E.; Cai, X.; Kelley, D. F. Red-Emitting Quantum Dots for Solid-State Lighting. *ECS J. Solid State Sci. Technol.* **2013**, *2* (2), R3112–R3118. https://doi.org/10.1149/2.015302jss.

(48) Groeneveld, E.; Witteman, L.; Lefferts, M.; Ke, X.; Bals, S.; Van Tendeloo, G.; de Mello Donega, C. Tailoring ZnSe–CdSe Colloidal Quantum Dots via Cation Exchange: From Core/Shell to Alloy Nanocrystals. *ACS Nano* **2013**, *7* (9), 7913–7930. https://doi.org/10.1021/nn402931y.

(49) Roberge, A.; Stein, J. L.; Shen, Y.; Cossairt, B. M.; Greytak, A. B. Purification and In Situ Ligand Exchange of Metal-Carboxylate-Treated Fluorescent InP Quantum Dots via Gel Permeation Chromatography. *J. Phys. Chem. Lett.* **2017**, *8* (17), 4055–4060. https://doi.org/10.1021/acs.jpclett.7b01772.

(50) Rafipoor, M.; Dupont, D.; Tornatzky, H.; Tessier, M. D.; Maultzsch, J.; Hens, Z.; Lange, H. Strain Engineering in InP/(Zn,Cd)Se Core/Shell Quantum Dots. *Chem. Mater.* **2018**, *30* (13), 4393–4400. https://doi.org/10.1021/acs.chemmater.8b01789.

(51) Stier, O.; Grundmann, M.; Bimberg, D. Electronic and Optical Properties of Strained Quantum Dots. *Phys. Rev. B* **1999**, *59* (8), 5688.

(52) Samadpour, M.; Boix, P. P.; Giménez, S.; Iraji Zad, A.; Taghavinia, N.; Mora-Seró, I.; Bisquert, J. Fluorine Treatment of TiO2 for Enhancing Quantum Dot Sensitized Solar Cell Performance. *J. Phys. Chem. C* **2011**, *115* (29), 14400–14407. https://doi.org/10.1021/jp202819y.

(53) Cooper, J. K.; Franco, A. M.; Gul, S.; Corrado, C.; Zhang, J. Z. Characterization of Primary Amine Capped CdSe, ZnSe, and ZnS Quantum Dots by FT-IR: Determination of Surface Bonding Interaction and Identification of Selective Desorption. *Langmuir* **2011**, *27* (13), 8486–8493. https://doi.org/10.1021/la201273x.

(54) Kagan, C. R.; Murray, C. B.; Bawendi, M. G. Long-Range Resonance Transfer of Electronic Excitations in Close-Packed CdSe Quantum-Dot Solids. *Phys. Rev. B* **1996**, *54* (12), 8633–8643. https://doi.org/10.1103/PhysRevB.54.8633.

(55) Xuan, T.; Yang, X.; Lou, S.; Huang, J.; Liu, Y.; Yu, J.; Li, H.; Wong, K.-L.; Wang, C.; Wang, J. Highly Stable CsPbBr3 Quantum Dots Coated with Alkyl Phosphate for White Light-Emitting Diodes. *Nanoscale* **2017**, *9* (40), 15286–15290. https://doi.org/10.1039/C7NR04179A.

(56) Rosseeva), E. V. S. (née; Cölfen, H. Mesocrystals: Structural and Morphogenetic Aspects. *Chem. Soc. Rev.* **2016**, *45* (21), 5821–5833. https://doi.org/10.1039/C6CS00208K.

(57) Cölfen, H.; Antonietti, M. Mesocrystals: Inorganic Superstructures Made by Highly Parallel Crystallization and Controlled Alignment. *Angew. Chem. Int. Ed Engl.* **2005**, *44* (35), 5576–5591. https://doi.org/10.1002/anie.200500496.

(58) Tachikawa, T.; Majima, T. Metal Oxide Mesocrystals with Tailored Structures and Properties for Energy Conversion and Storage Applications. *NPG Asia Mater.* **2014**, *6* (5), e100. https://doi.org/10.1038/am.2014.21.

(59) Zhou, L.; Smyth-Boyle, D.; O'Brien, P. A Facile Synthesis of Uniform NH_4 $TiOF_3$ Mesocrystals and Their Conversion to TiO_2 Mesocrystals. *J. Am. Chem. Soc.* **2008**, *130* (4), 1309–1320. https://doi.org/10.1021/ja076187c.

(60) Huang, M.; Schilde, U.; Kumke, M.; Antonietti, M.; Cölfen, H. Polymer-Induced Self-Assembly of Small Organic Molecules into Ultralong Microbelts with Electronic Conductivity. *J. Am. Chem. Soc.* **2010**, *132* (11), 3700–3707. https://doi.org/10.1021/ja906667x.

(61) Yang, J.-C.; He, Q.; Zhu, Y.-M.; Lin, J.-C.; Liu, H.-J.; Hsieh, Y.-H.; Wu, P.-C.; Chen, Y.-L.; Lee, S.-F.; Chin, Y.-Y.; Lin, H.-J.; Chen, C.-T.; Zhan, Q.; Arenholz, E.; Chu, Y.-H. Magnetic Mesocrystal-Assisted Magnetoresistance in Manganite. *Nano Lett.* **2014**, *14* (11), 6073–6079. https://doi.org/10.1021/nl5019172.

(62) Kodaimati, M. S.; Lian, S.; Schatz, G. C.; Weiss, E. A. Energy Transfer-Enhanced Photocatalytic Reduction of Protons within Quantum Dot Light-Harvesting–Catalyst Assemblies. *Proc. Natl. Acad. Sci.* **2018**, *115* (33), 8290–8295. https://doi.org/10.1073/pnas.1805625115.

(63) Zhang, D.; Li, G.; Wang, F.; Yu, J. C. Green Synthesis of a Self-Assembled Rutile Mesocrystalline Photocatalyst. *CrystEngComm* **2010**, *12* (6), 1759–1763. https://doi.org/10.1039/B922477G.

(64) Hu, B.; Wu, L.-H.; Zhao, Z.; Zhang, M.; Chen, S.-F.; Liu, S.-J.; Shi, H.-Y.; Ding, Z.-J.; Yu, S.-H. Hierarchical Silver Indium Tungsten Oxide Mesocrystals with Morphology-, Pressure-, and Temperature-Dependent Luminescence Properties. *Nano Res.* **2010**, *3* (6), 395–403. https://doi.org/10.1007/s12274-010-1044-y.

(65) Kodaimati, M. S.; McClelland, K. P.; He, C.; Lian, S.; Jiang, Y.; Zhang, Z.; Weiss, E. A. Viewpoint: Challenges in Colloidal Photocatalysis and Some Strategies for Addressing Them. *Inorg. Chem.* **2018**, *57* (7), 3659–3670. https://doi.org/10.1021/acs.inorgchem.7b03182.

Chapter 2. Quantifying Ligand Exchange on InP Using an Atomically-Precise Cluster Platform

Adapted with permission from the Journal of Inorganic Chemistry. Copyright 2019 American Chemical Society.

2.1 Introduction

Our understanding of the chemistry of colloidal semiconductor nanoparticles has advanced to enable progress in applying these materials in a wide range of applications including catalysis,[1,2] photovoltaics,[3,4] displays,[5] and imaging.[6,7] Recent efforts have focused on developing non-toxic materials, such as InP, for large-scale, highly distributed applications.[8,9] Research into II-IV and III-V nanomaterials has been tailored to the applications at hand by manipulating the quantum confinement effect as a function of size,[10,11] shape,[12,13] and composition.[14] Underpinning this research, and fundamental to colloidal nanoparticle function and synthesis, is the nature of the nanoparticle surface. The surface and ligand layer represents a highly complex component of the nanoparticle composition that has influence on the structural, electronic, and reactivity properties of the nanomaterial.[15,16] Accurately quantifying the binding properties of ligands is critical for designing size-tunable and anisotropic nanoparticle syntheses,[17,18] as well as for post synthetic modifications such as shelling, passivation, or cation exchange.[19–21] A detailed, analytical understanding of the surface structure and ligand coordination properties of a colloidal system must underscore any rational design of nanoscale properties in those systems.

Post synthetic ligand modification specifically has enabled a host of targeted applications. Exchanging ligands of differing hydrophobicity has long been known to facilitate changes in nanoparticle solubility, a critical parameter to control for applications in biosensing.[22] In a similar manner, modifying mixed ligand shells to tune hydrophobicity has been used to coordinate the formation of nanoparticle superstructures.[23] For catalysis applications, ligand exchange has been used improve C-C coupling rate[24] as well as H_2 production.[25] Furthermore, quantum dots are frequently treated with additives such as HF and Zn^{2+} in order to improve photoluminescent quantum yields by removing defects such as dangling bonds at the surface.[26–28] Finally, post-synthetic ligand modification is required for tuning interparticle charge and exciton transfer in thin films of colloidal semiconductor nanocrystals.[29] The nature of these applications implicitly requires post synthetic surface modification because the resulting surface chemistries would be significantly altered or the chemistry would preclude particle nucleation and growth.[30] Therefore, a robust understanding of ligand behavior not only directly benefits nanoparticle synthetic design but can also enable it to be separately optimized and better compartmentalized from applications.

Previous work in the literature has elegantly defined the binding affinities and characteristics of common ligands in the cases of CdSe,[31–34] PbS,[35,36] and perovskites.[37,38] Using NMR spectroscopy, it has been shown that equilibrium models for the binding of ligands on these surfaces can be accurately and easily measured. These previous analyses, however, suffer from fundamental limitations of measuring ensemble properties of inherently polydisperse samples. Because these systems are not perfectly uniform and vary with respect to particle size, and moreover, the number and type of binding sites, simplifying assumptions must be made or the model must take these factors into consideration. This greatly complicates the modeling, reducing the translatability and interpretation across particle sizes, compositions, and morphologies. Critically, many of these systems lack experimental quantification of ligand binding modes in the first place, relying on theory or analogy to distantly-related molecular structures. Here we illustrate the veracity of using the precisely known $In_{37}P_{20}X_{51}$ (X = carboxylate) cluster as a model for the

InP nanocrystal surface. This cluster can be synthesized and purified on a large scale and its surface chemistry is precisely known from single crystal X-ray diffraction analysis.[39] Notably, despite the rising prominence of InP nanocrystals for emissive applications, no such investigation into the ligation and surface binding properties of InP has been performed to date.

In order to answer outstanding questions surrounding InP nanoparticle surface chemistry, we adopt an analytical ^{1}H NMR spectroscopic approach used to great success in the CdSe and PbS literature.[31,35,40] Traditional aliphatic ligands are not diagnostically useful in the ^{1}H NMR spectrum of nanoparticles due to excessive overlapping and polydispersity of their alkyl resonances in the upfield region. By using alkene-labeled ligands it is possible to quantitatively measure both free and bound ligands on the nanoparticle surface in the relatively clean 4.0-6.0 ppm region. It is convenient for our purposes then to use secondary alkene oleate ligands on the native particle surface in conjunction with terminal alkenes as the exchanging ligands to enable complete deconvolution and analytical assessment of the ligand exchange equilibria. The sources of ^{1}H resonance shifts in nanoparticle solutions has recently been examined in detail including the source of peak shifts and broadening of ligated species.[41] By using a high field instrument, ligated molecules can be reliably shifted and deconvoluted from their free counterparts. Herein we will use these ^{1}H NMR properties to model ligand exchange equilibria as reversible chemical processes (Scheme 2.1) using

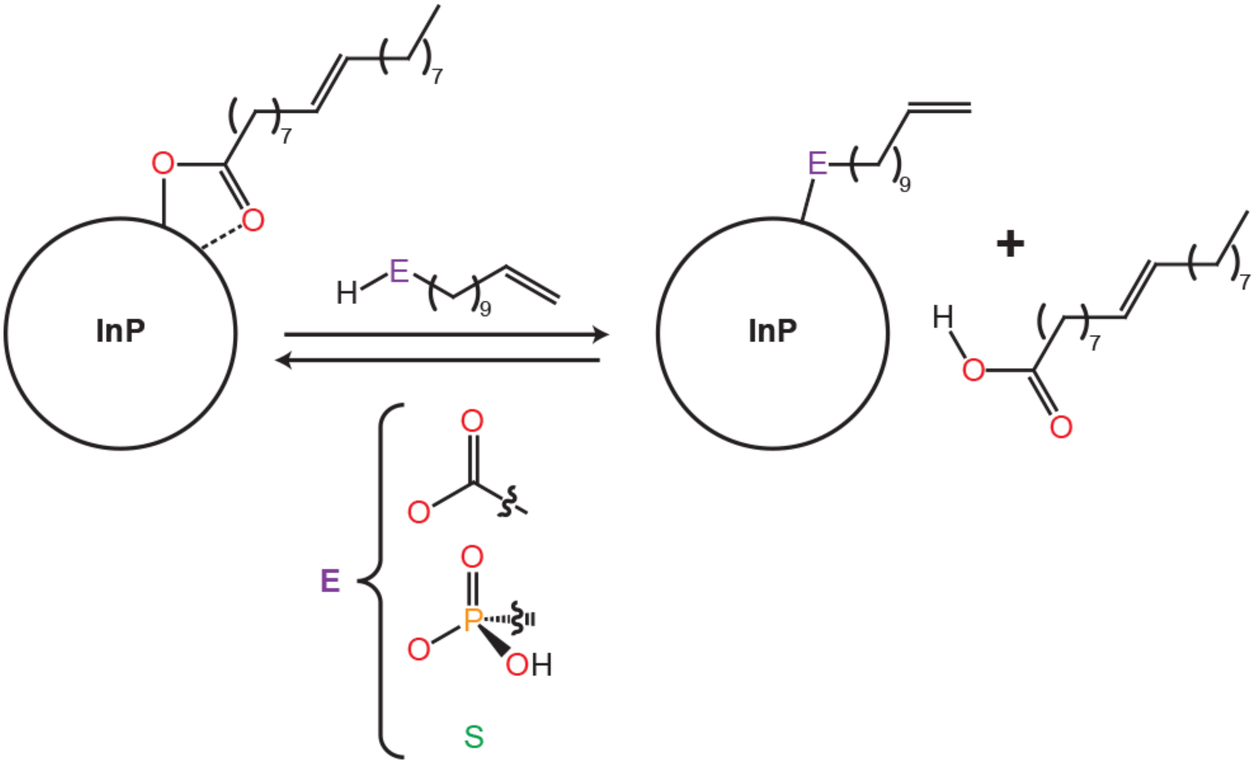

Scheme 2.1. Reaction Scheme Showing the Equilibrium Exchange of Oleate Ligands on InP Particles for Incoming Terminal Alkene-Labeled Ligands, Including Carboxylic Acid, Phosphonic Acid, and Thiol

quantitative NMR integration and fitting in conjunction with mesitylene as an internal standard, and highly purified 1.3 nm $In_{37}P_{20}X_{51}$ cluster as a precise starting point. Per-particle measurements are normally highly limited by not just polydispersity but also the inherent difficulty in determining nanoparticle concentrations. Using an atomically defined starting point eliminates data convolution arising from ensemble measurements and allows for highly precise correlations of per-particle properties such as ligand count and density.

2.2 Results and Discussion

2.2.1 Carboxylate-Carboxylic Acid Exchange

Carboxylates have historically been the ligand of choice for the synthesis of InP nanoparticles both for general laboratory use as well as for their application in commercialized display technologies.[5] The exchange between X-type carboxylate ligands (Figure 2.1) such as oleate (Ol) and dodec-11-enoic acid (DDA) on nanoparticle surfaces has often been modeled as a metathesis type equilibrium as described by equation 2.1.

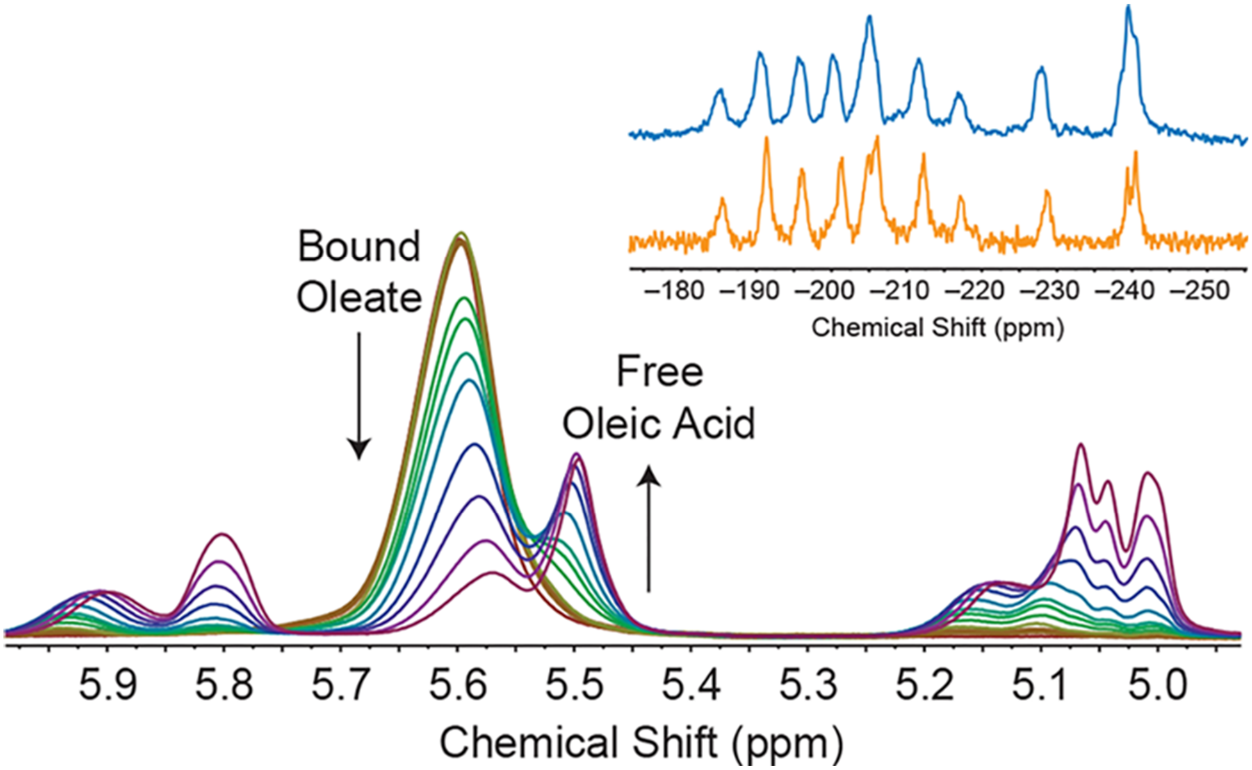

Figure 2.1. ^{1}H NMR spectra of the alkene region for titration of DDA into a solution of the Ol-capped $In_{37}P_{20}$ cluster, from 0 equiv (red) to 139 equiv (violet). Resonances at 5.8–5.9 and 5.0–5.2 ppm correspond to DDA, while those at 5.4–5.7 ppm correspond to Ol. Inset: ^{31}PNMR spectra of the starting cluster (blue) and the cluster + 139 equiv of DDA (orange).

$$[Ol]_B + [DDA]_F k_1 \rightleftarrows k_{-1} [Ol]_F + [DDA]_B \tag{2.1}$$

$$K_{eq} = \frac{[Ol]_F [DDA]_B}{[Ol]_B [DDA]_F} \tag{2.2}$$

This model is indifferent to binding modes of the ligand and site differentiation on the nanocrystal. The crystal structure of the $In_{37}P_{20}X_{51}$ cluster with carboxylate ligands is known and exhibits exclusively bidentate and bridging-bidentate X-type binding across a relatively uniform surface. Attempting to model the exchange as an X-type metathesis and determine K_{eq} via equation 2.2 shows a non-linear trend that can be interpreted as two distinct equilibrium regimes (Figure 2.2A). The difference in these regimes is much greater than would be expected from the difference in chemical potential between facets of InP[42], moreover a non-stoichiometric exchange ratio is seen in the early regime with sub-stoichiometric ligand displacement. Therefore, we consider an alternative, neutral L-type binding mode in addition to the X-type exchange to account for this increase in coverage.

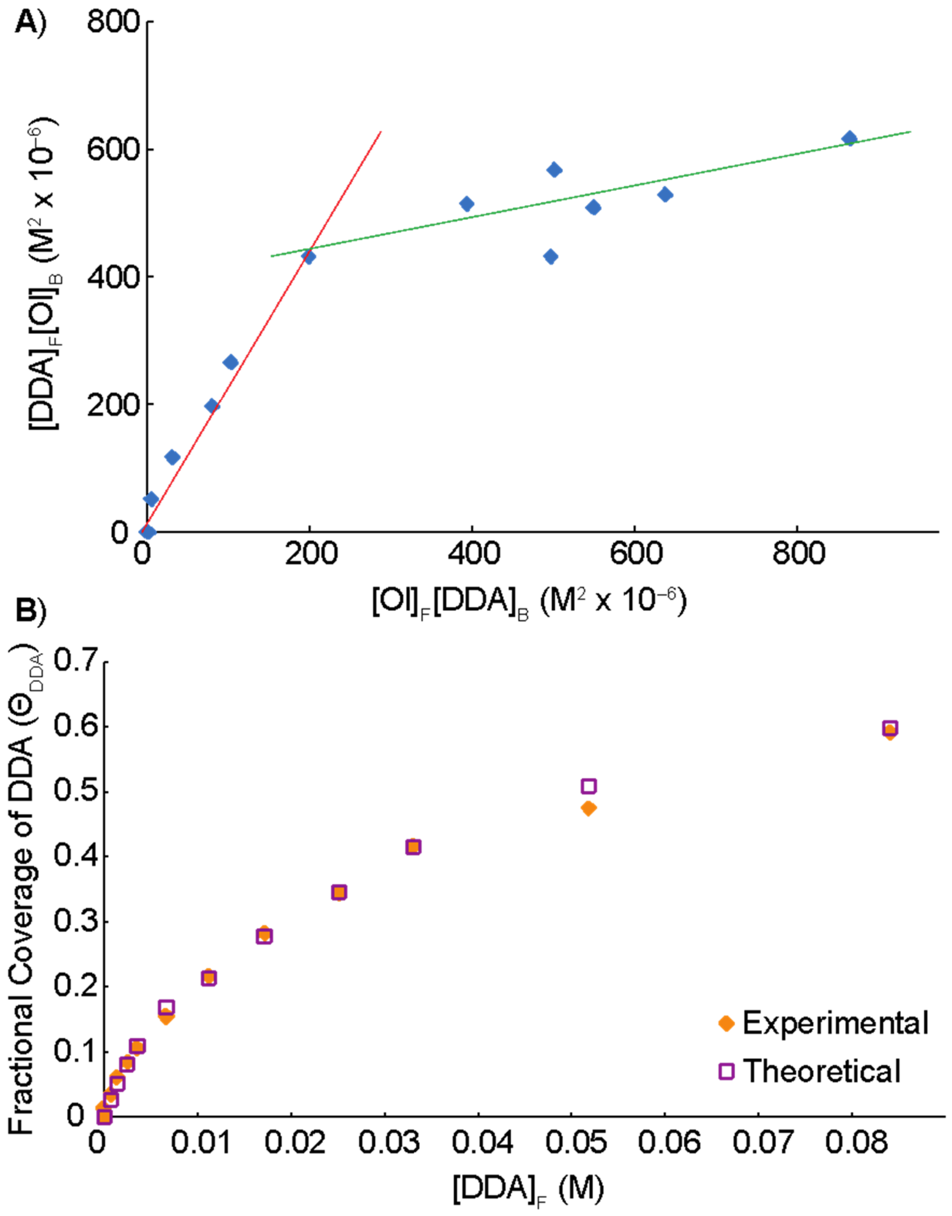

Figure 2.2. A) A metathesis-style plot of K_{eq} via equation 2.2 for the titration of DDA vs oleate capped cluster. Instead of a single slope corresponding to K_{eq}, empirically two regimes of differing equilibrium constant are seen. B) The same data replotted using an isotherm fit via equation 2.4. This fit gives the following values: $KX_{eq} = 0.80$, $KL_{DDA} = 2.3$, $KL_{Ol} = 1.9$, $nX = 51$, $nL = 8$.

To model this type of binding, we adopt a modified multi-site Langmuir isotherm model (equation 3) that enables us to account for multiple species as well as multiple binding modes. Additional details and derivation are available in experimental section 2.4.4. Equation 2.3 represents the binding of titrated acid (DDA) using a multisite-competitive Langmuir isotherm, which models the bound fraction of ligand, θ_{DDA}, as a function of free ligand concentrations and equilibrium constants. This model allows for the fitting of the fraction of sites belonging to each mode per nanoparticle, the L-type equilibria of each acid, and the relative X-type binding affinity of each carboxylate, such that $KX_{DDA}/KX_{Ol} = KX_{eq}$. We note that based on the range of calculated ligand desorption energies for different sites on the $In_{37}P_{20}$ cluster and the 1:1 nature of this exchange process, we would not expect to be able to distinguish individual X-type sites.[45] Considering that a ligand bound in the X- vs L-type mode will have a nearly indistinguishable terminal alkene resonance we can further rearrange equation 2.3 into directly measurable concentrations for quantitative ^1H NMR analysis via equation 2.4. Using this model, we see a much-improved fit and experimentally determine the equilibrium constants (Figure 2.2B). Our experimental value for KX_{eq} of 0.80 is remarkably similar to KX_{eq} reported by Dempsey et al. for a virtually identical pair of ligands on CdSe QDs,[31] suggesting that some relative binding properties of ligands may translate very well between nanoparticle systems. This may be especially true for Cd^{2+} and In^{3+}-based systems given the similarities in cation size and Lewis acidity. While the basicity of carboxylic acids is well characterized[43,44] the L-type equilibria of carboxylic acids on nanoparticle surfaces has to our knowledge never been quantified. Here we find equilibrium constants for the L-type binding of typical aliphatic carboxylates to be on the order of KL = 2.0 and that L-type binding accounts for approximately 15% of the total ligation when saturated. Given that L-type binding would proceed as a Lewis base interaction with a surface In atom, this ratio would likely decrease with the decreasing concentration of surface In that has been theorized and observed on larger particles.[45] Because these In sites are sterically saturated at the onset by bidentate binding, we would predict the L-type binding to be monodentate and concomitant with neighboring monodentate shifts in order to maintain coordination number and charge balance (Scheme 2.2).

$$\theta_{DDA} = \chi_x \frac{KX_{DDA}[DDA]_F}{1+KX_{DDA}[DDA]_F+KX_{Ol}[Ol]_F} + \chi_l \frac{KL_{DDA}[DDA]_F}{1+KL_{DDA}[DDA]_F+KL_{Ol}[Ol]_F} \tag{2.3}$$

$$[DDA]_B = [MSC]\left(nX \frac{KX_{DDA}[DDA]_F}{1+KX_{DDA}[DDA]_F+KX_{Ol}[Ol]_F} + nL \frac{KL_{DDA}[DDA]_F}{1+KL_{DDA}[DDA]_F+KL_{Ol}[Ol]_F}\right) \tag{2.4}$$

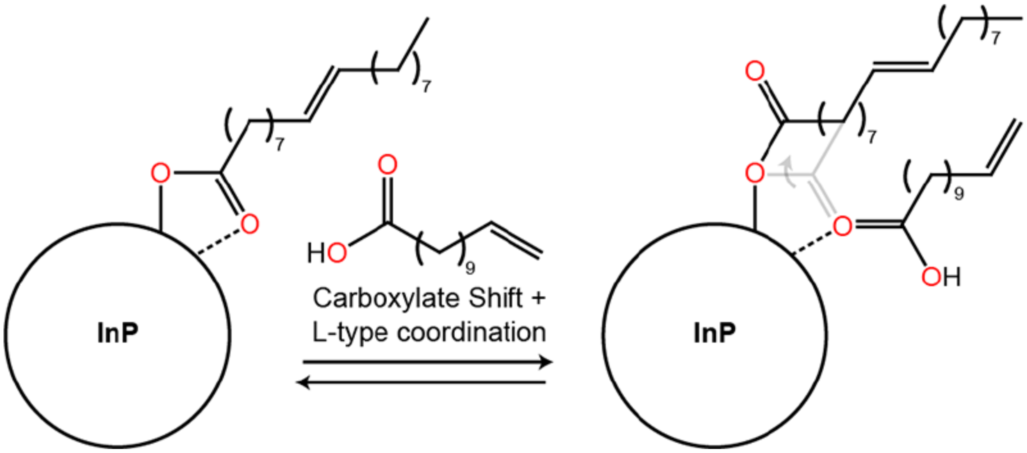

Scheme 2.2. Schematic representation of L-Type carboxylic acid coordination with a concomitant shift in a bidentate carboxylate to a monodentate binding mode

The difference between the L- and X-type binding modes was further investigated using variable temperature (VT) ^{1}H NMR spectroscopy (Figure 2.3). Because the theoretical number of L-type sites is small due to steric crowding on the cluster surface and the binding is favorable, the low free acid concentration regime can be considered L-exchange dominated, whereas the high free acid regime would theoretically be X-exchange dominated and L-type saturated. Constructing a Van't Hoff plot by examining K_{eq} as a function of temperature in the high concentration regime at 44 equivalents of acid (115 mM acid) reveals a nearly iso-Gibbs energy reaction. This is a reasonable result given that the number of particles in the system remains unchanged and that the acids are extremely similar with an equilibrium constant quite close to one. By contrast, examining the low, L-type dominated regime at 7 eq (18 mM) reveals weakly positive enthalpy and entropy terms of $\Delta H° = 8$ kJ/mol and $\Delta S° = 26$ J/mol K respectively, in line with similar measurements in the literature. These values equate to a ΔG of 412 J/mol at room temperature and suggest that L-type binding is slightly unfavorable whereas the isotherm fitting indicated it was slightly favorable. This may be an artifact of X-type exchange or other rearrangements convoluting the measurement, however it would also be unsurprising that carboxylic acids bind less favorably than traditional Lewis basic L-type ligands such as amines or phosphines. Positive entropy terms for ligand exchange reactions have been observed previously and assigned by others in the literature as disorder in the ligand shell, i.e. the entropy of mixing.[31,40] Entropy purely from mixing would, however, be proportional to the molar fractions of ligands being mixed and thus we would expect an order of magnitude lower entropy for the low equivalent exchange regime, treated as ideal species just 1.2 J/mol K.[46] We have previously shown crystallographically that carboxylates have four distinct X-type binding modes on InP that are predominantly bridging and bidentate. We hypothesize that L-type carboxylate binding would be associated with local rearrangement with neighboring ligands shifting from bidentate to monodentate in order to alleviate steric hindrance and reveal additional coordination sites. This denticity rearrangement has been seen crystallographically during the adsorption of water to the InP cluster.[47] Such a rearrangement could result in a net increase in entropy related to the increase in available microstates of a monodentate species vs a more rigidly bound bidentate ligand. Such conformational entropies have been calculated to be on the order of 10 J/mol K per degree denticity in other systems.[48]

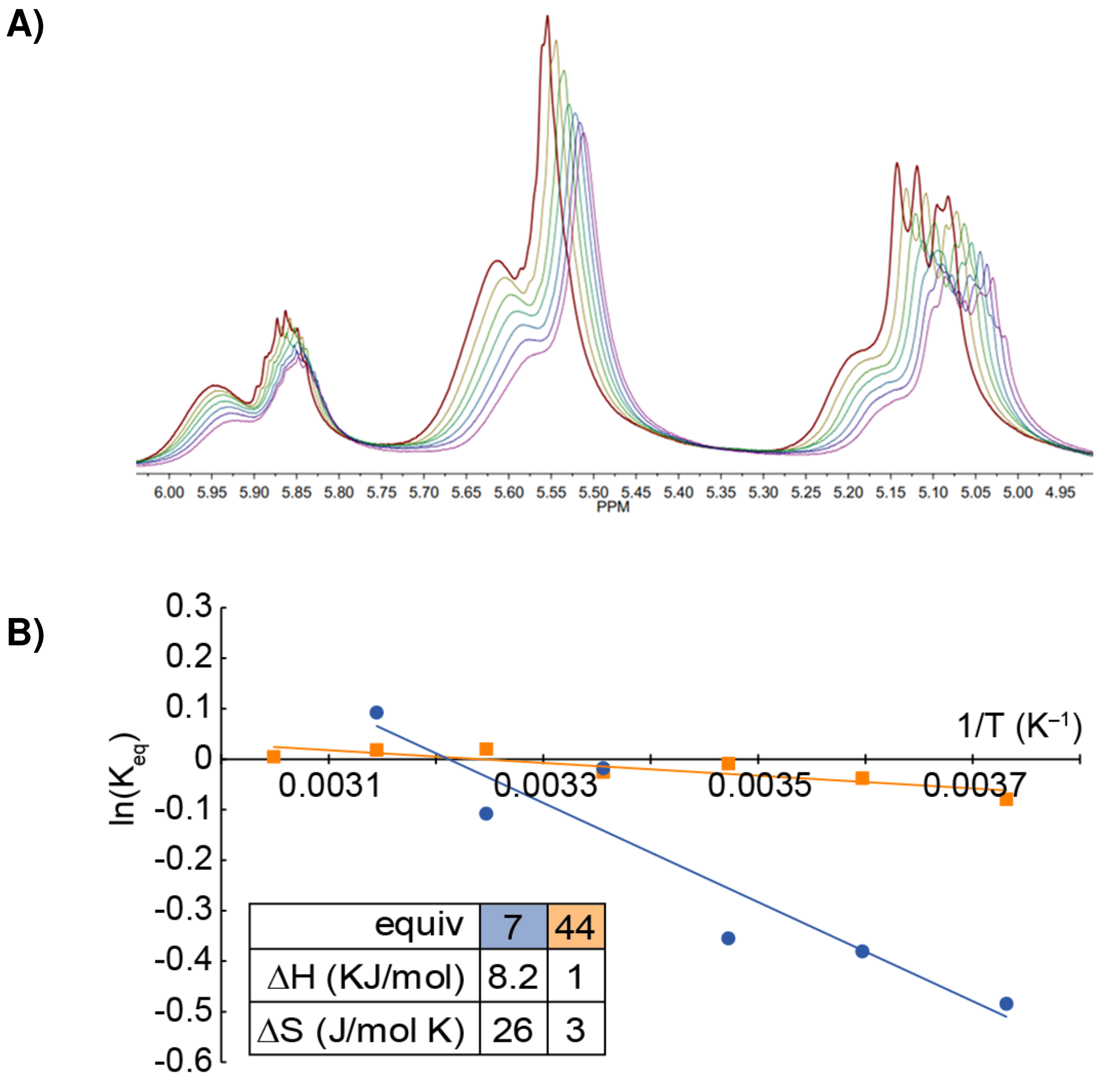

equiv	7	44
ΔH (KJ/mol)	8.2	1
ΔS (J/mol K)	26	3

Figure 2.3. A) ^{1}H NMR of cluster with 44 equiv additional DDA acquired from 268 K (red trace) to 328 K (magenta trace) in 10 K increments, toluene-d8, 700 MHz. B) Corresponding Van't Hoff plots for the temperature-dependant equilibria of DDA vs oleate at a low concentration (blue) vs high concentration (orange) regimes of added DDA.

The excitonic feature of the cluster as measured by UV-Vis spectroscopy was tracked as a function of added titrant and undergoes a slight 20 meV redshift followed by a 60 meV blueshift over the course of the titration at room temperature (Figure 2.4). This change is inconsistent with what has been seen in the Z-type etching of In-carboxylate from the cluster by amine.[47] Rather this strongly indicates influence of the ligand shell over the excitonic wavefunction which is magnified due to the cluster's small size. Given the electronic similarity of oleic acid and DDA this shift is more attributable to changes in the surface environment as opposed to ligand identity, with changes in binding modes and increased total coverage being the operative differences. As such, this feature is not only tunable but highly reversible and a useful metric for conveniently tracking cluster purification. The ^{31}P NMR spectrum does not show an appreciable change upon the addition of excess carboxylic acid (Figure 2.1, inset). Given that exchange is fast relative to the NMR timescale and that the net density of oxygen bonds at the surface does not change, this is not surprising, and supports the stability of the cluster towards excess carboxylic acid.

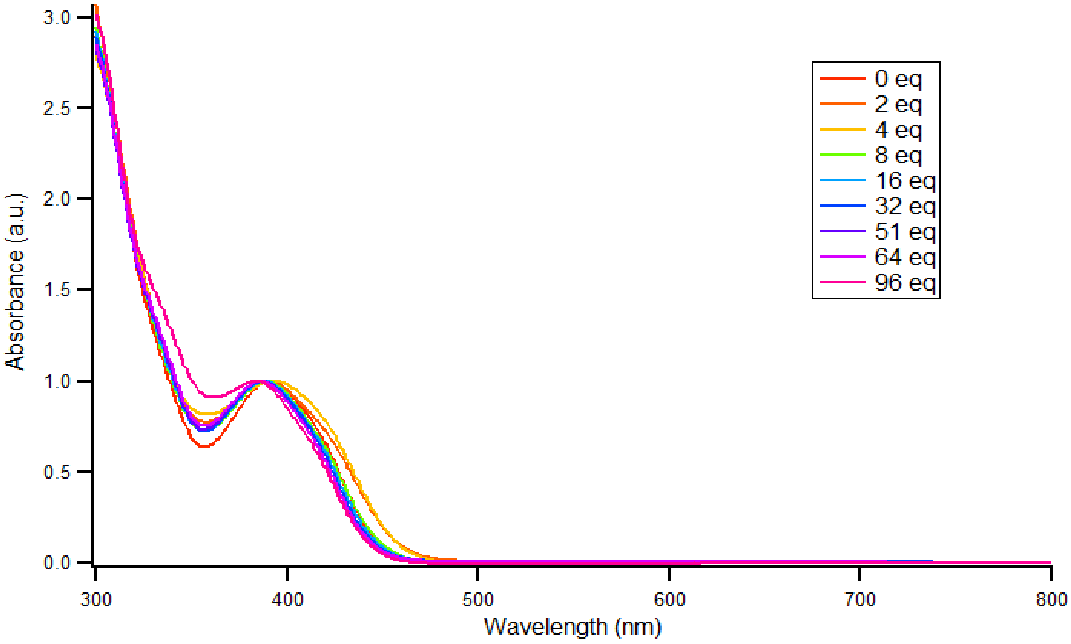

Figure 2.4. Shifting absorbance spectra of $In_{37}P_{20}$ cluster with additional carboxylic acid.

2.2.2 Carboxylate-Phosphonic Acid Exchange

Phosphonic acids are widely used in the semiconducting nanocrystal literature as robust X-type capping ligands. As ligands they are characterized by their variable, bidentate binding modes and strong, often irreversible, binding affinity.[49,50] These properties have been the driving arguments for synthetic observations such as anisotropic growth[51,52] and shelling inhibition, as well as influencing physical properties of nanoparticles through enhanced thermal, photochemical, and oxidative stability.[53–55] In the case of InP, phosphonate capping ligands have been little explored, and no bottom-up syntheses of InP using phosphonate ligands have been reported beyond a phosphonate-capped cluster species.[56] This is likely due to the extreme stability these ligands impart upon low molecular weight, oligomeric, and cluster intermediates.

Dianionic binding of phosphonates and displacement of carboxylate is widely reported in the quantum dot literature. This is readily predictable as phosphonic acids are roughly three orders of magnitude more acidic than analogous carboxylic acids and subsequent bidentate binding is heavily favored by the chelate effect.[57] Assuming the dianionic nature of the phosphonate ligand, the theoretical point of complete stoichiometric exchange on the starting oleate-ligated $In_{37}P_{20}X_{51}$ cluster by adding 10-ene-undecyl-phosphonic acid (UDPA) is 25.5 equivalents. Titrations towards this stoichiometric point at room temperature are associated with a steady blueshift of the excitonic feature in the UV-vis spectrum across a range of 10 meV, beyond which a decrease in intensity and loss of the lowest energy features and solution color are observed, suggesting cluster decomposition (Figure 2.5).

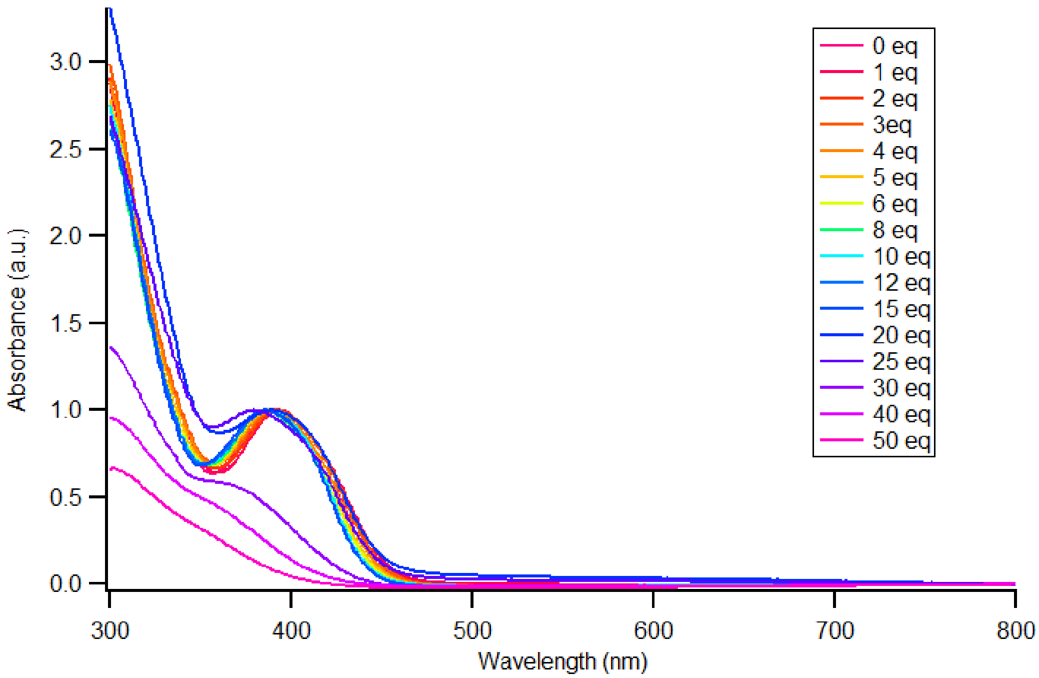

Figure 2.5. Shifting absorbance spectra of In37P20 cluster with additional phosphonic acid.

The initial hypsochromic shift is reasonably attributable to what has been proposed in the literature as ligand effects on excitonic wavefunctions as a function of head group electronegativity.[58–60] The HOMO and LUMO of the cluster are calculated to reside close to the surface and can be influenced by binding agents as we have shown previously.[39] Additionally, the exchange of carboxylate for phosphonate ligands dictates a significant degree of surface rearrangement, corroborated by an increase in cluster symmetry as seen by ^{31}P NMR spectroscopy (Figure 2.6 C). During this room temperature ligand exchange, however, structural rearrangement is not equivalent to the alternate zincblende cluster structure observed from bottom-up synthesis at elevated temperatures. Rather, the $In_{37}P_{20}$ cluster core is evidently kinetically stable across the complete range of the ligand exchange. By ^{1}H NMR spectroscopy we measure the stoichiometry of this exchange between carboxylate and phosphonate to be 2.10 ± 0.06 carboxylates per phosphonic acid (Figure 2.6), in strong agreement with the initial hypothesis of bidentate, irreversible binding as the phosphonate dianion.

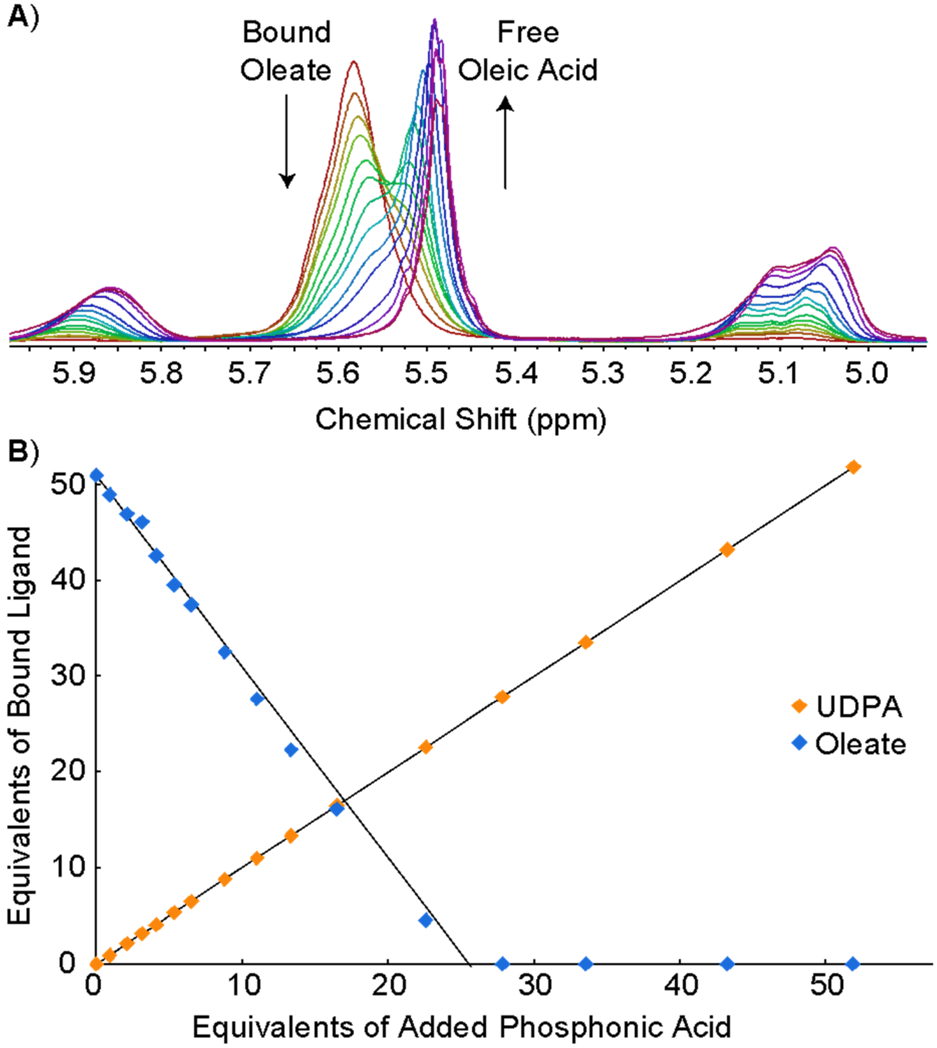

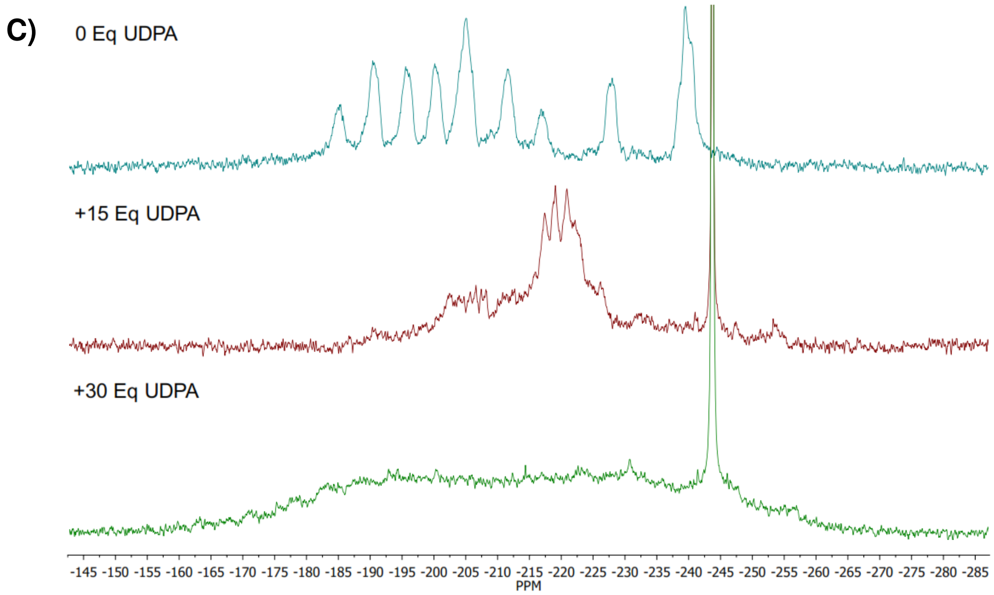

Figure 2.6. A) ^{1}H NMR spectra of the alkene region for the titration UDPA into a solution of oleate capped $In_{37}P_{20}$ cluster, from 0 equivalents (red) to 51 equivalents (violet). Resonances at 5.8-5.9 and 5.0-5.2 correspond to UDPA while 5.4-5.7 correspond to oleate. B) Quantification of the displacement of carboxylate (blue) by phosphonate (orange). The solid black lines correspond to theoretical 1:1 (UDPA:UDPA, increasing) and 2:1 (DDA:UDPA, decreasing) stoichiometries respectively. C)) ^{31}P NMR spectra of the phosphide region for the titration UDPA into a solution of oleate capped $In_{37}P_{20}$ cluster, from 0 equivalents to 30 equivalents.

Beyond the stoichiometric point of complete exchange there is no appearance of a free phosphonic acid resonances in either the ^{1}H or ^{31}P{^{1}H} NMR spectra in these experiments. Coupled with the bleach of the UV-Vis spectroscopic features, this suggests cluster decomposition in the presence of excess acid. The stoichiometric point of etching to form In_2PA_3 and PH_3 would be 55.5 equivalents of added phosphonic acid, however we do not observe a distinct crossover at this point. Etched PH_3 accounts for less than 3% of the phosphorous measured via ^{31}P NMR spectroscopy and the continued absence of free phosphonic acid suggests that InP decomposition by phosphonic acid does not proceed through primarily PH_3 displacement. Instead, the broadening of the bound phosphonate resonances and eventual solidification of the sample implies the formation of complex $InP(PO_3)(PO_3H)$ species. Despite this transformation being as completely forward driven as ligand exchange, it is only observed after ligand exchange is complete, prior to which at least 20 unique bound phosphonate resonances are observable in the ^{31}P NMR spectrum. Oligomeric phosphonate products such as this are likely what inhibits bottom-up growth of phosphonate-capped InP nanoparticles.

2.2.3 Carboxylate-Thiol Exchange

While not a general-use ligand choice for InP synthesis as compared to carboxylates, thiols hold great interest in InP syntheses insofar as they relate to shelling strategies to access InP@ZnS and related heterostructures.[61,62] A preliminary treatment of the exchange equilibrium between 10-undecene-1-thiol (UDTh) and oleate ligands on the cluster using equation 2.2 results in a similar two regime progression as seen in the carboxylate exchange case. Quantifying the exchange by total ligands bound per particle, however, reveals a trend inconsistent with a mixed L- and X-type binding model. The low concentration exchange regime exhibits a highly stoichiometric 50 ± 1 total X-type ligands bound. Following a rigid one-to-one exchange rate ratio strongly implies thiol does not L-type bind to InP. Additionally, the exchange causes a significant loss of ^{31}P environment symmetry as observed by NMR spectroscopy that likely signifies surface reconstruction (Figure 2.7). This surface rearrangement appears to preclude carboxylate L-type binding, as is also observed in the case of phosphonate coordination. Modeled as pure X-type exchange, this regime follows a thiolate for carboxylate exchange with $KX_{eq} = 3.9$ through 36 equivalents of added thiol, meaning a favorable exchange for thiol is seen through approximately 50% starting ligand substitution. This favorable binding is consistent with thiolate being a much softer Lewis base than carboxylate and In^{3+} being a relatively soft Lewis acid. By contrast, in the high concentration regime a roughly linear increase in the total number of bound ligands is observed at a ratio of approximately one per six equivalents of thiol added, or equivalently per increase in 0.6 mM thiol.

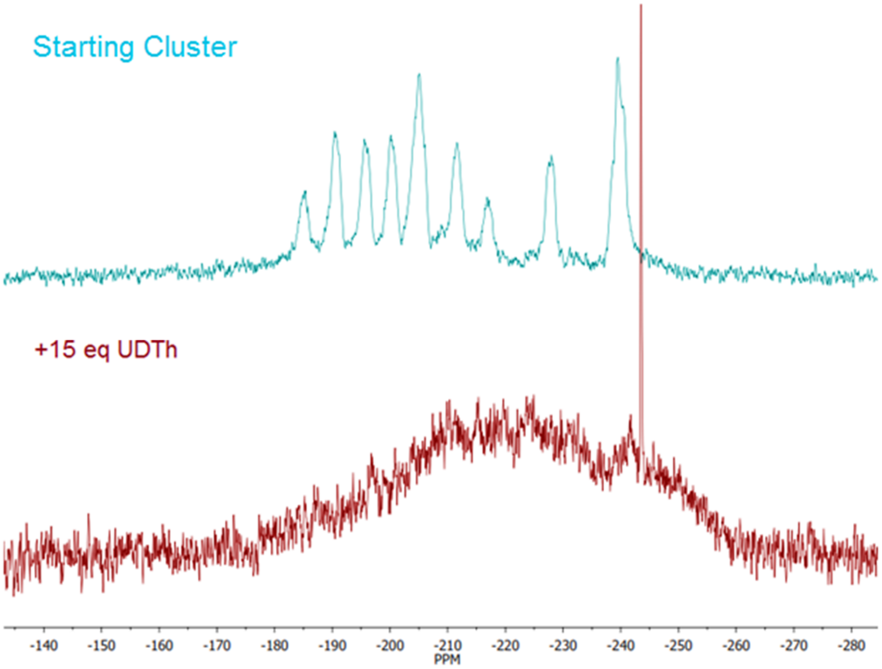

Figure 2.7. ^{31}P NMR spectra of the phosphide region for the titration UDTh into a solution of oleate capped $In_{37}P_{20}$ cluster at 0 and 15 equivalents.

Because there is no observed L-type binding, super-stoichiometric binding in this second regime can only be explained by particle etching, exposing either more metal atoms on the surface or in solution. Similar observations have been made in the Z-type etching of CdSe nanoparticles by concentrated primary alcohols.[63] Using ^{1}H DOSY NMR spectroscopy we measure the signal vs gradient decay rates for the bound species to be clearly non-monoexponential (Figure 2.8 A). Polyexponential decay curves mean that a sum of diffusing products is being measured, supporting the hypothesis of particle etching. Using biexponential fitting, three distinct species are found and can be independently correlated with the chemical shifts of bound or free regions (Figure 2.8 B). These species were found to have diffusion constants $D = 1 \times 10^{-5}$, 5×10^{-7}, and 4×10^{-6} cm^2/s which we assign as free acid/thiol, cluster, and etched product respectively. Accounting for solvent viscosity differences these values are consistent with literature.[41,64]

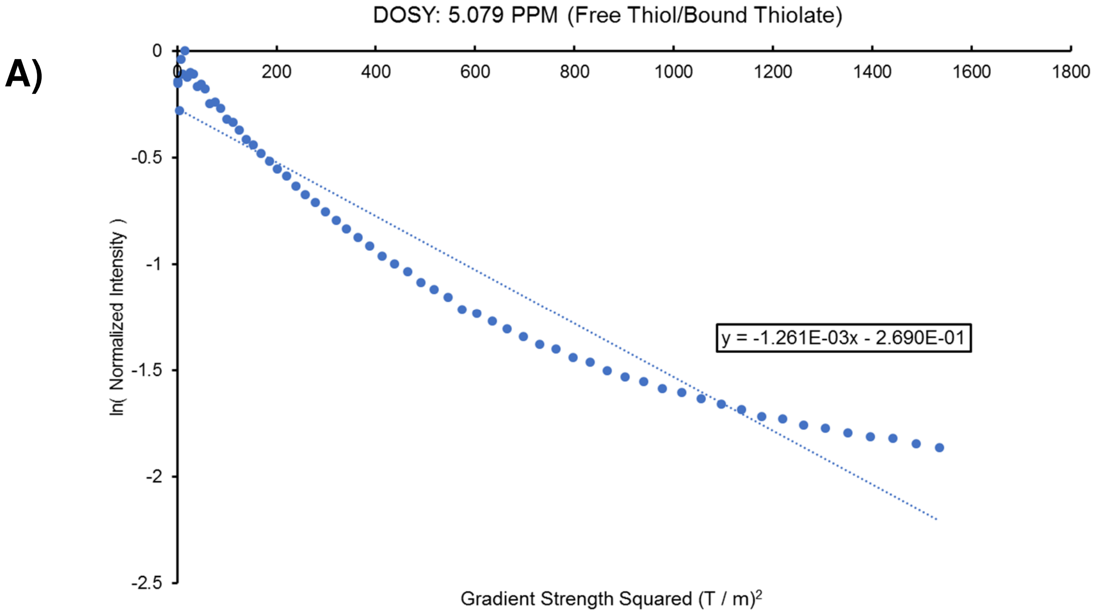

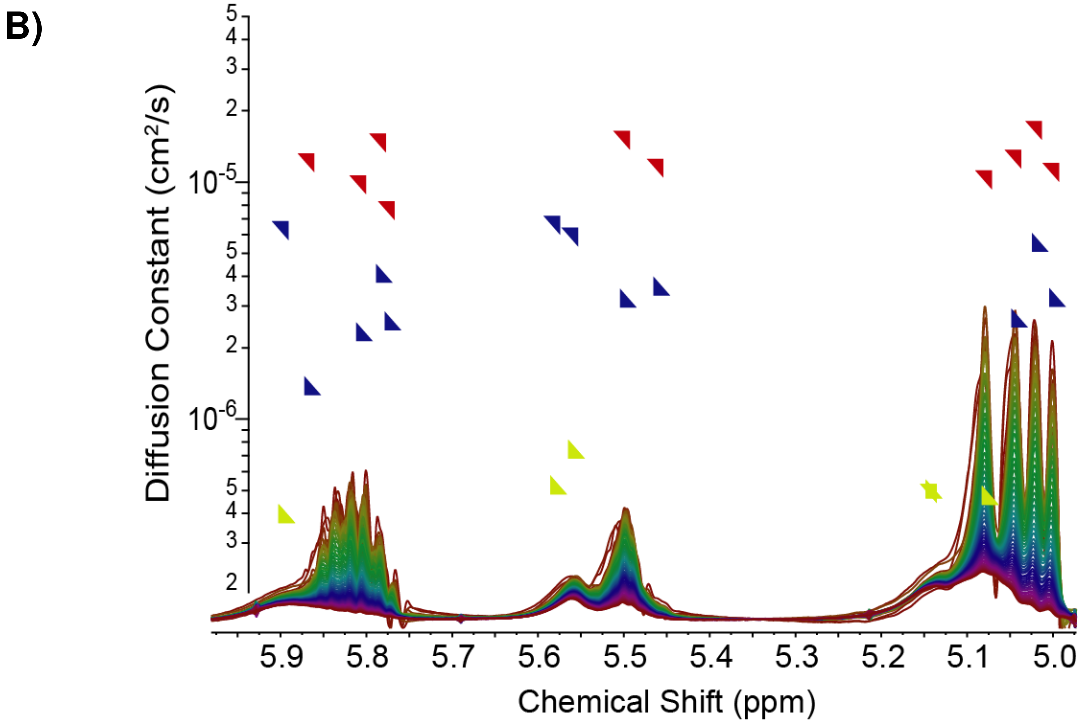

Figure 2.8. A) Example of a non-monoexponential diffusion signal decay measured in the alkene region. B) ^{1}H DOSY NMR spectra from low gradient (red) to high gradient (violet), overlaid with corresponding pairs of diffusion constants acquired from bi-exponential fits. Mean diffusion constants in benzene and assignments are as follows (cm^{2}/s): 1×10^{-5} (red) free acid, 5×10^{-7} (blue) etched species, 4×10^{-6} (green) cluster.

The etched product appears to contain both thiolate and carboxylate. Using the Stokes-Einstein equation this material has a hydrodynamic radius of 1.0 nm, approximately three times that of the free acid. Specifically assigning this species is very challenging as many small oligomers can be drawn with mixed numbers of carboxylates and thiolates, especially considering the many bridging modes of carboxylate. Whether this species also contains. No such decomposition was observed by ^{1}H and ^{31}P{^{1}H} NMR spectroscopy after exposing a sample of cluster to 16 equivalents of thiol for 12 hours, while decomposition was effectively immediate when exposed to an excess of 35 equivalents of thiol. This observation is unlike the Z-type displacement by amines on both InP[65] and CdSe,[63] where initial displacement is very rapid and subsequently slows, likely speaking to a different displacement mechanism. Whereas the carboxylate and phosphonate exchange systems were found to be relatively analogous to what has been found for CdSe nanoparticles, the case for thiol differs quite dramatically. There is no evidence to suggest that thiol shows L-type behavior or that thiolate irreversibly binds on InP. Additionally, no evidence for the formation of disulfides was found in the ^{1}H NMR data, which would have a diagnostic triplet at 2.5 ppm. The etched product of high concentration thiol exposure to the InP cluster most closely resembles Z-type exchange observed in the presence of alcohols in metal chalcogenide systems.

2.2.4 Carboxylate-Carboxylate Exchange on QDs

The $In_{37}P_{20}X_{51}$ cluster has proven to be a robust analog for InP quantum dots in many regards. It possesses a similar stoichiometry, has an In-Rich surface comparable to that which has been established for InP quantum dots, and is passivated with the same commonly used ligands. Given the cluster's greater curvature and more confined electronic structure, the similarity of ligand affinity between cluster and nanoparticle is not immediately obvious.[66] To establish the veracity of using the InP cluster as a model system for larger InP nanostructures, we have replicated the carboxylate exchange experiment on larger InP quantum dots. These particles were purified in the same manner as the cluster and determined to be 3 nm by TEM analysis. Solution concentrations were determined via the literature extinction coefficient values[66] and the exchange was carried out over a similar range to the cluster on a percent ligand basis using the same oleate starting and DDA titrant system.

The results of this exchange were indeed similar to those seen in the cluster case. Attempting to model the exchange mechanism as pure X-type metathesis yielded a similar non-linear fit to K_{eq} that was much-improved upon use of isotherm fitting via equation 2.3 (Figure 2.9). The experimental value for the X-type equilibrium was measured to be $KX_{eq} = 0.88$. This value is in strong agreement with the cluster system. The ratio of L- to X-type sites was calculated to be approximately 10% of total sites, which is significantly less than the 15% seen in the cluster case. A decrease in available surface-In concentration with increasing particle size has been recently computationally predicted to be as much as 30% lower for a 3.28 nm nanoparticle as compared to the $In_{37}P_{20}X_{51}$ cluster.[45] This change would naturally lead to a decrease in the L- to X-type ligand ratio as there are fewer sites in general to bind and X-type coordination takes priority for charge balance requirements. The absolute number of bound ligands on a per particle basis was also found to be lower than expected. At 98 bound ligands per particle there are approximately 25% fewer bound ligands than literature and geometric considerations would otherwise predict on a per particle basis.[45,66] This discrepancy could reasonably be attributed to ligand stripping from over-purification as has been observed previously,[67,68] or simply error arising from the inherent difficulty in quantifying nanoparticle concentrations. Overall, the nanoparticle system is demonstrably similar to the cluster system with nearly equivalent relative ligand affinities in conjunction with a predictable decrease in L-site availability.

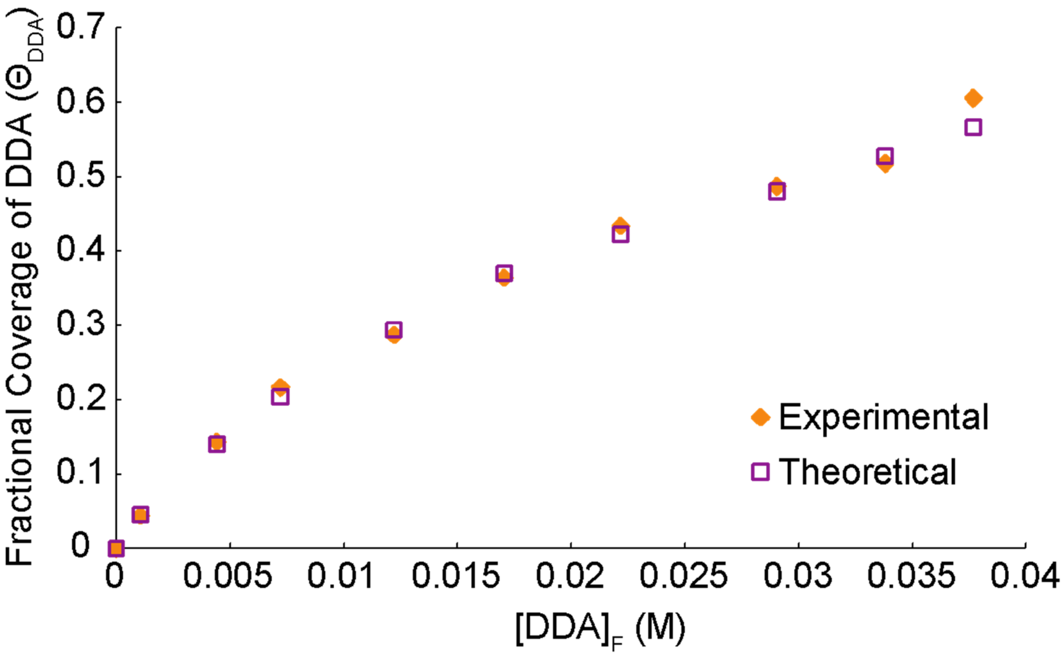

Figure 2.9. Isotherm fitting via equation 2.4 of DDA titration into a solution of oleate capped InP QDs from 0 eq to 110 equivalents. This fit gives the following values: $KX_{eq} = 0.88$, $KL_{DDA} = 2.3$, $KL_{Ol} = 3.5$, nX = 88, nL = 10.

2.3 Conclusion

Ligand shells are a complex and relatively poorly understood aspect of colloidal nanostructures. We have shown that on colloidal InP, ligative properties can vary greatly depending on the ligand identity, but that their binding can be reliably and quantitatively modeled. By using an InP cluster as a molecularly precise starting point and alkene-labeled ligands, we are able to quantitatively model the ligand binding dynamics in an atomically precise manner using ^{1}H NMR spectroscopy. Using dodec-11-enoic acid, we demonstrate the broad similarity of the cluster coordination chemistry to that of larger quantum dots of InP and CdSe. By modeling the equilibrium between DDA and the starting oleate ligands using an isotherm-based approach, we are able to for the first time deconvolute and quantify carboxylic acid L-type binding to a nanoparticle surface as accounting for 10-20% of total ligand binding at saturation. Given the net increase in entropy associated with this type of binding and the change in ^{31}P symmetry seen upon the binding of phosphonate and thiol, we suggest that both X- and L-type exchanges are concomitant with surface carboxylates shifting from bidentate to monodentate and more significant structural perturbations in the case of strongly binding ligands. 10-Undecyl-1ene thiol was found to bind more strongly than oleate with no tendency towards L-type binding or disulfide formation but was observed to cause decomposition before complete exchange. Finally, undecyl-10-ene phosphonic acid was found to bind irreversibly and at a strict 2:1 stoichiometry for oleate as has been observed in several material systems. This binding was largely free from decomposition below the complete exchange limit, beyond which InP-phosphonate oligomers began to develop. Ultimately, we believe that observations and analytical techniques such as these will underpin future development of nanoparticle synthesis and technological translation via an improvement in rational surface design. Methodological development in post-synthetic surface modification, including shelling for improved photophysical properties and ligand exchange for improved charge transport, will require a detailed understanding of the relative binding strengths of ligands as well as ligand decomposition pathways to achieve maximal utility.

2.4 Experimental

2.4.1 General Practices

Unless stated otherwise, all chemical reactions were performed under N_2 using standard Schlenk line air-free techniques and glassware. Chemicals were stored in a N_2 glovebox dried unless stated otherwise. Standard solutions were prepared immediately prior to use.

2.4.2 Experimental Procedures, Synthetic:

2.4.2.1 Synthesis of dodec-11-enoic acid (DDA):

DDA was synthesized via a Grignard reaction. A 100 mL Schlenk flask under nitrogen was charged with 30mL dry THF, 333 mg of Mg (3 eq), and one flake of I_2. Once the yellow color had dissipated, 4.0 g (17.1 mmol, 1.0 eq) of 11-bromo-1-undecene was added. The vessel was brought to 40 °C under N_2 with stirring for 2 hr, and a deep gold developed. A cannula was then used to sparge the solution with CO_2 for 1 hr. The solution was decanted and worked up with excess 1.0 M HCl and ammonium chloride. Following this it was extracted three times with saturated brine solution. The organic layer was concentrated by rotovap and purification was performed by column chromatography with a 1:8 ether:hexanes eluent followed by repeated washes with cold pentane. The product was a white powder with a tendency to melt from handling.

2.4.2.2 Synthesis of 10-undecene-1-thiol (UDTh):

UDTh was synthesized using a modified literature procedure via the synthesis and subsequent reduction of thioester.[69] A 50 mL round bottom flask was loaded with 15 mL dry ethanol and 1.96 g potassium thioacetate (17.1 mmol, 1.0 eq) and sonicated until a homogenous but opaque pink color. A separate solution of 15 mL dry ethanol and 4.0 g 11-bromo-1-undecene (17.1 mmol, 1.0 eq) was prepared and both solutions were sparged with nitrogen for 30 m. The solutions were then combined in the round bottomed flask, equipped with a condensing column, and refluxed for 18 hr under nitrogen. The resulting product was a dark orange with white precipitate and was extracted three times with 50 mL pentane. This solution was concentrated by rotovap down to an oil and purified by silica column using a 1:10 ether:hexanes eluent. The product was concentrated and confirmed by ^{1}H NMR to be S-(undec-10-en-1-yl) ethanthioate (2.54 g, 65% yield). A 100 mL Schlenk flask was loaded with 740 mg $LiAlH_4$ (1.75 eq) and under nitrogen and cooled to 0 °C in an ice bath. The thioester was resuspended in 5 mL dry ether and added dropwise with stirring. The solution was then removed from the ice bath and allowed to stir for 1 hr. The mixture was quenched with 15 mL of 1.0 M HCl and filtered over Celite on a glass frit. The organic layer was dried over $MgSO_4$ and concentrated via rotovap to a clear oil yielding 10-undecene-1-thiol which was degassed and stored immediately in a glovebox freezer and used without further purification.

2.4.2.3 Synthesis of 10-ene-undecyl-phosphonic acid (UDPA):

UDPA was synthesized from 11-bromo-1-undecene via the Michaelis-Arbuzov reaction. In a Schlenk flask 3.0 g (12.9 mmol, 1.0 eq) of 11-bromo-1-undecene was combined with 6.2 mL distilled triethyl phosphite (38.6 mmol, 3.0 eq) and refluxed under nitrogen at 150 °C for 16 hr. Excess triethyl phosphite was removed by vacuum assisted distillation leaving a yellow oil and complete conversion was verified by ^{31}P NMR spectroscopy. The flask was refilled with nitrogen and placed in an ice bath where a solution of 3.6 mL tris(trimethylsilyl)bromide in 10 mL dry toluene (27.1 mmol, 2.1 eq) was slowly injected. The flask was gently raised to 50 °C and allowed to stir for 2 hr where complete conversion was seen by ^{31}P NMR spectroscopy. Toluene and volatiles were removed via distillation and the reaction was worked up with a dilute solution of HCl. The product was purified by four repeated recrystallizations from hot hexanes yielding white crystalline flakes.

2.4.2.4 Synthesis of the $In_{37}P_{20}$ Cluster $[In_{37}P_{20}(O_2C_{18}H_{33})_{51}]$

Oleate ligated cluster was synthesized via the established literature procedure using in-situ formed $In(Ol)_3$.[70] After synthesis the clusters were taken into a glovebox where they were flocculated out of solution with acetonitrile. The crude material was purified by two elutions through a size-exclusion column using a BioBead stationary phase,[67] followed by further resuspensions in toluene and acetonitrile flocculation until no free acid was visible by NMR spectroscopic analysis. The clusters were dried under vacuum and stored as a solid with a wax consistency.

2.4.2.5 Synthesis of InP QDs

The InP QDs used were synthesized by heatup of oleate-capped cluster.[71] A solution of 200 mg as prepared cluster was dissolved in 10 ml octadecene and transferred to a 3-neck flask on the Schlenk line. The solution was raised to 280 °C at a rate of 10 °C/min. The solution was held at temperature for 1 hr, then allowed to cool. After vacuum assisted distillation at 120 °C the QD's were purified in the same manner as the cluster.

2.4.2.6 Titrations

Samples of 20.0 mg of cluster (1.04 μmol) were weighed and suspended in 400 μL C6D6, or in the case of variable temperature experiments toluene-d8. Prior to use, deuterated solvents were prepared with mesitylene as an internal standard at a concentration of 0.050 M. Sufficient delay time was determined via the inversion recovery experiment of mesitylene. Titrating solutions were prepared using this internally standardized solvent for each sample at a concentration of 1 equivalent ligand/ 10 μL of solvent. Between trials the J Young tube was brought into the glovebox where the appropriate amount of titrant was added via microliter syringe. Amounts beyond 50 eq (~10 mg) were weighed and added neat. The sample was allowed 30 min to equilibrate with agitation between additions.

2.4.3 Experimental Procedures, Analytical

2.4.3.1 UV-Vis Spectrometry

Ex situ UV-Vis spectra were measured using a Varian Cary model 5000 dual beam spectrometer. The spectrometer was equipped with a Mercury light source and measurements were made with 1 nm resolution between 300 and 800 nm. Samples were loaded into polished quartz cuvettes for analysis.

2.4.3.2 NMR ^{1}H and ^{31}P{^{1}H} Spectrometry:

^{1}H and ^{31}P{^{1}H} spectra were acquired on a Bruker base 700 MHz frequency instrument using a BBO ^{1}H{X} probe unless otherwise stated. Deuterated solvents were acquired from Cambridge Isotope Labs and dried over calcium hydride, vacuum-transferred, and stored over 4 Å sieves in a nitrogen glovebox. For ^{1}H NMR spectra mesitylene was used as an internal standard and reference, while for ^{31}P NMR spectra 85% phosphoric acid was used as an external reference. A 30° tilt pulse sequence was used to reduce quantitative delay times. Pulse and shim recalibrations were performed between all temperature changes during variable temperature experiments.

2.4.3.3 NMR DOSY Spectrometry:

DOSY spectra were acquired on a Bruker 500 MHz instrument using a TXO{^{1}H} probe. A basic STE DOSY pulse sequence with a single gradient was used. The gradient dimension was acquired over 32 evenly spaced datapoints from 5% to 90% gradient strength at 8 scans each. Scans were run using a T_1 delay of 30 s and a DOSY gradient pulse Δ delay of 400 ms.

2.4.4 Deriving a multi-site, multi-species-competitive Langmuir isotherm in terms of measurable variables:

A site balance on site-type *n* for multiple adsorbate species *i* is described by:

$$[S_n] = [S_{n0}] - \sum_i [i_{n,ad}] \tag{2.5}$$

Where individual equilibria are described by kinetics in the Langmuir model as:

$$[i_{n,ad}] = K^i_{eq,n}[S_n][i_f] \tag{2.6}$$

Combining (2.5) and (2.6) one can define the fractional occupation of site-type *n* by species *j*:

$$\Theta_{n,j} = \frac{K^j_{eq,n}\,[j_f]}{1 + \sum_i K^i_{eq,n}\,[i_f]} \tag{2.7}$$

Summing over all site-types, the total fractional occupancy by species *j* becomes:

$$\Theta_j = \sum_n \chi_n \frac{K^j_{eq,n}\,[j_f]}{1 + \sum_i K^i_{eq,n}\,[i_f]} \tag{2.8}$$

Using (2.8) one can rewrite (2.7) in the context of nanoparticles of concentration [NP] with z_n number of sites of type *n* per-particle:

$$\Theta_j = \frac{[j_{ad}]}{\sum_n z_n [NP]} \tag{2.9}$$

$$[j_{ad}] = [NP] \sum_n z_n \frac{K^j_{eq,n}\,[j_f]}{1 + \sum_i K^i_{eq,n}\,[i_f]} \tag{2.10}$$

(2.10) is general for $n \geq 1$ and $i \geq 1$, reducing to the competitive Langmuir isotherm for $n = 1$ and the multisite Langmuir isotherm for $i = 1$.

For example, the concentration of adsorbed oleate (Ol) competing with dodec-11-enoic acid (DDA) for L and X type sites becomes:

$$[Ol_{Ad}] = [NP]\left(z_L \frac{K_{eq,L}^{Ol}\left[Ol_f\right]}{1 + K_{eq,L}^{Ol}\left[Ol_f\right] + K_{eq,L}^{DDA}\left[DDA_f\right]} + z_X \frac{K_{eq,X}^{Ol}\left[Ol_f\right]}{1 + K_{eq,X}^{Ol}\left[Ol_f\right] + K_{eq,X}^{DDA}\left[DDA_f\right]}\right) \qquad (2.11)$$

And

$$[DDA_{Ad}] = [NP]\left(z_L \frac{K_{eq,L}^{DDA}\left[DDA_f\right]}{1 + K_{eq,L}^{DDA}\left[DDA_f\right] + K_{eq,L}^{Ol}\left[Ol_f\right]} + z_X \frac{K_{eq,X}^{DDA}\left[DDA_f\right]}{1 + K_{eq,X}^{DDA}\left[DDA_f\right] + K_{eq,X}^{Ol}\left[Ol_f\right]}\right) \qquad (2.12)$$

Definitions:

$[S_{n0}]$	Total concentration of sorption sites of type *n*
$[S_n]$	Concentration of open sites of type *n*
$[i_{n,ad}]$	Concentration of species *i* bound on *n*-sites
$[i_{ad}]$	Concentration of species *i* bound on all sites (i.e. $\sum_n [i_{n,ad}]$)
$[i_f]$	Concentration of species *i* free in solution
$K^i_{eq,n}$	Equilibrium constant of species *i* towards *n*-site type binding
$\Theta_{n,i}$	Fractional occupancy of species *i* over *n*-type sites (i.e. $[i_{n,ad}] / [S_{n0}]$)
χ_n	Fraction of total sites that are type *n* (i.e. $[S_{m0}] / \sum_n [S_{n0}]$)
Θ_i	Fractional occupancy of species *i* over all sites (i.e. $[i_{ad}] / \sum_n [S_{n0}]$)
[NP]	Concentration of nanoparticles
z_n	Number of sites of type *n* per nanoparticle (i.e. $[S_{n0}] = z_n[NP]$)

A note on X-type binding in this model:
Modeling X-Type binding using the Langmuir model physically implies a sorption reaction of:

$$X^- + NP^+ \rightleftarrows XNP$$

Which is a physically unreasonable reaction in non-polar solvent. However, the net combination of two such reactions:

$$XA^- + NP^+ \overrightarrow{K_{XA}} XANP$$

$$XB^- + NP^+ \overrightarrow{K_{XB}} XBNP$$

$$(XBNP \ \overrightarrow{K_{XB}^{-1}} XB^- + NP^+)$$

Reduces at equilibrium to the X-Type exchange reaction for reversible reactions A and B:

$$XA^- + XBNP \ \overleftrightarrow{K_{XA}/K_{XB}} \ XANP + XB^-$$

Thus if the reactions are at equilibrium and the exchange is one-to-one the net X-type equilibrium constant can be directly obtained from the isotherm variables:

$$K_{eq,X} = \frac{K_{eq,X}^{A}}{K_{eq,X}^{B}}$$

2.5 References

(1) Sambur, J. B.; Chen, P. Approaches to Single-Nanoparticle Catalysis. *Annu. Rev. Phys. Chem.* **2014**, *65* (1), 395–422. https://doi.org/10.1146/annurev-physchem-040513-103729.

(2) Xia, Y.; Yang, H.; Campbell, C. T. Nanoparticles for Catalysis. *Acc. Chem. Res.* **2013**, *46* (8), 1671–1672. https://doi.org/10.1021/ar400148q.

(3) Semonin, O. E.; Luther, J. M.; Beard, M. C. Quantum Dots for Next-Generation Photovoltaics. *Mater. Today* **2012**, *15* (11), 508–515. https://doi.org/10.1016/S1369-7021(12)70220-1.

(4) Lewis, N. S. Toward Cost-Effective Solar Energy Use. *Science* **2007**, *315* (5813), 798–801. https://doi.org/10.1126/science.1137014.

(5) Shirasaki, Y.; Supran, G. J.; Bawendi, M. G.; Bulović, V. Emergence of Colloidal Quantum-Dot Light-Emitting Technologies. *Nat. Photonics* **2013**, *7* (1), 13–23. https://doi.org/10.1038/nphoton.2012.328.

(6) Gao, X.; Yang, L.; Petros, J. A.; Marshall, F. F.; Simons, J. W.; Nie, S. In Vivo Molecular and Cellular Imaging with Quantum Dots. *Curr. Opin. Biotechnol.* **2005**, *16* (1), 63–72. https://doi.org/10.1016/j.copbio.2004.11.003.

(7) Kairdolf, B. A.; Smith, A. M.; Stokes, T. H.; Wang, M. D.; Young, A. N.; Nie, S. Semiconductor Quantum Dots for Bioimaging and Biodiagnostic Applications. *Annu. Rev.*

Anal. Chem. Palo Alto Calif **2013**, *6* (1), 143–162. https://doi.org/10.1146/annurev-anchem-060908-155136.

(8) Hu, M. Z.; Zhu, T. Semiconductor Nanocrystal Quantum Dot Synthesis Approaches Towards Large-Scale Industrial Production for Energy Applications. *Nanoscale Res. Lett.* **2015**, *10*. https://doi.org/10.1186/s11671-015-1166-y.

(9) Pu, Y.; Cai, F.; Wang, D.; Wang, J.-X.; Chen, J.-F. Colloidal Synthesis of Semiconductor Quantum Dots toward Large-Scale Production: A Review. *Ind. Eng. Chem. Res.* **2018**, *57* (6), 1790–1802. https://doi.org/10.1021/acs.iecr.7b04836.

(10) Bukowski, T. J.; Simmons, J. H. Quantum Dot Research: Current State and Future Prospects. *Crit. Rev. Solid State Mater. Sci.* **2002**, *27* (3–4), 119–142. https://doi.org/10.1080/10408430208500496.

(11) Johansen, J.; Stobbe, S.; Nikolaev, I. S.; Lund-Hansen, T.; Kristensen, P. T.; Hvam, J. M.; Vos, W. L.; Lodahl, P. Size Dependence of the Wavefunction of Self-Assembled InAs Quantum Dots from Time-Resolved Optical Measurements. *Phys. Rev. B* **2008**, *77* (7). https://doi.org/10.1103/PhysRevB.77.073303.

(12) Wang, F.; Wang, Y.; Liu, Y.-H.; Morrison, P. J.; Loomis, R. A.; Buhro, W. E. Two-Dimensional Semiconductor Nanocrystals: Properties, Templated Formation, and Magic-Size Nanocluster Intermediates. *Acc. Chem. Res.* **2015**, *48* (1), 13–21. https://doi.org/10.1021/ar500286j.

(13) Jia, G.; Xu, S.; Wang, A. Emerging Strategies for the Synthesis of Monodisperse Colloidal Semiconductor Quantum Rods. *J. Mater. Chem. C* **2015**, *3* (32), 8284–8293. https://doi.org/10.1039/C5TC01234A.

(14) Reiss, P.; Protière, M.; Li, L. Core/Shell Semiconductor Nanocrystals. *Small* **2009**, *5* (2), 154–168. https://doi.org/10.1002/smll.200800841.

(15) Hines, D. A.; Kamat, P. V. Recent Advances in Quantum Dot Surface Chemistry. *ACS Appl. Mater. Interfaces* **2014**, *6* (5), 3041–3057. https://doi.org/10.1021/am405196u.

(16) Owen, J. The Coordination Chemistry of Nanocrystal Surfaces. *Science* **2015**, *347* (6222), 615–616. https://doi.org/10.1126/science.1259924.

(17) Talapin, D. V.; Nelson, J. H.; Shevchenko, E. V.; Aloni, S.; Sadtler, B.; Alivisatos, A. P. Seeded Growth of Highly Luminescent CdSe/CdS Nanoheterostructures with Rod and Tetrapod Morphologies. *Nano Lett.* **2007**, *7* (10), 2951–2959. https://doi.org/10.1021/nl072003g.

(18) Kim, K.; Yoo, D.; Choi, H.; Tamang, S.; Ko, J.-H.; Kim, S.; Kim, Y.-H.; Jeong, S. Halide–Amine Co-Passivated Indium Phosphide Colloidal Quantum Dots in Tetrahedral Shape. *Angew. Chem. Int. Ed.* **2016**, *55* (11), 3714–3718. https://doi.org/10.1002/anie.201600289.

(19) Park, J.; Kim, S.-W. CuInS2/ZnS Core/Shell Quantum Dots by Cation Exchange and Their Blue-Shifted Photoluminescence. *J. Mater. Chem.* **2011**, *21* (11), 3745–3750. https://doi.org/10.1039/C0JM03194A.

(20) Wang, X.-S.; Dykstra, T. E.; Salvador, M. R.; Manners, I.; Scholes, G. D.; Winnik, M. A. Surface Passivation of Luminescent Colloidal Quantum Dots with Poly(Dimethylaminoethyl Methacrylate) through a Ligand Exchange Process. *J. Am. Chem. Soc.* **2004**, *126* (25), 7784–7785. https://doi.org/10.1021/ja0489339.

(21) Groeneveld, E.; Witteman, L.; Lefferts, M.; Ke, X.; Bals, S.; Van Tendeloo, G.; de Mello Donega, C. Tailoring ZnSe–CdSe Colloidal Quantum Dots via Cation Exchange: From

Core/Shell to Alloy Nanocrystals. *ACS Nano* **2013**, *7* (9), 7913–7930. https://doi.org/10.1021/nn402931y.

(22) Petryayeva, E.; Algar, W. R.; Medintz, I. L. Quantum Dots in Bioanalysis: A Review of Applications across Various Platforms for Fluorescence Spectroscopy and Imaging. *Appl. Spectrosc.* **2013**, *67* (3), 215–252. https://doi.org/10.1366/12-06948.

(23) Merg, A. D.; Zhou, Y.; Smith, A. M.; Millstone, J. E.; Rosi, N. L. Ligand Exchange for Controlling the Surface Chemistry and Properties of Nanoparticle Superstructures. *ChemNanoMat* **2017**, *3* (10), 745–749. https://doi.org/10.1002/cnma.201700171.

(24) Zhang, Z.; Edme, K.; Lian, S.; Weiss, E. A. Enhancing the Rate of Quantum-Dot-Photocatalyzed Carbon–Carbon Coupling by Tuning the Composition of the Dot's Ligand Shell. *J. Am. Chem. Soc.* **2017**, *139* (12), 4246–4249. https://doi.org/10.1021/jacs.6b13220.

(25) Chang, C. M.; Orchard, K. L.; Martindale, B. C. M.; Reisner, E. Ligand Removal from CdS Quantum Dots for Enhanced Photocatalytic H $_2$ Generation in PH Neutral Water. *J. Mater. Chem. A* **2016**, *4* (8), 2856–2862. https://doi.org/10.1039/C5TA04136H.

(26) Samadpour, M.; Boix, P. P.; Giménez, S.; Iraji Zad, A.; Taghavinia, N.; Mora-Seró, I.; Bisquert, J. Fluorine Treatment of TiO2 for Enhancing Quantum Dot Sensitized Solar Cell Performance. *J. Phys. Chem. C* **2011**, *115* (29), 14400–14407. https://doi.org/10.1021/jp202819y.

(27) Shahid, R.; Gorlov, M.; El-Sayed, R.; Toprak, M. S.; Sugunan, A.; Kloo, L.; Muhammed, M. Microwave Assisted Synthesis of ZnS Quantum Dots Using Ionic Liquids. *Mater. Lett.* **2012**, *89*, 316–319. https://doi.org/10.1016/j.matlet.2012.08.143.

(28) Stein, J. L.; Mader, E. A.; Cossairt, B. M. Luminescent InP Quantum Dots with Tunable Emission by Post-Synthetic Modification with Lewis Acids. *J. Phys. Chem. Lett.* **2016**, *7* (7), 1315–1320. https://doi.org/10.1021/acs.jpclett.6b00177.

(29) Talapin, D. V.; Murray, C. B. PbSe Nanocrystal Solids for N- and p-Channel Thin Film Field-Effect Transistors. *Science* **2005**, *310* (5745), 86–89. https://doi.org/10.1126/science.1116703.

(30) Wall, M. A.; Cossairt, B. M.; Liu, J. T. C. Reaction-Driven Nucleation Theory. *J. Phys. Chem. C* **2018**, *122* (17), 9671–9679. https://doi.org/10.1021/acs.jpcc.8b01368.

(31) Knauf, R. R.; Lennox, J. C.; Dempsey, J. L. Quantifying Ligand Exchange Reactions at CdSe Nanocrystal Surfaces. *Chem. Mater.* **2016**, *28* (13), 4762–4770. https://doi.org/10.1021/acs.chemmater.6b01827.

(32) Anderson, N. C.; Hendricks, M. P.; Choi, J. J.; Owen, J. S. Ligand Exchange and the Stoichiometry of Metal Chalcogenide Nanocrystals: Spectroscopic Observation of Facile Metal-Carboxylate Displacement and Binding. *J. Am. Chem. Soc.* **2013**, *135* (49), 18536–18548. https://doi.org/10.1021/ja4086758.

(33) Weiss, E. A. Organic Molecules as Tools To Control the Growth, Surface Structure, and Redox Activity of Colloidal Quantum Dots. *Acc. Chem. Res.* **2013**, *46* (11), 2607–2615. https://doi.org/10.1021/ar400078u.

(34) Zhou, Y.; Buhro, W. E. Reversible Exchange of L-Type and Bound-Ion-Pair X-Type Ligation on Cadmium Selenide Quantum Belts. *J. Am. Chem. Soc.* **2017**, *139* (37), 12887–12890. https://doi.org/10.1021/jacs.7b05167.

(35) Kessler, M. L.; Starr, H. E.; Knauf, R. R.; Rountree, K. J.; Dempsey, J. L. Exchange Equilibria of Carboxylate-Terminated Ligands at PbS Nanocrystal Surfaces. *Phys. Chem. Chem. Phys.* **2018**, *20* (36), 23649–23655. https://doi.org/10.1039/C8CP04275F.

(36) Size-Tunable, Bright, and Stable PbS Quantum Dots: A Surface Chemistry Study - ACS Nano (ACS Publications) https://pubs.acs.org/doi/10.1021/nn103050w (accessed Oct 31, 2018).

(37) Wheeler, L. M.; Sanehira, E. M.; Marshall, A. R.; Schulz, P.; Suri, M.; Anderson, N. C.; Christians, J. A.; Nordlund, D.; Sokaras, D.; Kroll, T.; Harvey, S. P.; Berry, J. J.; Lin, L. Y.; Luther, J. M. Targeted Ligand-Exchange Chemistry on Cesium Lead Halide Perovskite Quantum Dots for High-Efficiency Photovoltaics. *J. Am. Chem. Soc.* **2018**, *140* (33), 10504–10513. https://doi.org/10.1021/jacs.8b04984.

(38) Zhou, L.; Yu, K.; Yang, F.; Cong, H.; Wang, N.; Zheng, J.; Zuo, Y.; Li, C.; Cheng, B.; Wang, Q. Insight into the Effect of Ligand-Exchange on Colloidal CsPbBr3 Perovskite Quantum Dot/Mesoporous-TiO2 Composite-Based Photodetectors: Much Faster Electron Injection. *J. Mater. Chem. C* **2017**, *5* (25), 6224–6233. https://doi.org/10.1039/C7TC01611E.

(39) Gary, D. C.; Flowers, S. E.; Kaminsky, W.; Petrone, A.; Li, X.; Cossairt, B. M. Single-Crystal and Electronic Structure of a 1.3 Nm Indium Phosphide Nanocluster. *J. Am. Chem. Soc.* **2016**, *138* (5), 1510–1513. https://doi.org/10.1021/jacs.5b13214.

(40) De Nolf, K.; Cosseddu, S. M.; Jasieniak, J. J.; Drijvers, E.; Martins, J. C.; Infante, I.; Hens, Z. Binding and Packing in Two-Component Colloidal Quantum Dot Ligand Shells: Linear versus Branched Carboxylates. *J. Am. Chem. Soc.* **2017**, *139* (9), 3456–3464. https://doi.org/10.1021/jacs.6b11328.

(41) De Roo, J.; Yazdani, N.; Drijvers, E.; Lauria, A.; Maes, J.; Owen, J. S.; Van Driessche, I.; Niederberger, M.; Wood, V.; Martins, J. C.; Infante, I.; Hens, Z. Probing Solvent–Ligand Interactions in Colloidal Nanocrystals by the NMR Line Broadening. *Chem. Mater.* **2018**, *30* (15), 5485–5492. https://doi.org/10.1021/acs.chemmater.8b02523.

(42) Cho, E.; Jang, H.; Lee, J.; Jang, E. Modeling on the Size Dependent Properties of InP Quantum Dots: A Hybrid Functional Study. *Nanotechnology* **2013**, *24* (21), 215201. https://doi.org/10.1088/0957-4484/24/21/215201.

(43) Lee, D. G.; Sadar, M. H. The Basicity of Aliphatic Carboxylic Acids. *Can. J. Chem.* **1976**, *54* (21), 3464–3469. https://doi.org/10.1139/v76-497.

(44) Böhm, S.; Exner, O. Basicity of Carboxylic Acids: Resonance in the Cation and Substituent Effects. *New J Chem* **2005**, *29* (2), 336–342. https://doi.org/10.1039/B411039K.

(45) Zhao, Q.; Kulik, H. J. Electronic Structure Origins of Surface-Dependent Growth in III–V Quantum Dots. *Chem. Mater.* **2018**. https://doi.org/10.1021/acs.chemmater.8b03125.

(46) Denbigh, K. *The Principles of Chemical Equilibrium*, 3rd ed.

(47) Gary, D. C.; Petrone, A.; Li, X.; Cossairt, B. M. Investigating the Role of Amine in InP Nanocrystal Synthesis: Destabilizing Cluster Intermediates by Z-Type Ligand Displacement. *Chem Commun* **2017**, *53* (1), 161–164. https://doi.org/10.1039/C6CC07952K.

(48) Gaberle, J.; Gao, D. Z.; Watkins, M. B.; Shluger, A. L. Calculating the Entropy Loss on Adsorption of Organic Molecules at Insulating Surfaces. *J. Phys. Chem. C* **2016**, *120* (7), 3913–3921. https://doi.org/10.1021/acs.jpcc.5b12028.

(49) Wagner, G. W.; Fry, R. A. Observation of Distinct Surface Al $_{\mathrm{IV}}$ Sites and Phosphonate Binding Modes in γ-Alumina and Concrete by High-Field ^{27} Al and ^{31} P MAS NMR. *J. Phys. Chem. C* **2009**, *113* (30), 13352–13357. https://doi.org/10.1021/jp902474z.

(50) Owen, J. S.; Park, J.; Trudeau, P.-E.; Alivisatos, A. P. Reaction Chemistry and Ligand Exchange at Cadmium–Selenide Nanocrystal Surfaces. *J. Am. Chem. Soc.* **2008**, *130* (37), 12279–12281. https://doi.org/10.1021/ja804414f.

(51) Peng, Z. A.; Peng, X. Mechanisms of the Shape Evolution of CdSe Nanocrystals. *J. Am. Chem. Soc.* **2001**, *123* (7), 1389–1395. https://doi.org/10.1021/ja0027766.

(52) Wang, F.; Tang, R.; Kao, J. L.-F.; Dingman, S. D.; Buhro, W. E. Spectroscopic Identification of Tri- *n* -Octylphosphine Oxide (TOPO) Impurities and Elucidation of Their Roles in Cadmium Selenide Quantum-Wire Growth. *J. Am. Chem. Soc.* **2009**, *131* (13), 4983–4994. https://doi.org/10.1021/ja900191n.

(53) Prodanov, M. F.; Pogorelova, N. V.; Kryshtal, A. P.; Klymchenko, A. S.; Mely, Y.; Semynozhenko, V. P.; Krivoshey, A. I.; Reznikov, Y. A.; Yarmolenko, S. N.; Goodby, J. W.; Vashchenko, V. V. Thermodynamically Stable Dispersions of Quantum Dots in a Nematic Liquid Crystal. *Langmuir* **2013**, *29* (30), 9301–9309. https://doi.org/10.1021/la401475b.

(54) Tang, J.; Brzozowski, L.; Barkhouse, D. A. R.; Wang, X.; Debnath, R.; Wolowiec, R.; Palmiano, E.; Levina, L.; Pattantyus-Abraham, A. G.; Jamakosmanovic, D.; Sargent, E. H. Quantum Dot Photovoltaics in the Extreme Quantum Confinement Regime: The Surface-Chemical Origins of Exceptional Air- and Light-Stability. *ACS Nano* **2010**, *4* (2), 869–878. https://doi.org/10.1021/nn901564q.

(55) Xuan, T.; Yang, X.; Lou, S.; Huang, J.; Liu, Y.; Yu, J.; Li, H.; Wong, K.-L.; Wang, C.; Wang, J. Highly Stable CsPbBr3 Quantum Dots Coated with Alkyl Phosphate for White Light-Emitting Diodes. *Nanoscale* **2017**, *9* (40), 15286–15290. https://doi.org/10.1039/C7NR04179A.

(56) Gary, D. C.; Terban, M. W.; Billinge, S. J. L.; Cossairt, B. M. Two-Step Nucleation and Growth of InP Quantum Dots via Magic-Sized Cluster Intermediates. *Chem. Mater.* **2015**, *27* (4), 1432–1441. https://doi.org/10.1021/acs.chemmater.5b00286.

(57) Franz, R. G. Comparisons of PKa and Log P Values of Some Carboxylic and Phosphonic Acids: Synthesis and Measurement. *AAPS PharmSci* **2001**, *3* (2), 1–13. https://doi.org/10.1208/ps030210.

(58) Kroupa, D. M.; Vörös, M.; Brawand, N. P.; McNichols, B. W.; Miller, E. M.; Gu, J.; Nozik, A. J.; Sellinger, A.; Galli, G.; Beard, M. C. Tuning Colloidal Quantum Dot Band Edge Positions through Solution-Phase Surface Chemistry Modification. *Nat. Commun.* **2017**, *8*, 15257. https://doi.org/10.1038/ncomms15257.

(59) Frederick, M. T.; Weiss, E. A. Relaxation of Exciton Confinement in CdSe Quantum Dots by Modification with a Conjugated Dithiocarbamate Ligand. *ACS Nano* **2010**, *4* (6), 3195–3200. https://doi.org/10.1021/nn1007435.

(60) Giansante, C. Surface Chemistry Control of Colloidal Quantum Dot Band Gap. *J. Phys. Chem. C* **2018**, *122* (31), 18110–18116. https://doi.org/10.1021/acs.jpcc.8b05124.

(61) Bang, E.; Choi, Y.; Cho, J.; Suh, Y.-H.; Ban, H. W.; Son, J. S.; Park, J. Large-Scale Synthesis of Highly Luminescent InP@ZnS Quantum Dots Using Elemental Phosphorus Precursor. *Chem. Mater.* **2017**, *29* (10), 4236–4243. https://doi.org/10.1021/acs.chemmater.7b00254.

(62) Ryu, E.; Kim, S.; Jang, E.; Jun, S.; Jang, H.; Kim, B.; Kim, S.-W. Step-Wise Synthesis of InP/ZnS Core–Shell Quantum Dots and the Role of Zinc Acetate. *Chem. Mater.* **2009**, *21* (4), 573–575. https://doi.org/10.1021/cm803084p.

(63) Anderson, N. C.; Hendricks, M. P.; Choi, J. J.; Owen, J. S. Ligand Exchange and the Stoichiometry of Metal Chalcogenide Nanocrystals: Spectroscopic Observation of Facile Metal-Carboxylate Displacement and Binding. *J. Am. Chem. Soc.* **2013**, *135* (49), 18536–18548.

(64) White, J. R. Diffusion Coefficients of Fatty Acids and Monobasic Phosphoric Acids in *n* -Decane. *J. Chem. Phys.* **1955**, *23* (12), 2247–2251. https://doi.org/10.1063/1.1740732.

(65) Gary, D. C.; Petrone, A.; Li, X.; Cossairt, B. M. Investigating the Role of Amine in InP Nanocrystal Synthesis: Destabilizing Cluster Intermediates by Z-Type Ligand Displacement. *Chem Commun* **2017**, *53* (1), 161–164. https://doi.org/10.1039/C6CC07952K.

(66) Xie, L.; Shen, Y.; Franke, D.; Sebastián, V.; Bawendi, M. G.; Jensen, K. F. Characterization of Indium Phosphide Quantum Dot Growth Intermediates Using MALDI-TOF Mass Spectrometry. *J. Am. Chem. Soc.* **2016**, *138* (41), 13469–13472. https://doi.org/10.1021/jacs.6b06468.

(67) Roberge, A.; Stein, J. L.; Shen, Y.; Cossairt, B. M.; Greytak, A. B. Purification and In Situ Ligand Exchange of Metal-Carboxylate-Treated Fluorescent InP Quantum Dots via Gel Permeation Chromatography. *J. Phys. Chem. Lett.* **2017**, *8* (17), 4055–4060. https://doi.org/10.1021/acs.jpclett.7b01772.

(68) Doris, S. E.; Lynch, J. J.; Li, C.; Wills, A. W.; Urban, J. J.; Helms, B. A. Mechanistic Insight into the Formation of Cationic Naked Nanocrystals Generated under Equilibrium Control. *J. Am. Chem. Soc.* **2014**, *136* (44), 15702–15710. https://doi.org/10.1021/ja508675t.

(69) Minozzi, M.; Nanni, D.; Walton, J. C. Alkenylthioimidoyl Radicals: Competition between β-Scission and Cyclization to Dihydrothiophen-2-Ylidene-Amines. *Org. Lett.* **2003**, *5* (6), 901–904. https://doi.org/10.1021/ol034073+.

(70) Gary, D. C.; Flowers, S. E.; Kaminsky, W.; Petrone, A.; Li, X.; Cossairt, B. M. Single Crystal and Electronic Structure of a 1.3 Nm Indium Phosphide Nanocluster. *J Am Chem Soc* **2016**, *138*, 1510–1513.

(71) Gary, D. C.; Terban, M.; Billinge, S. J. L.; Cossairt, B. M. Two-Step Nucleation and Growth of InP Quantum Dots via Magic-Sized Cluster Intermediates. *Chem Mater* **2015**, *27*, 1432–1441.

Chapter 3. Templated Growth of InP Nanocrystals with a Polytwistane Structure

Adapted with permission from Angewandte Chemie. Copyright 2018 Wiley-VCH.

3.1 Introduction

Since the earliest discovery of emergent properties in nanoscale materials, the field of nanomaterial synthesis has advanced to afford access to a host of entirely new phases of matter not observed in the bulk. The ability to define structure at the nascent stage of nanocrystal nucleation has enabled the synthesis of a wide variety of non-thermodynamic structures, including Al, Ge, and Au clusters,[1–5] metal chalcogenide superlattices,[6–9] and molecule-like crystals of InP and CdSe,[10–13] many of which exhibit unique surface chemistry and optical properties, and all of which redefine the classical ideas of material phase and crystal synthesis. Such clusters often exhibit novel material phases. One such hypothesized nanoscale phase of matter is polytwistane.[14,15] Based on the monomer twistane, an isomer of adamantane displaying carbon rings in twist-boat conformation, polytwistane is a polymer that has been hypothesized to form chiral, ultra-thin, ultra-rigid, high surface area carbon nanotubes. Strain extended into the polymer by the twist-boat conformation poses a synthetic challenge, but also implies exciting physical and optoelectronic properties.[16]

Developing a rational understanding of the growth mechanisms of nanocrystals (NCs) is necessary in controlling material morphology at the atomistic level. Growing evidence suggests that classical mechanisms are in many cases insufficient to explain the formation of semiconductor NCs.[11,17–19] The existence of non-classical cluster intermediates during crystal growth have been shown to have profound implications on the growth kinetics of NCs.[17,20,21] These locally stable intermediates, so called magic-sized clusters (MSCs), are characterized by their molecule-like monodispersity, unusual stability, and in many cases their ability to seed the growth of kinetically accessible nanomaterial morphologies such as nanobelts, platelets, and pyramids.[7,9,13] This last feature has made MSCs intriguing synthons for templated nanomaterial synthesis and suggests that exploiting their unique structural properties can facilitate the synthesis of new nanoscale phases and morphologies.[22] Specifically, a close examination of a recently discovered InP MSC, $In_{37}P_{20}(O_2CR)_{51}$,[10] reveals a high-symmetry $In_{13}P_{14}$ core fragment displaying a structure of multiple polytwistane units helically intersecting in three dimensions. We hypothesize that extending this framework without molecular rearrangement[23] could result in InP nanostructures with a polytwistane crystal lattice.

In this work, we describe a kinetic, templated growth strategy to convert InP MSCs to larger nanomaterials without a concurrent transition to a more thermodynamically stable phase. This strategy enables the synthesis of InP NCs with the unprecedented three-dimensional polytwistane framework by kinetically trapping the phase of the MSC. We further examine reaction intermediates and propose a non-classical mechanism to explain the evolution of this structure type.

3.2 Results and Discussion

3.2.1 Templated Conversion of InP Cluster Using $P(SiMe_3)_3$

The $P(SiMe_3)_3$-induced conversion of $In_{37}P_{20}(O_2C(CH_2)_{12}CH_3)_3$ (InP MSC) into larger NCs was probed using in situ UV-Vis spectroscopy (Figure 3.1). The synthesis was carried out at 100 °C with 23 eq of $P(SiMe_3)_3$, both in excess over the empirical minimums for the reaction. At this temperature the MSC would not spontaneously thermally decompose ($t_{1/2}$ >5 hr at 150 °C), but any added $P(SiMe_3)_3$ would immediately react, thus allowing for a quantitative relation between the equivalents of $P(SiMe_3)_3$ added and the evolution of the NCs via their optical spectra.

The resulting in situ absorbance spectra demonstrated a broad and continuous redshift of the excitonic transition over nearly 0.7 eV, consistent with nanocrystal growth. During this period, nanocrystal polydispersity was maintained as indicated by the change in FWHM of the excitonic transition from 0.50 eV to 0.56 eV. Closer inspection of the optical change vs time (Figure 3.1, inset) reveals that the growth occurred across three distinct regimes. Regime I is an apparent induction period wherein the optical spectra show no appreciable shift, slowly accelerating by the addition of ca. 5 equivalents $P(SiMe_3)_3$. Given that the lowest energy MSC transitions have been previously assigned to molecular orbitals that reside primarily in the core of the MSC,[10] this observation does not discount the possibility of significant, surface-localized reactions. Regime II shows an extended period of nanocrystal growth with a strong correlation to the amount of $P(SiMe_3)_3$ added to the solution. Transition to the final regime occurs precisely at 17 equivalents, the stoichiometric point for conversion of all 51 carboxylate ligands in the MSC to silylester. Complete conversion is confirmed by ^1H NMR spectroscopy. The decrease in absorbance is thus rationalized by a loss of colloidal stability.

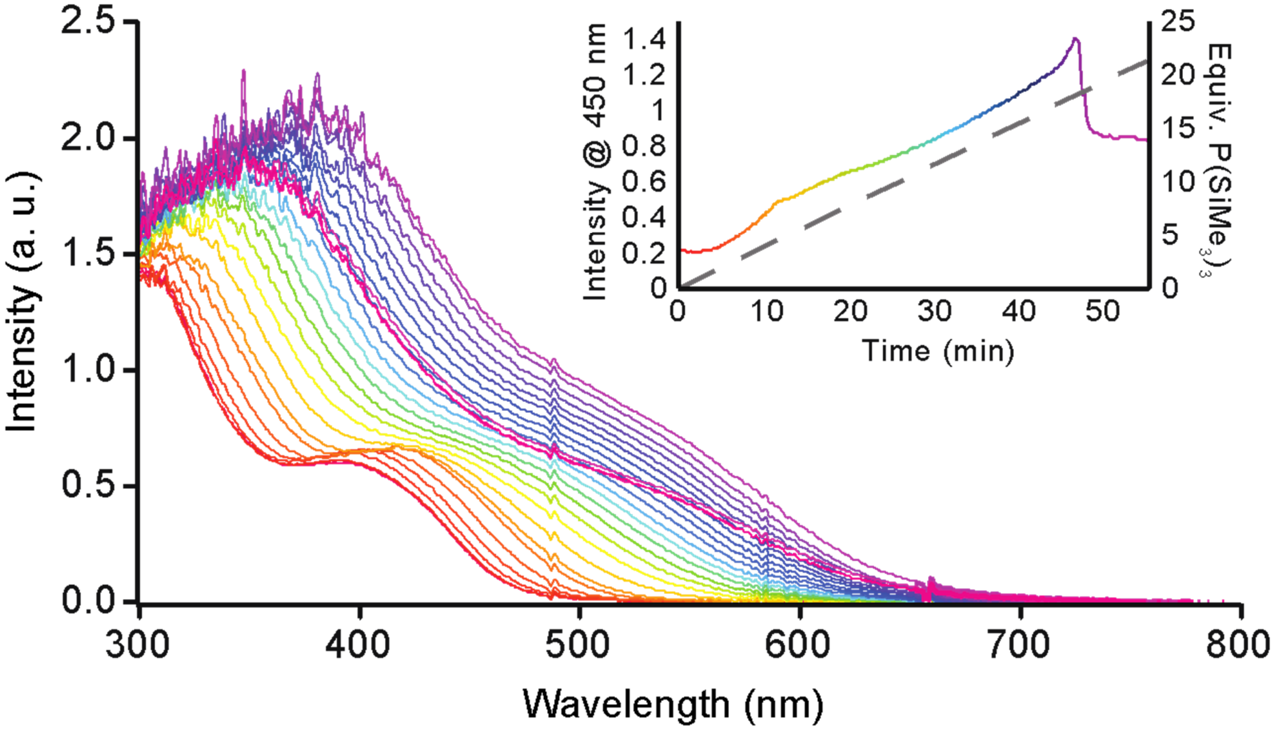

Figure 3.1. In-situ UV-Vis spectra of the reaction between $In_{37}P_{20}(O_2C(CH_2)_{12}CH_3)_3$ and 23 eq $P(SiMe_3)_3$ injected over 1 hr at 100 °C; traces displayed in 2.5 min increments. Inset: The shift in the absorbance at 450 nm vs time.

Similar trends are observed upon the rapid and complete addition of the $P(SiMe_3)_3$, as well as under conditions in which concentration (across two orders of magnitude) and temperature (35 - 125 °C) are varied (Figure 3.2). The temperature of this reaction was found to have a modest and non-linear impact on increasing product particle size.

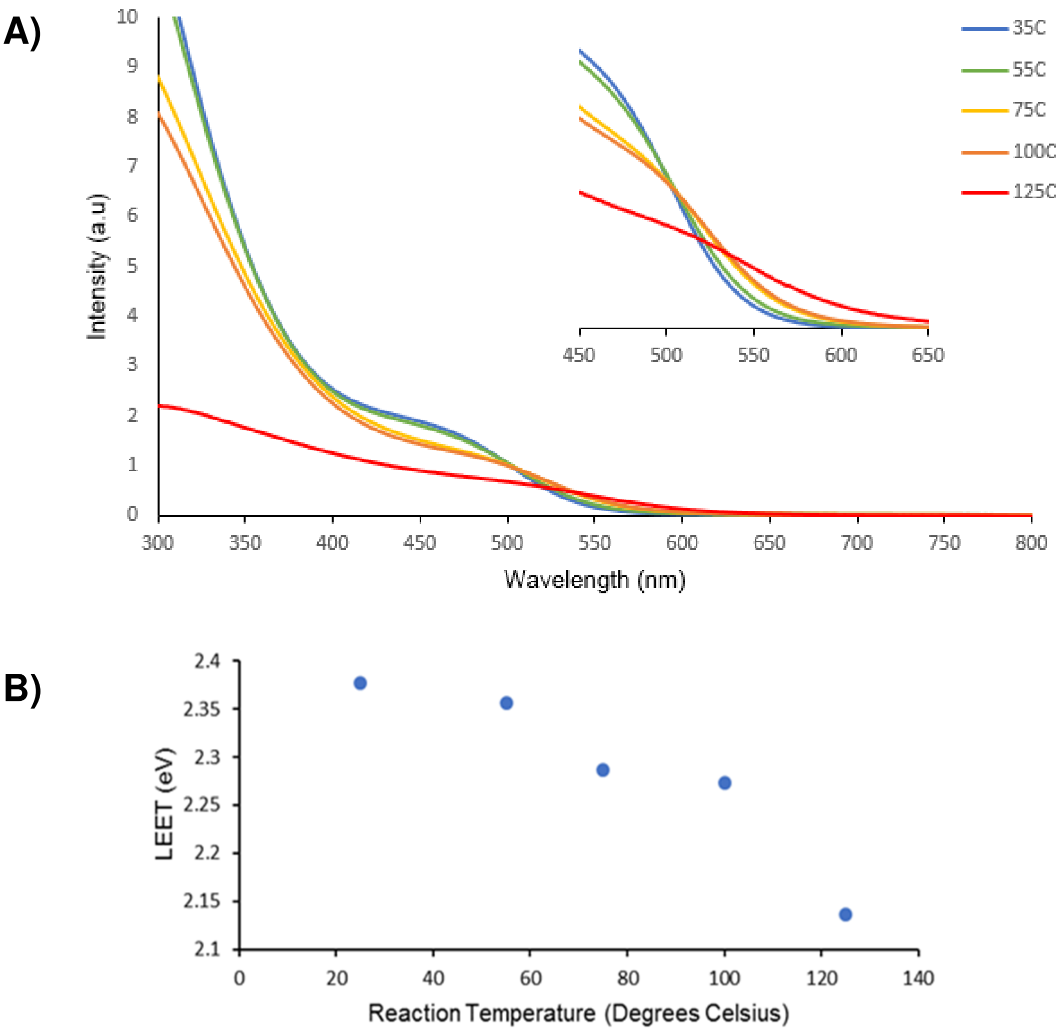

Figure 3.2. A) UV-Vis absorption spectra as a function of reaction temperature for the product QDs of the reaction between $In_{37}P_{20}$ and 15 equiv $P(SiMe_3)_3$ at standard concentration. B) The corresponding lowest energy excitonic transition energy as determined by Tauc intercepts of A.

A typical 100 °C synthesis generates NCs with a diameter of 2.93 (± 0.25) nm as evidenced by TEM analysis, and as would be expected from the position of the excitonic transition (2.4-2.1 eV) of this material.[24,25] The combination of dependence on temperature yet independence of starting

MSC concentration suggests a reaction mechanism that is rate limited by the conversion of an intermediate.

3.2.2. Structural Analyses Using XRD and SSNMR

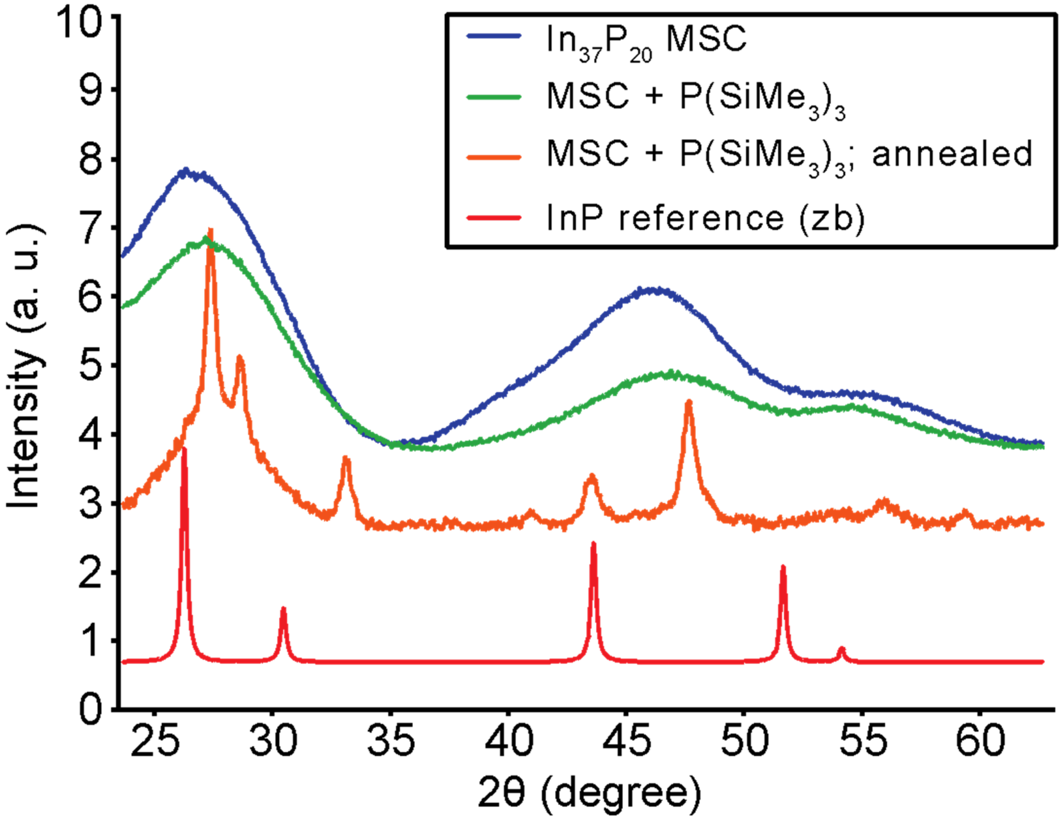

Figure 3.3. XRD Patterns of MSC and NCs collected with Cu K1-Alpha radiation, and InP reference pattern (ICDD PDF 00-032-0452).

The X-ray diffraction (XRD) patterns of the resulting NCs imply a greatly unaltered structure (Figure 3.3). Identical peak positions imply a perseverance of the MSC crystal phase whereas the lack of change in the FWHM implies that increasing synthesis temperature had no effect on the crystalline domain size of the NCs. These observations may be indicative of a unit cell that is large relative to the final NC size, or by the formation of highly defective NCs. Annealing a dried sample under dynamic vacuum at 275 °C does, however, yield a clearly corresponding and also novel diffraction pattern exhibiting increased crystalline domain size greater than 10 nm. Variance in the diffraction patterns is well explained by the convolution of these underlying peaks (Figure 3.4).

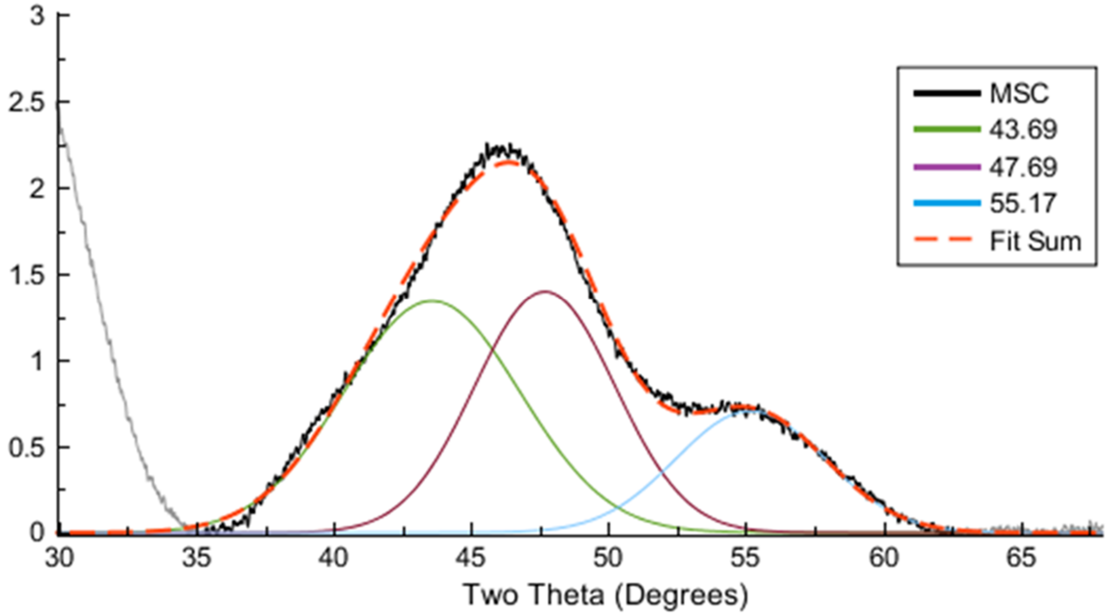

Figure 3.4. Comparison of standard $In_{37}P_{20}$ cluster (black) wide-angle X-ray diffraction peaks with the sum of three underlying gaussians centered at the cadmoindite ($CdIn_2S_4$) diffraction peak positions.

The annealed pattern has stark resemblance to the spinel mineral type, matching the thiospinel mineral Cadmoindite ($CdIn_2S_4$) to within d-spacing of 0.4%. We infer the formation of the near-isovalent In-P based analogue, with P replacing S, In replacing Cd, and a charge balancing vacancy, In_3P_3, which would represent the first phosphospinel in the literature to our knowledge. In this light, the MSC-phase may be a similar, incomplete, or defective form of this structure type.

Using Magic Angle Spinning (MAS) ^{31}P NMR spectroscopy we have observed that these NCs have a set of P environments distinct from both the starting MSC and zincblende InP (Figure 3.5 C). The predominantly observed P environment at −242 ppm matches exactly with what we have previously assigned to the "core" environment of the MSC (Figure 3a), further suggesting that this structure has been isotropically repeated during growth.

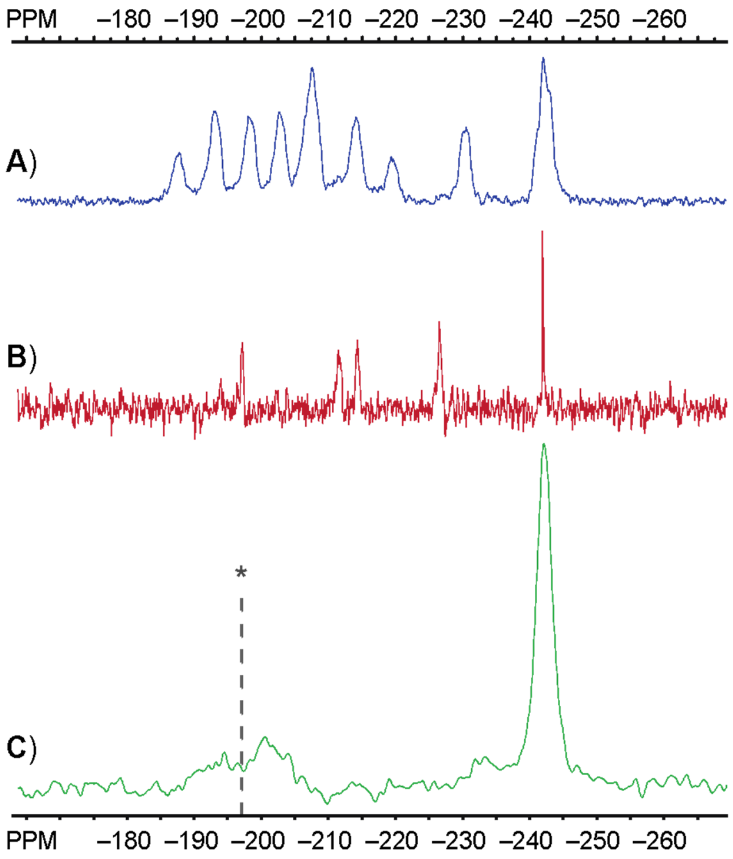

Figure 3.5. A) Solution ^{31}P NMR spectrum of the $In_{37}P_{20}$ MSC. B) Solution ^{31}P NMR spectrum of the $In_{37}P_{20}$ exposed to 2 eq $P(SiMe_3)_3$ over 120 hr, assigned as $In_{29}P_{14}(O_2CR)_{45}$. C) Solid state MAS ^{31}P NMR spectrum of NCs packed in boron nitride and grown via MSC conversion with $P(SiMe_3)_3$. Marked at −197 ppm is the literature reported resonance of zincblende InP NCs.[26]

We propose that this solution-phase cluster conversion reaction is leading to the templated growth of InP NCs into a 3D polytwistane structure. The structural relationship between twistane, polytwistane, and the MSC is shown in Figure 3.5. Polytwistane is a theoretical carbon nanotube-like morphology of carbon composed of 'twist' conformation six-membered rings with a structural connectivity exactly matching that of the InP MSC.[14] The MSC contains numerous, interlocking polytwistane units of identical chirality up to polytwistane-6. Such a structure has, to the best of our knowledge, never been described theoretically or experimentally prior to our observation of the $In_{37}P_{20}$ MSC. Although the crystal structure of the cluster does not contain a repeatable unit cell of this phase, the motif of isotropically interlocking twistane units is clearly extensible and its similarity to a spinel crystal structure is evident. Given the near-identical powder diffraction patterns of InP NCs synthesized via this $P(SiMe_3)_3$ method and the starting cluster, the resulting quantum dots strongly appear to have maintained the phase of the MSC, adopting neither the bulk zincblende nor wurtzite structure. Moreover, the annealed diffraction pattern corresponds to no known phase of any In, P, and/or O containing material.

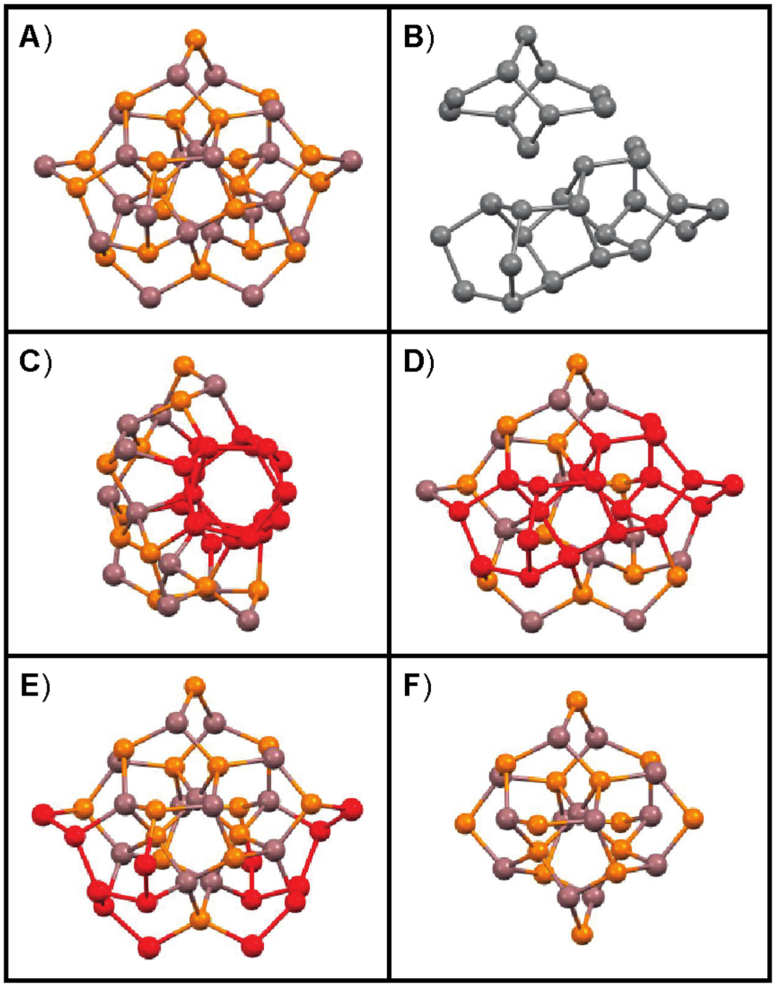

Figure 3.6. A) The $In_{21}P_{20}$ core of the $In_{37}P_{20}$ MSC (P=orange, In=purple). B) Twistane and (6)polytwistane, hydrogens omitted. C, D) One subunit of (6)polytwistane highlighted in the MSC. E, F) Hypothetical structure of $In_{13}P_{14}$ derived from the $In_{21}P_{20}$ core, etched atoms highlighted.

3.2.3 Investigation of Intermediary Cluster Species and a Growth Mechanism

Given the low C_2 symmetry of the starting InP MSC and the continuous, steady growth process observed by in situ UV-Vis analysis, direct cluster aggregation seemed like an unlikely mechanism to explain the observed nanocrystal formation. Interested in learning more about how the cluster transforms during this growth process, we examined the reaction between the InP MSC and low equivalents of $P(SiMe_3)_3$ (*vis a vis* Regime I) under more kinetically controlled conditions. Two equivalents of $P(SiMe_3)_3$ at room temperature resulted in a drastic blue shift in the MSC optical transition over a period of four days (Figure 3.7).

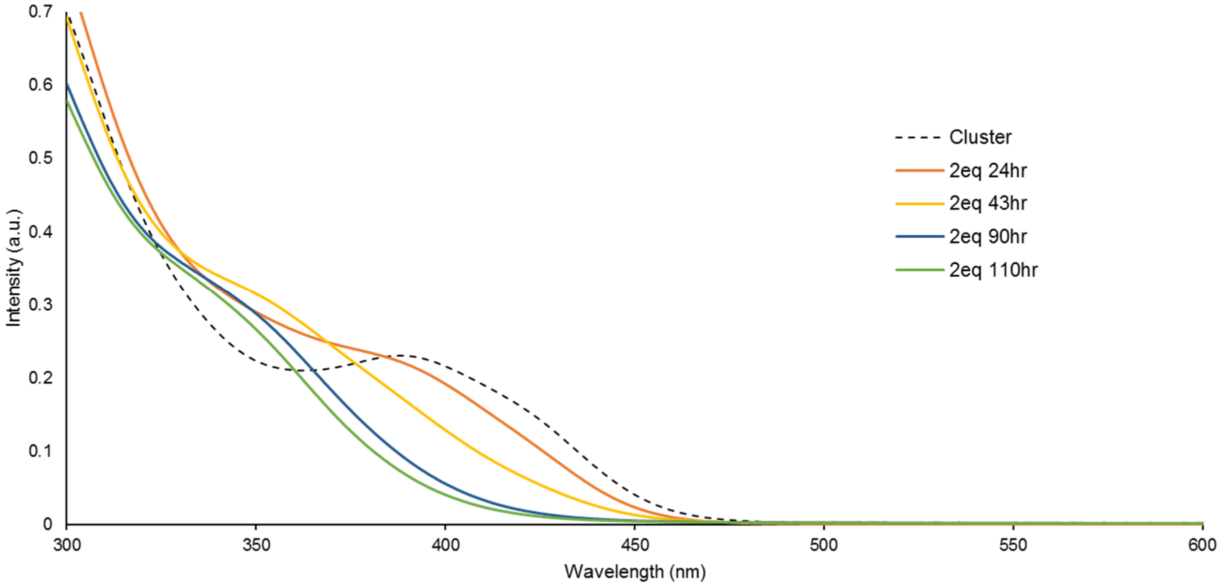

Figure 3.7. Evolution of the absorbance spectrum of $In_{37}P_{20}$ MSC with the addition of 2 equiv $P(SiMe_3)_3$ in toluene at room temperature over four days.

Figure 3.5B shows the ^{31}P NMR spectrum of the resulting product. Contrasted with the NMR spectrum of the starting $In_{37}P_{20}$ cluster, fewer distinct P environments are present, implying that this product has significantly higher symmetry and is plausibly smaller, an observation consistent with interpreting the blue shift as resulting from increased quantum confinement. Shrinkage is further consistent with an increase in diffusion constant as measured by DOSY ^1H NMR spectroscopy (Figure 3.8).

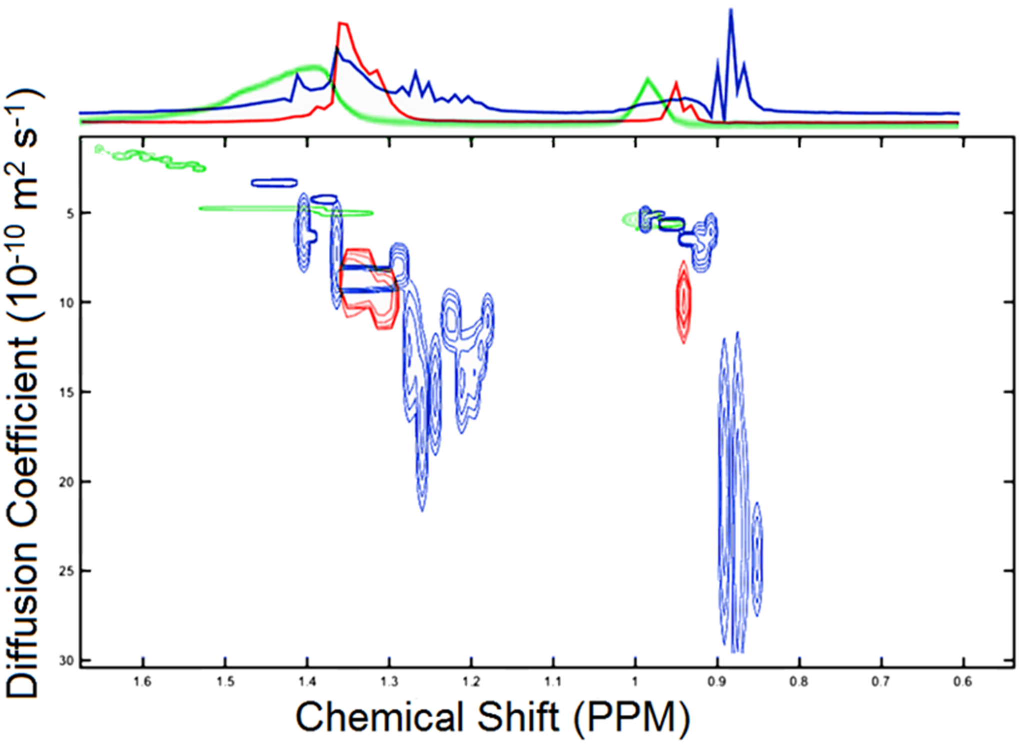

Sample	Region *(PPM)*	D$_0$ *(10^{-10} m^2 s^{-1})*	Assignment
MSC	1.55	1.5 ± 0.5	Cluster, Surface
	1.40	4.9 ± 0.4	Cluster, Outer Ligand
MSC +2eq	1.45	3.5 ± 0.5	Cluster, Surface
	1.38	6.25 ± 2	Cluster, Outer Ligand
	1.30	14 ± 5	Silyl Ester
In(Myr)$_3$	1.35	9 ± 1.5	In(Myr)$_3$

Figure 3.8. ^{1}H NMR DOSY diffusion spectra of $In_{37}P_{20}$ MSC, In-carboxylate, and the etched product of MSC with $P(SiMe_3)_3$ in toluene at room temperature.

Tellingly the XRD pattern of this species remains virtually unchanged from the initial MSC pattern indicating significant structural preservation. We hypothesize that the addition of $P(SiMe_3)_3$ destabilizes the MSC by removing carboxylate ligands in the form of silylester, and creating high energy surface P sites. The cluster responds by fragmentation, shrinking but not dissolving entirely to its "core" (Figure 3.6F), which is shown with its P atoms assigned to the observed ^{31}P NMR resonances, in strong agreement with near isoenvironmental assignments of the intact $In_{37}P_{20}$ MSC (Figure 3.9).

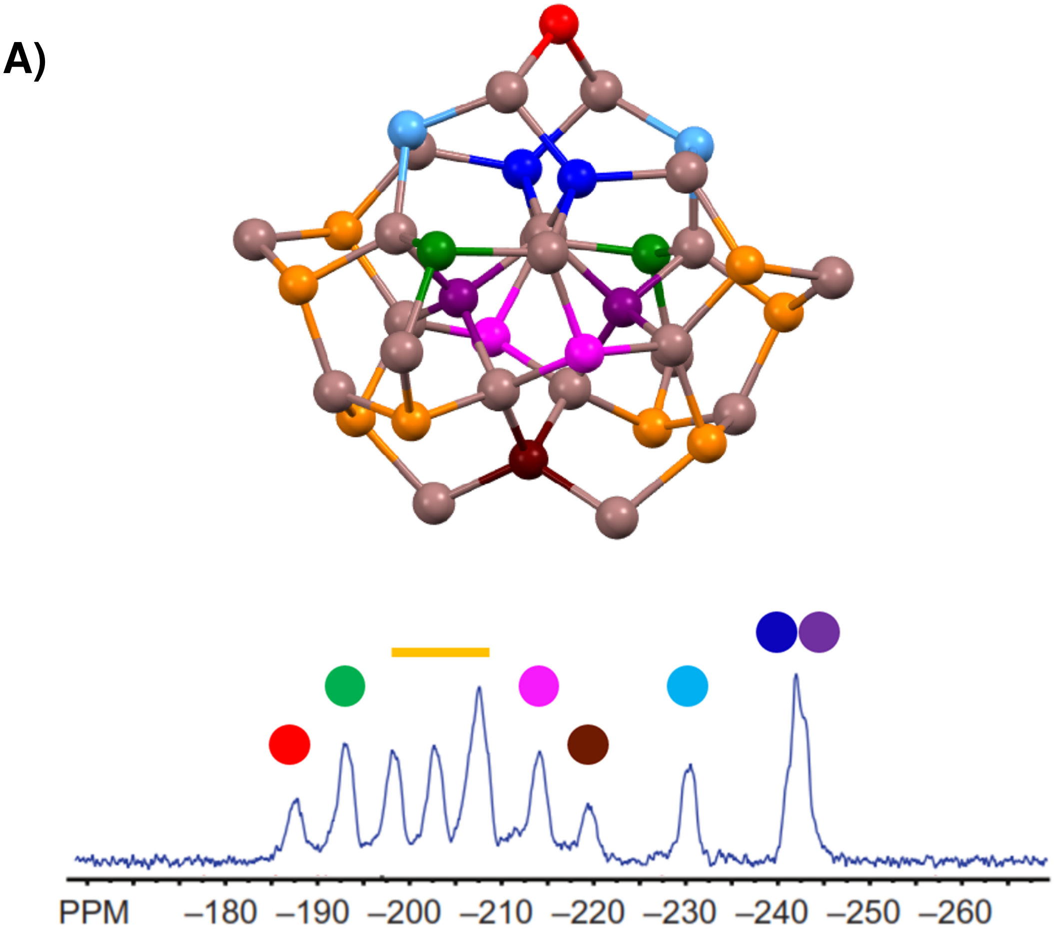

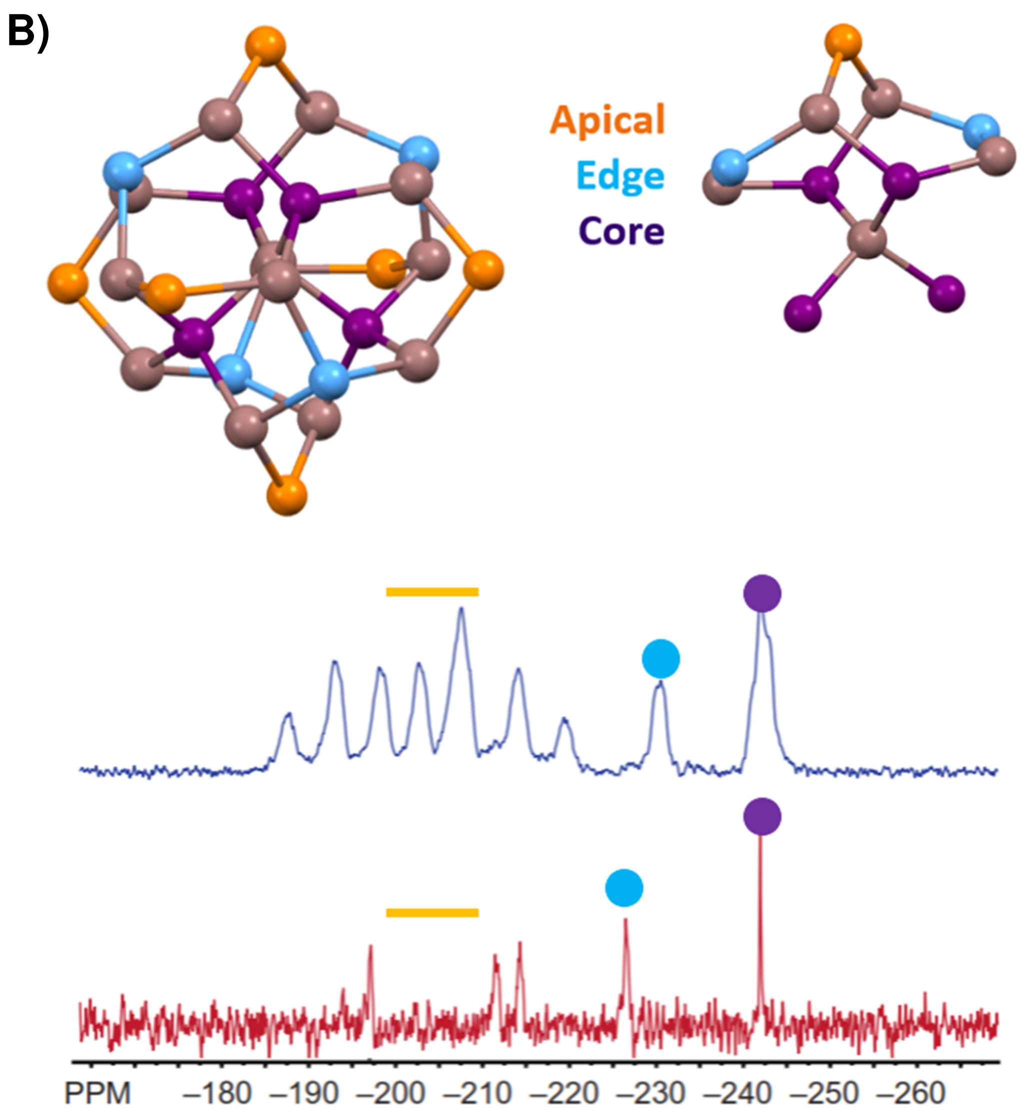

Figure 3.9. A) Structure from single crystal X-ray diffraction of the $In_{21}P_{20}$ core of the $In_{37}P_{20}$ cluster and corresponding ^{31}P spectrum and assignments. B) The proposed structure of the $In_{13}P_{14}$ core produced by etching with 2 equiv of $P(SiMe_3)_3$ at room temperature (Figure 3.7) and corresponding ^{31}P spectrum and assignments.

The fused inorganic core has T point group symmetry and chemical formula of $In_{13}P_{14}$. Based on the structure of the starting InP MSC, we anticipate all of the phosphorus atoms to have near-tetrahedral coordination with their coordination spheres completed by $In(O_2CR)_3$, resulting in a complete molecular formula of $In_{16}(In_{13}P_{14})(O_2CR)_{45}$. Ligation by indium carboxylate results in symmetry lowering and non-degeneracy of the 'surface P' environments as seen in the ^{31}P NMR spectrum (Figure 3B).[10,27] This formulation coincides perfectly with a balanced stoichiometric reaction between $In_{37}P_{20}(O_2CR)_{51}$ and 2 eq of $P(SiMe_3)_3$, as shown in Scheme 3.1.

$$In_{37}P_{20}(O_2CR)_{51} + 2\ P(SiMe_3)_3$$

$$\downarrow$$

$$In_{29}P_{14}(O_2CR)_{45} + 6\ Me_3SiO_2CR + 8\ [InP]$$

Scheme 3.1. A proposed reaction between the MSC and $P(SiMe_3)_3$.

The structure of this polytwistane core is rationalizable at the atomistic level as shown in Scheme 3.2. A slight deviation from zincblende during the early stages of nucleation readily drives the formation of the polytwistane phase. Atomistic growth or fragment addition can proceed to the formation of the MSC and beyond with no other perturbations necessary. By contrast, traditional colloidal InP syntheses in significant excess of 100 °C would have greater nuclei redissolution and favor a zincblende nucleus of lower chemical potential.[28,29] However, complete dissolution is not observed under the kinetic conditions described here. Moreover, given the fact that no excess clusters or fragments are visible in the final NC ^{31}P NMR spectrum, and that the MSC does not completely dissolve under these kinetic conditions, it can be inferred that multiple, partially dissolved cores must take part in surface $P(SiMe_3)_3$ driven aggregation processes in parallel or convolution with the recrystallization of liberated monomer.

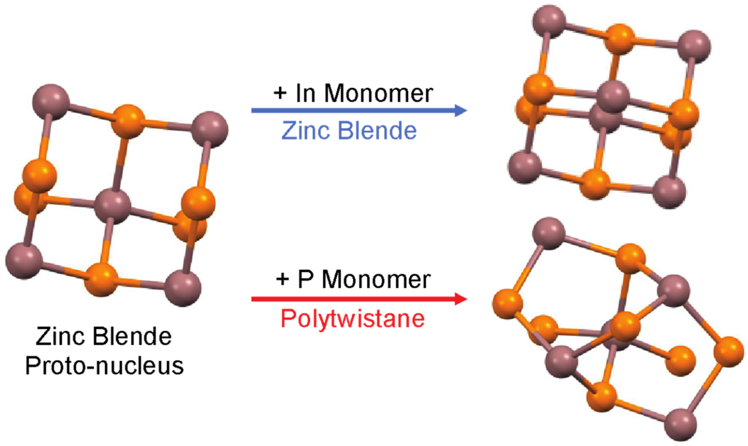

Scheme 3.2. A hypothetical, partially illustrated example of structural formation and solidification during proto-nucleation of InP.

3.2.4 Structural Evolution of InP Clusters and Quantum Dots Measured by In-Situ SAXS

In order to further quantify the structural evolution of colloidal InP nanomaterial during nucleation and growth, time-resolved in-situ small angle X-ray scattering (SAXS) measurements were obtained using a synchrotron X-ray source. Capillaries containing typical 2:1:3.6 stoichiometries of indium and phosphorus precursors and ligand were sealed in quartz capillaries inside an air free glovebox. While $P(SiMe_3)_3$ is known to react to form subsequent intermediates under these conditions no nucleation is observed at room temperature and the solution remains colorless. By loading the capillary into a heated sample holder nucleation can be initiated and measured in-situ as a function of time. The capillary heater was raised to 100 °C until no evolution in the scattering was observed, yielding a clear yellow solution.

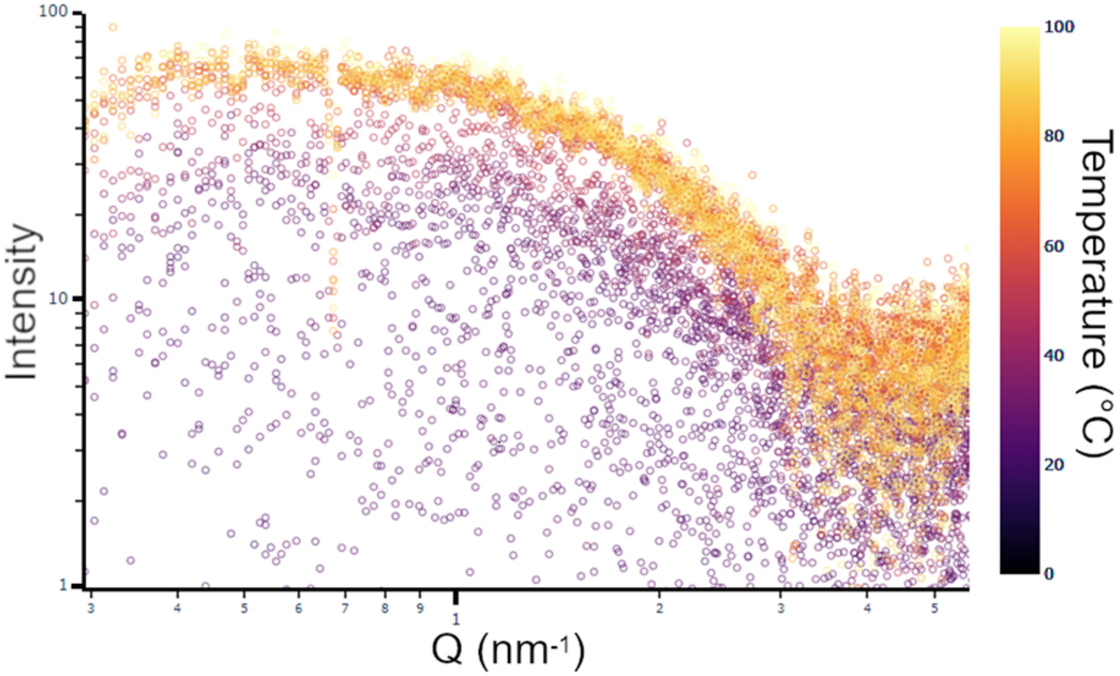

Figure 3.10. Stacked in-situ SAXS measurements of InP nucleation, heated from 20 to 100 °C at a rate of 5 °C per minute with 60 s integration time per acquisition.

At early time points below 50 °C no coherent scattering is observed from the solution which is consistent with the hypothesis that nucleation does not occur at room temperature. Coherent scattering begins to develop as the cell holder reaches approximately 50 °C. The development over time of this scattering is notably non-continuous. Scattering develops slowly within a band between 50 and 75 °C and appears to reach completion beyond 80 °C. Fitting using relatively simple solid sphere and ellipsoidal models was performed to investigate this structural evolution over time (Figure 3.11).

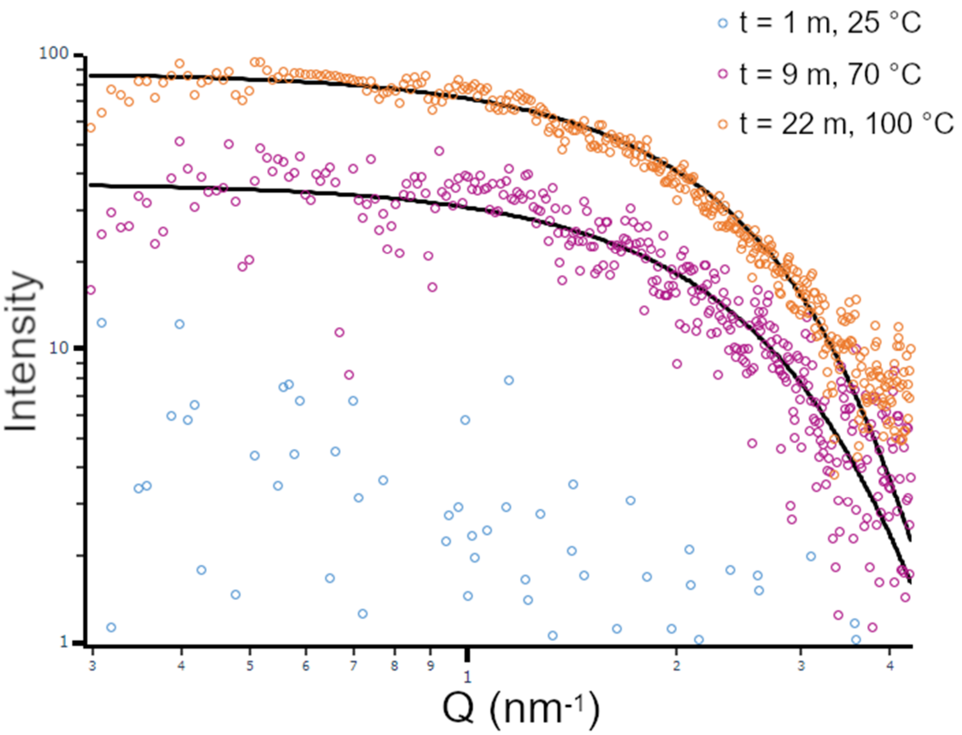

Figure 3.11. Selected time points of in-situ SAXS measurement of InP nucleation. Blue: 1 m, 25 °C, no fit shown. Purple: 9 m, 75 °C, the black line represents a modeled spherical fit with a 7 Å radius and 20 % ensemble polydispersity. Orange: 22 m, 100 °C, the black line represents a modeled ellipsoidal fit with a 6.5 Å equatorial radius and an 11 Å polar radius.

By 100 °C the product had stopped evolving and the scattering was fit to an ellipsoidal model fitting a 6.5 Å equatorial radius and an 11 Å polar radius. These dimensions closely reflect the dimensions and overall shape measured by single crystal X-ray crystallography being several bond lengths wider than tall and C_2V symmetric. By contrast, the first persistent band in the growth profile centered around 60 – 70 °C fit to a spherical model with a 7 Å radius with 20 % ensemble polydispersity. The improved fit to a more symmetric spherical model with roughly the same radial dimension is in strong agreement with the fragment isolated via decomposition of the $In_{37}P_{20}$ cluster (Figure 3.9). Observing such a species during the heating of precursors supports the hypothesis that the smaller cluster is an on-path intermediate and not purely the result of decomposition.

To further explore the growth pathways of InP NCs, similar experiments were performed on purified solutions of the $In_{37}P_{20}$ cluster in ODE solution heating to significantly higher temperatures up to 275 °C to induce growth of larger InP nanomaterials. For these experiments, we were additionally able to correlate the evolution of both the small and wide-angle X-ray scattering domains over time (Figure 3.12).

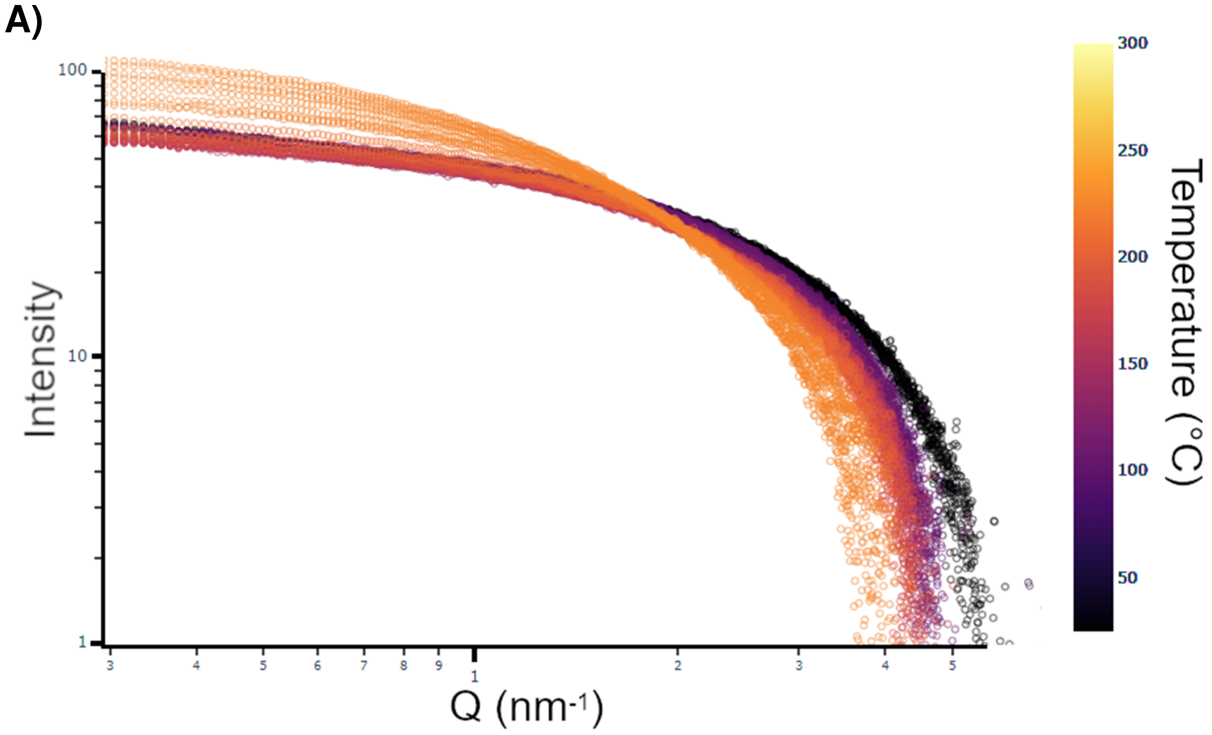

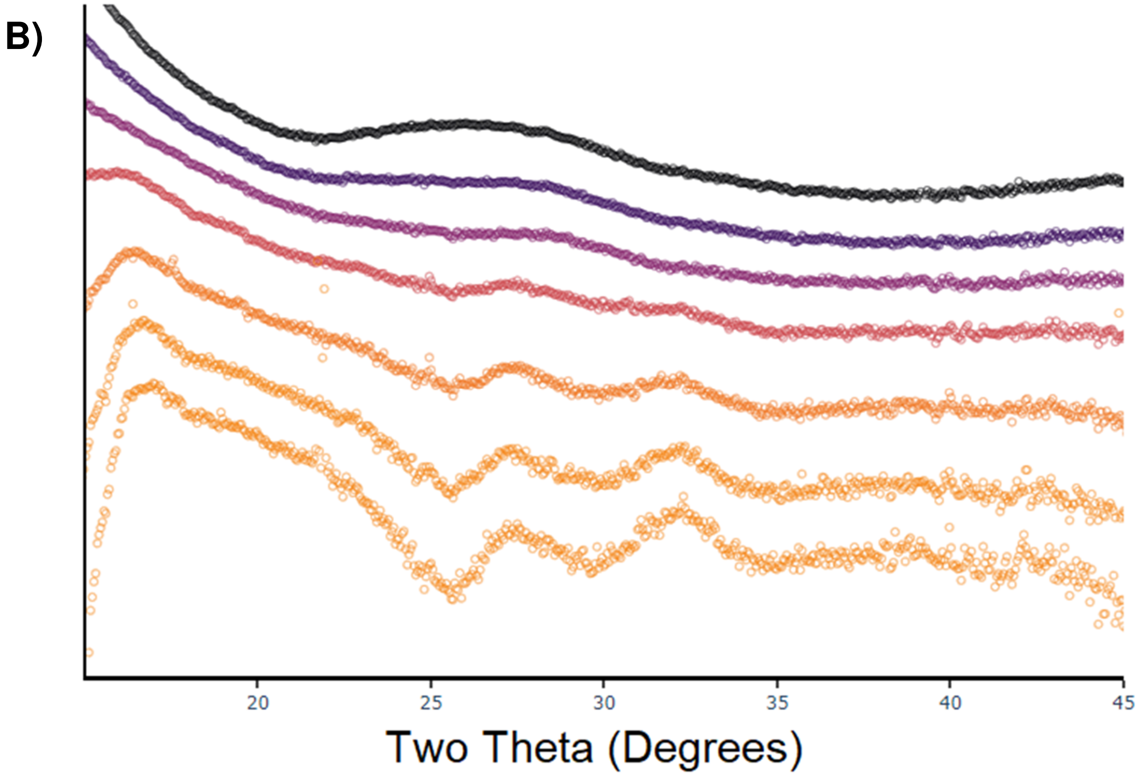

Figure 3.12. A) SAXS spectra collected of 10 mg/mL $In_{37}P_{20}$ cluster solution heated at a rate of 5 °C with 60 s integration time per acquisition. B) Corresponding WAXS spectra, shown at 8 m intervals.

The thermolysis of a cluster solution to form quantum dots is shown to proceed only once the solution is heated beyond 150 °C. This barrier is in good agreement with in and ex-situ measurements that measure the optical properties of the system as a function of time via UV-Vis spectroscopy. The observed growth of the ensemble of QDs by SAXS shows no signs of intermediate aggregative or anisotropic growth. The crystal phase measured in the wide-angle domain during cluster thermolysis (Figure 3.12 B) shows a clear conversion between the starting twistane phase to the bulk phase zinc blende final product. What this in-situ data reveals that ex-situ measurements do not, however, is that the conversion proceeds through decomposition of the initial phase and a re-growth into the zinc blende phase. This corroborates observations from NMR investigations that suggest InP cluster to QD conversion occurs through a decomposition pathway and not an aggregative pathway followed by annealing. If phase annealing were occurring the WAXS data should reveal a mixed or alloyed phase at intermediate times rather than the almost complete loss of crystalline scattering altogether as seen by ca. 22 m, 150 °C.

3.3 Conclusion

The conversion of InP precursors to colloidal nanomaterials demonstrably deviates from the classical La Mer mechanism of growth. The $In_{37}P_{20}$ cluster has been previously shown by our group to be an isolable intermediate along the growth pathway to larger QDs. However here we have further investigated kinetic and thermodynamic growth regimes to control the conversion of this intermediate to larger InP NCs. Under the kinetic surface-mediated growth regime we propose a full mechanistic scheme as follows: $P(SiMe_3)_3$ drives a surface decomposition event upon its reaction with the stabilizing carboxylate ligands of the MSC, forming silylester, and liberating InP monomers. Because the MSC does not dissolve entirely, its core-dominated optical properties remain largely unperturbed, likewise the crystalline phase naturally remains unchanged as observed in the kinetic product. The fragmented, P rich products and liberated monomers then recrystallize in a non-thermodynamic phase as their chemical potential at low temperature is very high. Templated by the initial phase of the MSC, the resulting NCs therefore adopt the unprecedented 3D polytwistane structure. The thermodynamic growth regime was also investigated using synchrotron in-situ SAXS and WAXS spectroscopies. These investigations corroborate growth pathways that involve cluster decomposition and regrowth as opposed to aggregation followed by annealing.

3.4 Experimental

3.4.1 General practices

Unless stated otherwise all chemical reactions were performed under N_2 using standard Schlenk line air-free techniques and glassware. Experiments were typically run using a 50 mL three-neck round bottomed flask equipped with a condensing column, gas adapter, glass thermowell, rubber septum, and magnetic stir bar. All glassware was oven or flame dried prior to use. Solvents were dried as described above. In a typical synthesis, materials were weighed and measured in a N_2 atmosphere glovebox and transferred to a receiving flask on the Schlenk line via syringe. Upon completing a reaction, solvent was removed by vacuum distillation and the flask was sealed and transferred into the glovebox for subsequent workup and analysis preparation. Samples were stored re-dispersed in toluene unless otherwise insoluble.

3.4.2 Experimental procedures, synthetic

3.4.2.1 Synthesis of Tristrimethylsilylsphosphine, $P(SiMe_3)_3$

$P(SiMe_3)_3$ was prepared in a modified literature procedure.[30,31] In our modified preparation NaK was substituted stoichiometrically with Na at a scale of 8.05 g (350 mmol) with the addition of 0.759g (6 mmol) naphthalene. All subsequent steps remained unaffected. Net yield, 60%.

3.4.2.2 Synthesis of the $In_{37}P_{20}$ MSC, $In_{37}P_{20}(OOCR)_{51}$

Myristate ligated (OOCR = $C_{14}H_{27}O_2^-$) InP MSC was prepared following literature procedures[17] using in situ produced $InMyr_3$ and $P(SiMe_3)_3$. The cluster was purified by flocculation between toluene and acetonitrile and stored dry under an inert atmosphere.

3.4.2.3 Synthesis of acid free In-Myristate

In-Myristate ($InMyr_3$) used outside of MSC synthesis was produced via $InMe_3$ (We have observed both various reaction sensitivities to acid and morphological differences between in-situ, $InAc_3$ derived $In(OOCR)_3$ vs that made with this method). In a typical synthesis 112 mg (0.70 mmol) of $InMe_3$ and 479 mg (2.10 mmol) of Myristic acid were each dissolved in 2 mL toluene respectively. The In solution was added dropwise to the acid solution with stirring at RT in a glovebox and the mixture was allowed to stir at RT for 2 hr. Finally, the solution was dried under vacuum and the material was stored as a solid under nitrogen.

3.4.2.4 QD Synthesis via MSC and $P(SiMe_3)_3$

In a typical synthesis 50 mg of MSC was dissolved in 5 mL dry toluene in the glovebox and transferred via syringe to charge a 3-neck round bottom flask equipped to the Schlenk line under N_2. Once the reaction was brought to temperature, 35-100 °C, a solution of 13.(3) uL $P(SiMe_3)_3$ (15 eq) in 1 mL toluene was rapidly injected and the solution was monitored by UV-vis examination of aliquots for 10-120 min until completion. Once complete the reaction was distilled to dryness using vacuum assisted distillation. The Product was resuspended in toluene and purified by repeated flocculation in toluene and acetonitrile (1:5).

3.4.2.5 $In_{37}P_{20}$ Kinetic Conversion to $In_{29}P_{14}$

In a glovebox 25 mg of purified MSC was dissolved in 25 mL dry toluene. A 3-neck round bottomed flask on the Schlenk line was charged with the MSC solution via syringe. To the solution 2 mL of a prepared stock solution containing a total 0.44 uL (1 equivalent) $P(SiMe_3)_3$ was injected at 0 °C. The temperature was raised and held at 25 °C under nitrogen flow for 120 hr using an oil bath. Aliquots taken were diluted in 2.0 mL dry toluene in air free cuvettes. Toluene was distilled under vacuum at 25 °C prior to NMR and other analyses.

3.4.2.6 ZnS Shelling

A batch of QDs was made using the above procedure with 35 mg MSC, 5 uL (8eq) $P(SiMe_3)_3$, and 4 mL dry ODE instead of toluene, carried out at 60 °C for 1 hr. The Sulphur precursor was made the day prior by allowing 10.5 mg elemental S (0.33 mmol) to stir at room temperature in 2 mL TOP overnight. The Zn precursor was made by first drying 75 mg Zinc Stearate (0.24 mmol) under dynamic and at 100 °C vacuum overnight. Under N_2 4 mL of dry ODE was added to the $ZnStr_2$ and was stirred at 200 °C for 2 hrs until the solution was mostly clear. Using a syringe approximately one third of the Zn solution was transferred to the QD flask and the temperature was raised to 200 °C. Upon reaching temperature one third of the TOP-S solution was injected over a 10 min period using a syringe pump. The reaction was allowed to proceed for another 10 min after which point the process was repeated two more times. The sample was resuspended in toluene, centrifuged, and decanted to remove greatly insoluble impurities, and was then purified by three rounds of resuspension in toluene and flocculation with acetonitrile. Photoluminescent data were acquired post purification.

3.4.3 Experimental procedures, analytical

3.4.3.1 In-situ UV-vis of QD Synthesis

In Situ observation of $P(SiMe_3)_3$ mediated QD growth was performed using an Ocean Optics dipprobe. The probe was fitted via air tight adapter to a 50 mL 4-neck round bottomed flask also equipped with condensing column, glass thermowell, and septa and under N_2 via the Schlenk line. The flask was charged with 25 mg MSC dissolved in 15 mL dry toluene. The temperature was raised to 100 °C at which point 3 mL of dry toluene containing 10 uL (23 equivalents) $P(SiMe_3)_3$ was slowly injected over 1 hr using a syringe pump.

3.4.3.2 UV-Vis Spectrometry

Ex situ UV-Vis analysis was measured using a Varian Cary model 6000 dual beam spectrometer. The spectrometer was equipped with a Mercury light source and measurements were made with 1 nm resolution between 300 and 800 nm. Diluted samples were loaded into polished quartz cuvettes for analysis. Purified samples were taken directly from the glovebox using air-tight cuvettes.

3.4.3.3 Photoluminescence Spectrometry

Photoluminescence spectra of the ZnS shelled particles were acquired on a Horiba Fluoromax 4 spectrofluorimeter. The sample was diluted in toluene, loaded in a quartz cuvette, and excited at $\lambda = 430$ nm. Light acquisition was measured using emission and collection slit widths of 2nm and automated software correction of dark noise.

3.4.3.4 XRD Preparation and Analysis

After being purified, samples of clusters and quantum dots were concentrated in toluene. On <100> Si wafer and in the glovebox the samples were dropcast and the solvent was allowed to evaporate. This was repeated for 3-10 repetitions until visible surface coverage was achieved. Samples were analyzed on a Bruker D8 Discover X-Ray diffractometer with Cu Kα source. The Instrument was equipped with a 0.5 mm beam collimator, large area 2D detector, and an air scatter screen. Data were acquired with fixed theta position.

3.4.3.5 HRTEM Preparation and Analysis

Prior to TEM analysis samples were passed through a column filled with toluene soaked BioBeads 1-2 times as an additional purification from excess carboxylate. Samples were diluted in dry toluene and dropcast on 200 mesh carbon-covered Cu TEM grids supplied by TED Pella. HRTEM imaging was performed using an FEI TECNAI F20 operating at 200 KeV using a single tilt holder with a point resolution of 2.3 Å. Images were collected via 4 MP CCD camera.

3.4.3.6 Solution ^{31}P and ^{1}H NMR Spectroscopy

Solution ^{31}P NMR was performed on a Bruker Avance 500 system operating with a Bruker BBI ^{1}H {X} multichannel probe operating at 202 MHz. Unless otherwise stated ^{31}P Spectra were taken under N_2 in J Young tubes and using C_6D_6 as solvent. Chemical shifts are referenced to external 85% phosphoric acid. Acquisitions were made using a d1 delay of 40s and generally collected for 8-12 hours.

Solution ^{1}H spectra were taken either on the Bruker Avance 500 or on a Bruker Avance 300 system also operating with a Bruker BBI ^{1}H {X} multinuclear probe operating at 300 MHz. Samples were prepared in and referenced to C_6D_6. Acquisitions were made with a d1 delay of 25 s unless otherwise stated.

3.4.3.7 Solid State MAS ^{31}P NMR

For MAS analysis ca. 100 mg of QDs were prepared and purified using the procedure outlined above. The sample was pumped to dryness using dynamic vacuum yielding a waxy product. Boron Nitride was manually mixed into this product until a homogenous, free-flowing powder was formed. Samples were packed firmly into a 3.2 mm ZrO_2 rotor. Solid state spectra were taken on a Bruker 700 Avance system equipped with a 3.2 mm probe at 283 MHz. Spectra were acquired at the magic angle with a spin rate of 10 kHz and referenced to 85% phosphoric acid.

3.4.3.8 Diffusion Spectroscopy NMR

Diffusion constants were measured in C_6D_6 using a pulse field gradient stimulated Hahn echo sequence. Spectra were acquired on a Bruker Avance 500 (500 MHz). The sequence was executed with a sine wave pulse gradient and with a delay Δ between 100 and 200 ms for molecular or cluster species respectively. Data was processed using DOSY Toolbox freeware[32].

3.4.3.9 Synchrotron SAXS Preparation and Analysis

Small angle X-ray scattering (SAXS) was performed using beamline 1-5 of the Stanford Synchrotron Radiation Light Source at the SLAC National Laboratory. Wide angle X-ray scattering (WAXS) was collected at beamline 11-2. Data were acquired using a 1 m detector distance configuration using a PILATUS 100K 2D detector and at 10.5 keV. Samples were prepared in 1 mm quartz capillaries produced by Charles Supper Co at concentrations of about 10 mg/mL and sealed with epoxy. SAXS data were analyzed using SasView, an open source project developed in part by the NSF and NIST.[33] The background was determined using an external capillary of solvent as a baseline reference and data were normalized to the beam-stop intensity.

3.5 References

(1) *Metal Clusters in Chemistry*; Oro, L. A., Braunstein, P., Raithby, P. R., Eds.; Wiley-VCH: Weinheim ; New York, 1999.

(2) Schnöckel, H. Structures and Properties of Metalloid Al and Ga Clusters Open Our Eyes to the Diversity and Complexity of Fundamental Chemical and Physical Processes during Formation and Dissolution of Metals †. *Chem. Rev.* **2010**, *110* (7), 4125–4163. https://doi.org/10.1021/cr900375g.

(3) Schnepf, A.; Jee, B.; Schnöckel, H.; Weckert, E.; Meents, A.; Lübbert, D.; Herrling, E.; Pilawa, B. Preparation and Precise Structural Determination of a Second Ga_{84} Cluster Compound. A First Hint for Cluster Doping and Its Fundamental Consequences in the Field of Chemistry and Physics of Nanoscaled Metalloid Cluster Material. *Inorg. Chem.* **2003**, *42* (24), 7731–7733. https://doi.org/10.1021/ic035031k.

(4) Richards, A. F.; Hope, H.; Power, P. P. Synthesis and Characterization of Neutral, Homo and Heteronuclear Clusters with Unsubstituted Germanium or Tin Atoms. *Angew. Chem. Int. Ed.* **2003**, *42* (34), 4071–4074. https://doi.org/10.1002/anie.200351907.

(5) Higaki, T.; Liu, C.; Zhou, M.; Luo, T.-Y.; Rosi, N. L.; Jin, R. Tailoring the Structure of 58-Electron Gold Nanoclusters: $Au_{103}S_2(S\text{-}Nap)_{41}$ and Its Implications. *J. Am. Chem. Soc.* **2017**, *139* (29), 9994–10001. https://doi.org/10.1021/jacs.7b04678.

(6) Vossmeyer, T.; Reck, G.; Katsikas, L.; Haupt, E. T. K.; Schulz, B.; Weller, H. A “Double-Diamond Superlattice” Built Up of $Cd_{17}S_4(SCH_2CH_2OH)_{26}$ Clusters. *Science* **1995**, *267* (5203), 1476–1479.

(7) Wang, F.; Wang, Y.; Liu, Y.-H.; Morrison, P. J.; Loomis, R. A.; Buhro, W. E. Two-Dimensional Semiconductor Nanocrystals: Properties, Templated Formation, and Magic-Size Nanocluster Intermediates. *Acc. Chem. Res.* **2015**, *48* (1), 13–21. https://doi.org/10.1021/ar500286j.

(8) Feng, P.; Bu, X.; Zheng, N. The Interface Chemistry between Chalcogenide Clusters and Open Framework Chalcogenides. *Acc. Chem. Res.* **2005**, *38* (4), 293–303. https://doi.org/10.1021/ar0401754.

(9) Zhang, J.; Rowland, C.; Liu, Y.; Xiong, H.; Kwon, S.; Shevchenko, E.; Schaller, R. D.; Prakapenka, V. B.; Tkachev, S.; Rajh, T. Evolution of Self-Assembled ZnTe Magic-Sized Nanoclusters. *J. Am. Chem. Soc.* **2015**, *137* (2), 742–749. https://doi.org/10.1021/ja509782n.

(10) Gary, D. C.; Flowers, S. E.; Kaminsky, W.; Petrone, A.; Li, X.; Cossairt, B. M. Single-Crystal and Electronic Structure of a 1.3 Nm Indium Phosphide Nanocluster. *J. Am. Chem. Soc.* **2016**, *138* (5), 1510–1513. https://doi.org/10.1021/jacs.5b13214.

(11) Zhu, T.; Zhang, B.; Zhang, J.; Lu, J.; Fan, H.; Rowell, N.; Ripmeester, J. A.; Han, S.; Yu, K. Two-Step Nucleation of CdS Magic-Size Nanocluster MSC–311. *Chem. Mater.* **2017**, *29* (13), 5727–5735. https://doi.org/10.1021/acs.chemmater.7b02014.

(12) Kudera, S.; Zanella, M.; Giannini, C.; Rizzo, A.; Li, Y.; Gigli, G.; Cingolani, R.; Ciccarella, G.; Spahl, W.; Parak, W. J.; Manna, L. Sequential Growth of Magic-Size CdSe Nanocrystals. *Adv. Mater.* **2007**, *19* (4), 548–552. https://doi.org/10.1002/adma.200601015.

(13) Wang, Y.; Zhang, Y.; Wang, F.; Giblin, D. E.; Hoy, J.; Rohrs, H. W.; Loomis, R. A.; Buhro, W. E. The Magic-Size Nanocluster (CdSe) $_{34}$ as a Low-Temperature Nucleant for Cadmium Selenide Nanocrystals; Room-Temperature Growth of Crystalline Quantum Platelets. *Chem. Mater.* **2014**, *26* (7), 2233–2243. https://doi.org/10.1021/cm404068e.

(14) Olbrich, M.; Mayer, P.; Trauner, D. Synthetic Studies toward Polytwistane Hydrocarbon Nanorods. *J. Org. Chem.* **2015**, *80* (4), 2042–2055. https://doi.org/10.1021/jo502618g.

(15) Barua, S. R.; Quanz, H.; Olbrich, M.; Schreiner, P. R.; Trauner, D.; Allen, W. D. Polytwistane. *Chem. - Eur. J.* **2014**, *20* (6), 1638–1645. https://doi.org/10.1002/chem.201303081.

(16) Stier, O.; Grundmann, M.; Bimberg, D. Electronic and Optical Properties of Strained Quantum Dots. *Phys. Rev. B* **1999**, *59* (8), 5688.

(17) Gary, D. C.; Terban, M. W.; Billinge, S. J. L.; Cossairt, B. M. Two-Step Nucleation and Growth of InP Quantum Dots via Magic-Sized Cluster Intermediates. *Chem. Mater.* **2015**, *27* (4), 1432–1441. https://doi.org/10.1021/acs.chemmater.5b00286.

(18) Yang, J.; Muckel, F.; Baek, W.; Fainblat, R.; Chang, H.; Bacher, G.; Hyeon, T. Chemical Synthesis, Doping, and Transformation of Magic-Sized Semiconductor Alloy Nanoclusters. *J. Am. Chem. Soc.* **2017**, *139* (19), 6761–6770. https://doi.org/10.1021/jacs.7b02953.

(19) Tiemann, M.; Weiß, Ö.; Hartikainen, J.; Marlow, F.; Lindén, M. Early Stages of ZnS Nanoparticle Growth Studied by In-Situ Stopped-Flow UV Absorption Spectroscopy. *ChemPhysChem* **2005**, *6* (10), 2113–2119. https://doi.org/10.1002/cphc.200500163.

(20) Lee, J.; Yang, J.; Kwon, S. G.; Hyeon, T. Nonclassical Nucleation and Growth of Inorganic Nanoparticles. *Nat. Rev. Mater.* **2016**, 16034. https://doi.org/10.1038/natrevmats.2016.34.

(21) Jiang, Z.-J.; Kelley, D. F. Role of Magic-Sized Clusters in the Synthesis of CdSe Nanorods. *ACS Nano* **2010**, *4*, 1561–1572.

(22) Friedfeld, M. R.; Stein, J. L.; Cossairt, B. M. Main-Group-Semiconductor Cluster Molecules as Synthetic Intermediates to Nanostructures. *Inorg. Chem.* **2017**, *56* (15), 8689–8697. https://doi.org/10.1021/acs.inorgchem.7b00291.

(23) La Porta, F. A.; Andrés, J.; Li, M. S.; Sambrano, J. R.; Varela, J. A.; Longo, E. Zinc Blende versus Wurtzite ZnS Nanoparticles: Control of the Phase and Optical Properties by Tetrabutylammonium Hydroxide. *Phys Chem Chem Phys* **2014**, *16* (37), 20127–20137. https://doi.org/10.1039/C4CP02611J.

(24) Mićić, O.; Ahrenkiel, S.; Nozik, A. Synthesis of Extremely Small InP Quantum Dots and Electronic Coupling in Their Disordered Solid Films. *Appl. Phys. Lett.* **2001**, *78* (25), 4022–4024. https://doi.org/10.1063/1.1379990.

(25) Cho, E.; Jang, H.; Lee, J.; Jang, E. Modeling on the Size Dependent Properties of InP Quantum Dots: A Hybrid Functional Study. *Nanotechnology* **2013**, *24* (21), 215201-1–5.

(26) Virieux, H.; Le Troedec, M.; Cros-Gagneux, A.; Ojo, W.-S.; Delpech, F.; Nayral, C.; Martinez, H.; Chaudret, B. InP/ZnS Nanocrystals: Coupling NMR and XPS for Fine Surface and Interface Description. *J. Am. Chem. Soc.* **2012**, *134* (48), 19701–19708. https://doi.org/10.1021/ja307124m.

(27) Owen, J. The Coordination Chemistry of Nanocrystal Surfaces. *Science* **2015**, *347* (6222), 615–616. https://doi.org/10.1126/science.1259924.

(28) Markov, I. V. *Crystal Growth for Beginners: Fundamentals of Nucleation, Crystal Growth and Epitaxy*, 2nd ed.; World Scientific: Singapore; River Edge, N.J, 2003.

(29) Mujica, A.; Needs, R. Theoretical Study of the High-Pressure Phase Stability of GaP, InP, and InAs. *Phys. Rev. B* **1997**, *55* (15), 9659.

(30) Becker, G.; Schmidt, H.; Uhl, G.; Uhl, W.; Regitz, M.; Roesch, W.; VogelBacher, U. Tris(Trimethylsilyl)Phosphine. In *Inorganic Syntheses*; John Wiley & Sons, Inc.: New York, 2007; Vol. 27, pp 243–249.

(31) Kosolapoff, G. M. Isomerization of Alkylphosphites. III. The Synthesis of n-Alkylphosphonic Acids. *J. Am. Chem. Soc.* **1945**, *67* (7), 1180–1182.

(32) Nilsson, M. The DOSY Toolbox: A New Tool for Processing PFG NMR Diffusion Data. *J. Magn. Reson.* **2009**, *200* (2), 296–302. https://doi.org/10.1016/j.jmr.2009.07.022.

(33) SasView. SasView https://sasview.github.io/ (accessed Mar 13, 2020).

Chapter 4. Covalently Linked, Two-Dimensional Quantum Dot Assemblies

4.1 Introduction

A longstanding goal in materials synthesis is the formation of order across length scales by the directed assembly of nanoscopic building blocks.[1–4] By creating long range, hierarchical materials with order engineered down to the nanometer length scale, a new environment is created for the nanoscale building blocks, which can lead to distinct local behavior.[5–7] Moreover, new system-level properties may emerge, a feature commonly exploited in nature to create complex functionality.[8] Many successful strategies have been developed to create nanoparticle frameworks with long-range order, usually based on the use of hard- or soft-matter templates,[9–11] or alternatively crystallization or aggregation across a larger length scale.[12–14] The crystallization of atoms and small molecules is a well understood and analogous process to the repeated assembly of monodisperse nanoparticles or protein-sized molecules. In the most straightforward cases the direct, non-covalent crystallization of superlattices has been observed using nanoparticles as superatoms in crystalline or mesocrystalline lattices and films.[9,15,16] A more generalizable approach to nanoparticle assembly has been the addition of linker units that make use of either non-covalent or covalent bonding to hold or direct individual centers in a lattice,[17–20] similar to the strategy common to metal- and covalent-organic frameworks (MOFs and COFs).[21,22] However, few generalizable strategies exist when the assembling unit exceeds the size of a small molecule.

Forming freestanding assemblies of nanoparticles with a high degree of order has proven to be a particular challenge, and most solution synthesized NP assemblies in the literature are entirely amorphous.[17,23] This is due to their large size and polydispersity resulting in crystallization of a superstructure being kinetically disfavored. In contrast, more ordered and mesocrystalline nanoparticle assemblies are the result of enthalpic or electrostatic assembly pathways, templating, and often drying effects via dipolar and Van der Waals interactions.[24,25] Particles with well-defined shapes for example can exhibit permanent dipoles leading to solution-phase self-assembly as has been seen in the dipole driven formation of anisotropic CdTe films in water with charged ligands.[26] Similarly, nano and microparticles with well defined, distinguished facets and anisotropy have been observed to form long range assemblies,[13,27,28] and especially in the presence of hard templates,[29,30] bio-templates,[31–33] or interfaces in which they preferentially orient.[34–36]

Thermodynamic assembly forces have been demonstrated most clearly in the case of nanoparticle "programmable atom equivalent" design. In these systems it has been shown that DNA based ligands induce assembly driven by the enthalpic, thermodynamically favored binding of complementary base pairs leading to orientational control.[31,37–41] Recently, this strategy was exploited to create 3D frameworks of DNA-defined voxels that define the lattice symmetry independent of the size or shape of the nanoparticles.[42] Extension of this approach to more versatile polymer-based ligands with "lock-and-key" complementarity has also been realized.[43–48] These methods, however, often require ligands that are difficult to scale and have been most broadly examined in the case of traditional metal nanoparticles in aqueous solution. Very few examples exist in the literature of scalable, solution processable methods for creating ordered assemblies for arbitrary nanoparticle compositions. Scalable and generalizable syntheses with robust products are required for practical applications such as catalysis where changes to material composition and morphology are less flexible. In one particularly inspiring example, Pozzo demonstrated a solution phase method of directed nanoparticle assembly based on generalizable steric exclusion,[49] allowing formation of dimers, trimers, and higher-order linear oligomers starting from spherical nanoparticles. This interaction of "patchy" surfaces for hierarchical self-assembly has been widely examined theoretically,[50,51] but few experimental results exist in this area, especially in the case of isotropic, 0-dimensional nanoparticles in the 1-10 nm size regime. Here we demonstrate the generalizable assembly of colloidal semiconductor quantum dots into robust, covalently linked monolayer and multilayer two-dimensional sheets. Our method relies on the exchange of a moderate density of bifunctional linkers (10-50 equivalents per QD) on an otherwise fatty-acid-ligated surface. We demonstrate the generality of the method using CdSe (3.3 nm), InP/ZnSeS (3.2 nm), and CdS (5.9 nm) QDs. The impacts of equilibration time, QD concentration, linker concentration, and linker identity (length and rigidity) are explored in detail to give a set of design principles that deepen our understanding of the assembly process.

4.2 Results and Discussion

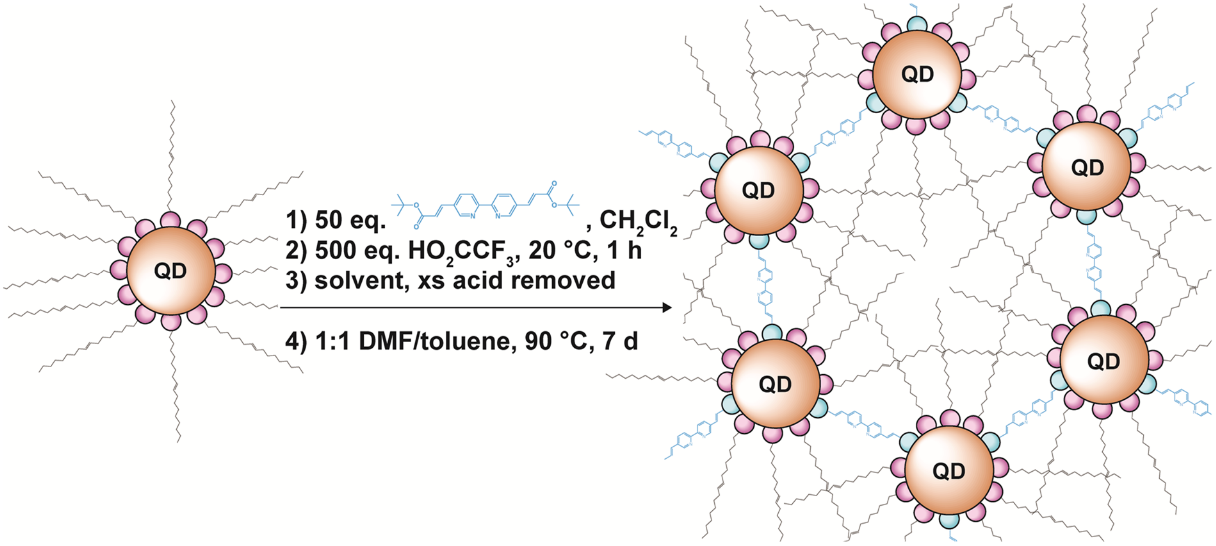

Scheme 4.1. Synthesis of 2D QD assemblies from QDs and esterified linker

4.2.1 Synthesis of amorphous and 2D Quantum Dot Assemblies

The synthesis of monolayer quantum dot sheets is typified by the reaction of 5.9 nm oleate-capped CdS quantum dots and 2,2'-bipyridine-5,5'-diacrylic acid (Scheme 4.1). A 2 μM solution of quantum dots and 50 eq. of crosslinker were combined in CH_2Cl_2 at room temperature in a nitrogen atmosphere glovebox. The crosslinker was added in its esterified (^{t}Bu) form to improve its solubility in non-polar solvents and thereby ensure good mixing prior to aggregation. Notably, the carboxylic acid form of the linker is both poorly soluble and apt to immediately induce aggregation, visible by precipitation of the quantum dots. In a second step, aggregation was induced by addition of stoichiometric amounts of trifluoroacetic acid to deprotect the ester, followed by 1 h equilibration at room temperature. Excess trifluoroacetic acid and the solvent were removed under reduced pressure. At this stage, amorphous quantum dot aggregates with sizes dictated by the total amount of added linker (10-250 eq) are obtained as determined by TEM and dynamic light scattering (DLS) analysis (Figure 4.1).

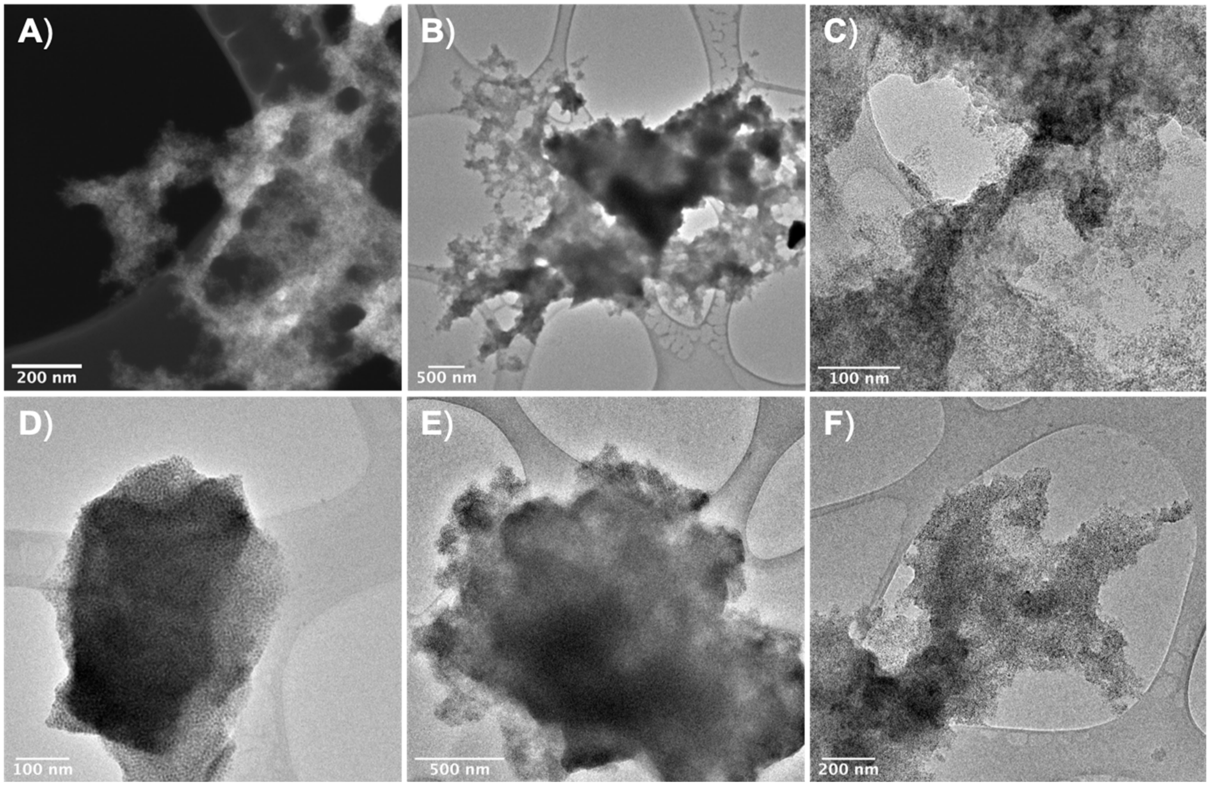

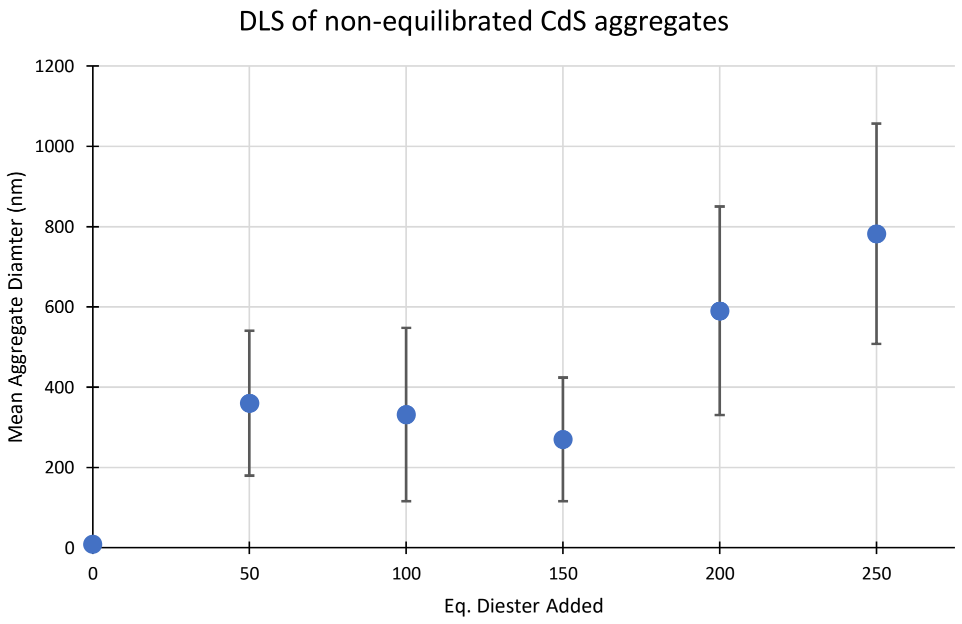

Figure 4.1. TEM images of amorphous QD aggregates after 1 h equilibration at 22 °C with varied linker equivalents 10 eq, 50 eq, and 250 eq (A-C respectively) and corresponding DLS. TEM images using 50 eq linker after 1, 4, and 7 d at 90 °C (D-F, respectively).

This process is general for various quantum dot compositions and sizes, including 3.3 nm CdSe, 5.9 nm CdS, and 3.2 nm InP/ZnSeS. By tuning the solution concentration and equivalents of linkers, aggregates of mean radius 100 to 800 nm can be targeted using this in-situ deprotection method, as measured by DLS. Similar but more polydisperse assemblies were created when using various bis-carboxylic acid cross linkers such as dodecanedioic acid and using 2,2'-bipyridine-5,5'-diacrylic acid directly without in situ deprotection of the ester. Similar schemes have been reported previously in the literature for aggregation of nanoparticles using bifunctional linkers and have achieved amorphous assemblies and monoliths of NPs using ambient, solvothermal, or supercritical reaction conditions.

While a single carboxylate linkage may be considered labile, a large crosslinked system is effectively a kinetically trapped structure. The method described here aims to target a more specific free energy minimum in the assembly landscape. Quantum dot monolayer sheets were prepared by drying and resuspending the amorphous assemblies in a 50/50 mixture of toluene and DMF at a 2 mM nanoparticle concentration (6 mL scale typical). The solutions were raised to 90 °C under N_2 and with 60 rpm stirring. This mixture of solvents was found to maximally solubilize both the quantum dots and 2,2'-Bipyridine-5,5'-diacrylic acid, allowing for improved equilibration kinetics. The solution was held at 90 °C for between one and seven days. Observations were made by TEM and DLS of aliquots that were removed and purified by flocculation at several time points. After one day of equilibration at 90 °C, the large amorphous aggregates had broken down into a polydisperse ensemble of smaller aggregates. Over the next four to seven days, a secondary morphological evolution occurred resulting in the formation of two-dimensional structures (Figure 4.2, Figure 4.3).

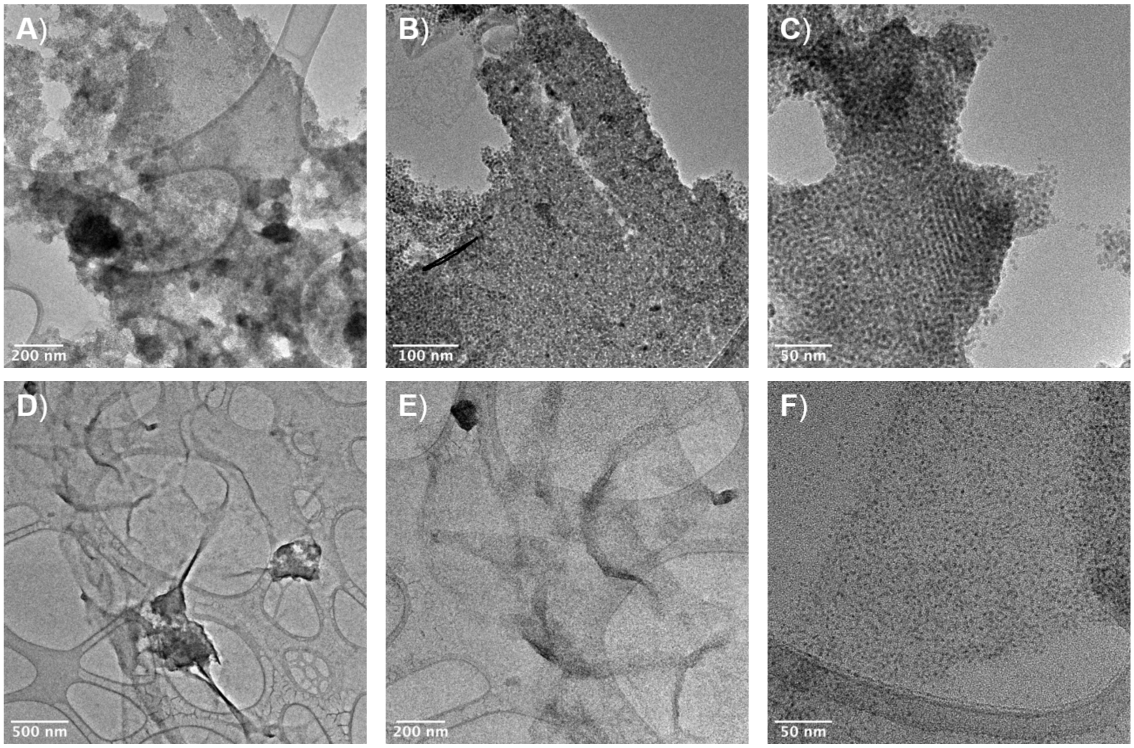

Figure 4.2. Two dimensional aggregates of 5.9 nm CdS QDs following treatment with 50 eq. 2,2'-bipyridine-5,5'-diacrylic acid and equilibration at 90 °C for 7 days.

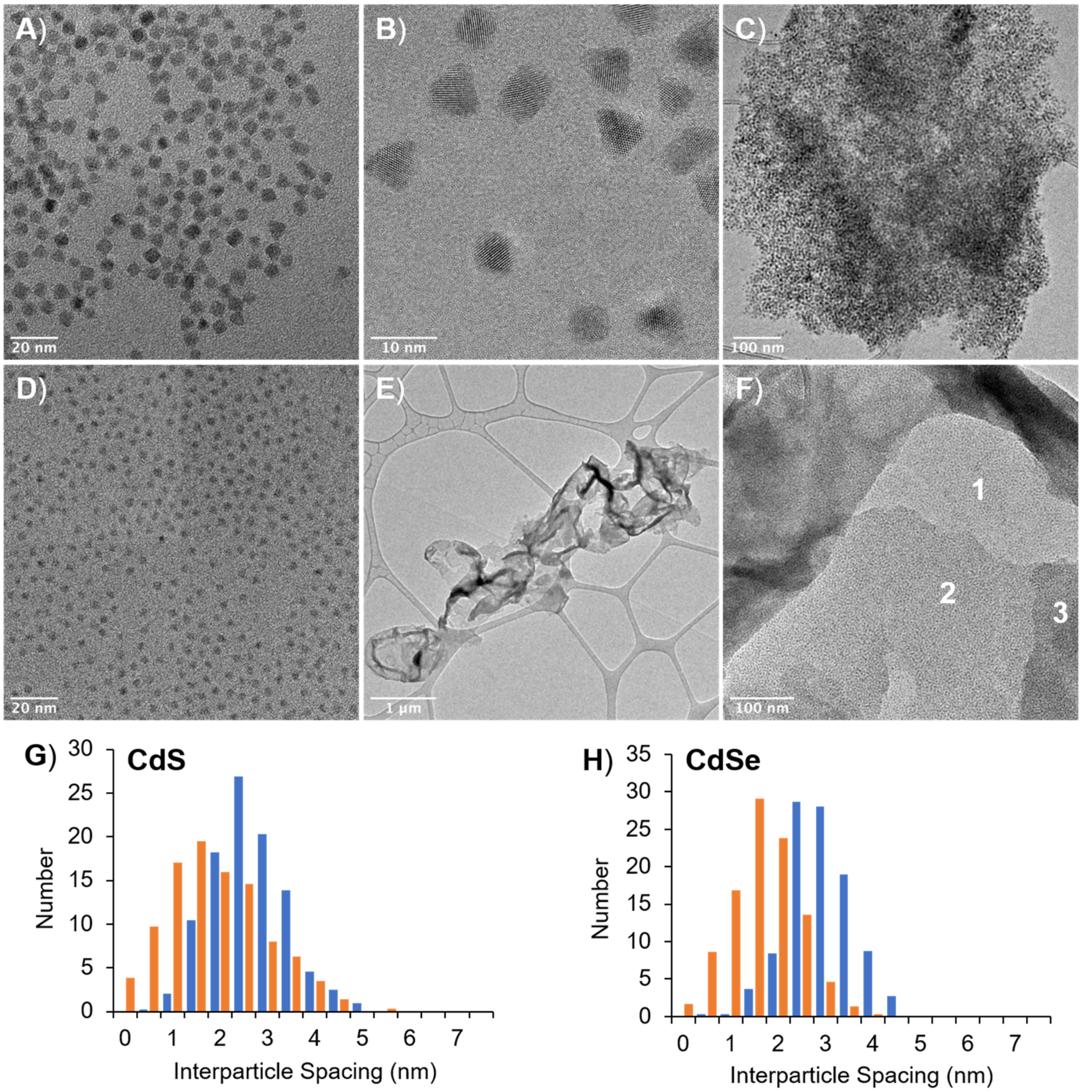

Figure 4.3. (A, B) 5.9 nm CdS and (D) 3.3 nm CdSe QDs. Assembly of (C) 5.9 nm CdS and (E, F) 3.3 nm CdSe QDs formed following treatment with 2,2'-bipyridine-5,5'-diacrylic acid and equilibration at 90 °C for 7 days. Areas of high contrast result from sheets folding during drying, but areas where a slight increase of contrast is seen in a stepwise fashion indicates sheet stacking into bilayers and trilayers as illustrated in F. (G – CdS, H – CdSe) Histograms of interparticle spacing for close packed arrays of free QDs (blue) and linked QDs (orange).

4.2.2 HR TEM Analyses of 2D Quantum Dot Assemblies

With *ex situ* TEM analysis, the assembly process can be seen to ultimately create large, nearly flat QD aggregates on the micron scale that resemble sheets (Figure 4.3C, E, F). The thickness appears to be roughly that of a monolayer of QDs without structure or ordering within the plane of the layer. Sporadic areas within the sheets show some QD overlap (Figure 4.3C), likely due to QDs bound outside the plane of the main monolayer. Additionally, multilayer areas are observed due to the drying of the sheets for TEM analysis leading to stacking or folding of the sheets (Figure 4.3E, F). With no linker present, oleate-capped CdS QDs are seen to dry in roughly hexagonal close packed (hcp) arrays with an average size of 5.92 ± 0.65 nm and center-to-center distance of 7.88 ± 0.96 nm, leaving a 1.95± 0.96 nm spacing between the particles (Figure 4.3A, E, F and Table 4.1).

Table 4.1. Particle size and spacing analysis for CdS QDs from TEM.

CdS	Particle size (nm)	Center-center distance (nm)	Interparticle spacing (nm)	STDEV (nm)
QDs	5.93	7.88	1.96	0.96
Aggregates	5.31	7.07	1.76	1.14

Note the reported ranges here reflect the dispersity of the sample and not the error of the measurement. Before undergoing aggregation, the CdS QDs exhibit a faceted pyramidal structure that can disrupt the hexagonal packing depending on how the nanocrystals dry relative to neighboring particles. After being subjected to assembly conditions the nanocrystals etched slightly, resulting in smaller, more spherical particles that packed more uniformly into hexagonal arrays. The final particles exhibit an average size of 5.31 ± 0.67 nm after 7 days in the reaction mixture. In the case of etching without assembly (using a monofunctional linker, for example), the average particle spacing increases to 2.63 ± 0.79 nm because of the morphological evolution to a less faceted shape that forms more ordered hexagonal lattices. In the case of successful assembly, the center-to-center distance decreases as a result of the shorter bifunctional linker with an average center-to-center distance of 7.07 ± 1.14 nm, leaving 1.76 ± 1.14 nm between particles. The linker is 1.63 nm long from oxygen to oxygen as determined by single crystal X-ray diffraction analysis, slightly shorter than the native oleate ligands (~2 nm), on the surface of the particles. For two particles to become linked, the linker must penetrate two individual ligand shells, each of about 2 nm. There is likely interweaving occurring in the ligand shells, especially upon drying, as we observe an average particle spacing of 2.63 nm without linker present.

4.2.3 Synchrotron SAXS Analyses of QD Assemblies

The structures of the QD assemblies were analyzed by solution phase SAXS using the synchrotron source at the Stanford National Accelerator Labs. Suspensions of QD sheets in toluene were measured in sealed capillaries to confirm the existence and structure of assemblies in solution (Figure 4.4).

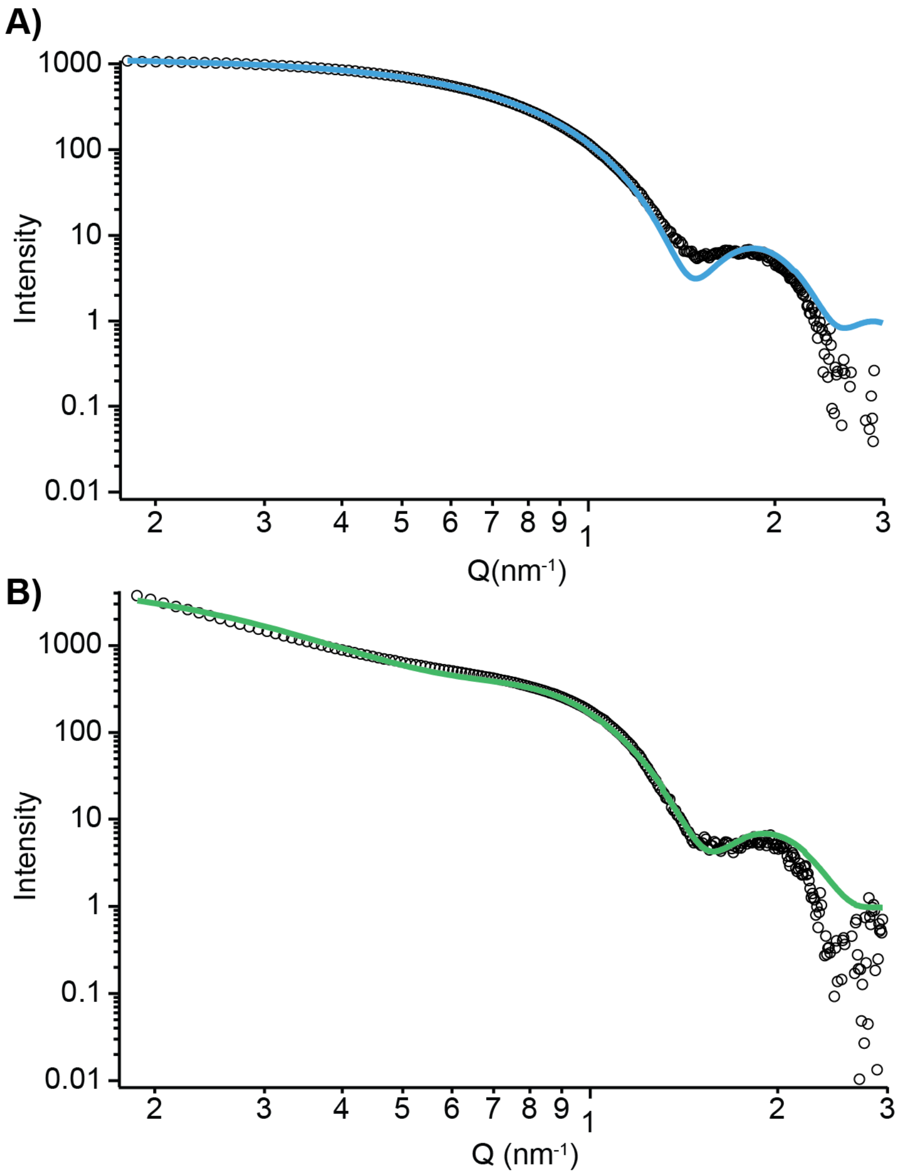

Figure 4.4. SAXS data (black) for 6 nm CdS QDs in toluene (A) and 2D assemblies of CdS QDs in toluene (B). The data in (A) are fit to a spherical model giving a diameter of 5.96 ± 0.55 (blue). The data in (B) are fit to a "pearl necklace" model giving a particle radius of 5.62 ± 0.62 and an interparticle distance of 1.84 nm.

Table 4.2. Results of SAXS fitting of free QDs and QD assemblies. Fitting methodology described in section 4.4.12.

	QD SAXS	QD TEM	Assembly SAXS	Assembly TEM
Diameter (nm)	5.96 ± 0.55	5.93 ± 0.65	5.62 ± 0.62	5.31 ± 0.67
Spacing (nm)	n/a	1.96 ± 0.96	1.84	1.76 ± 1.14

The unassembled CdS QDs were fit to a spherical model to a diameter of 5.96 ± 0.55 nm, in strong agreement with manual TEM measurement of 5.92 ± 0.65 nm (Table 4.2). SAXS measurements of QD sheet assemblies were fit using an existing 'pearl necklace' model fitting both the spherical diameter and spacing of particles within the assembly.[52,53] The results of this fitting give a particle diameter of 5.62 ± 0.62 nm and an interparticle spacing of 1.84 nm Table 4.2), in close agreement with both crystallographic data of the linker length and TEM measurements. By dividing the aggregate scattering intensity by the as-measured form factor, an experimental structure factor can be obtained in addition to the theoretical pearl necklace model.[54–57] This experimental structure factor displays clear aggregation of particles at low Q values as well as a defined correlation peak at 0.95 nm^{-1} near the expected mean center-to-center distance. These data along with other solution phase measurements including DLS (Table 4.3) show definitively the existence of assemblies in solution and not merely as a drying effect. Interestingly, the optical properties of the sheets measured by diffuse reflectance confirms the QDs remain intact and that their electronic structure is largely unperturbed by the assembly process in the CdS case (Figure 4.5).

Table 4.3. Particle size and spacing analysis for different linkers measured by TEM.

	Center-center distance (nm)	**Interparticle spacing (nm)**	**Theoretical Spacing (crystallographic estimates from CCDC)**
2,2′-bipyridine-4,4′-dicarboxylic acid	7.60	2.28 ± 0.89	1.07
Terephthalic acid	7.48	2.17 ± 0.83	0.73
Dodecanedioic acid	6.88	1.57 ± 0.80	1.61 *est
2,2′-biphenyl-5,5′-diacrylic acid	7.01	1.70 ± 0.83	1.68

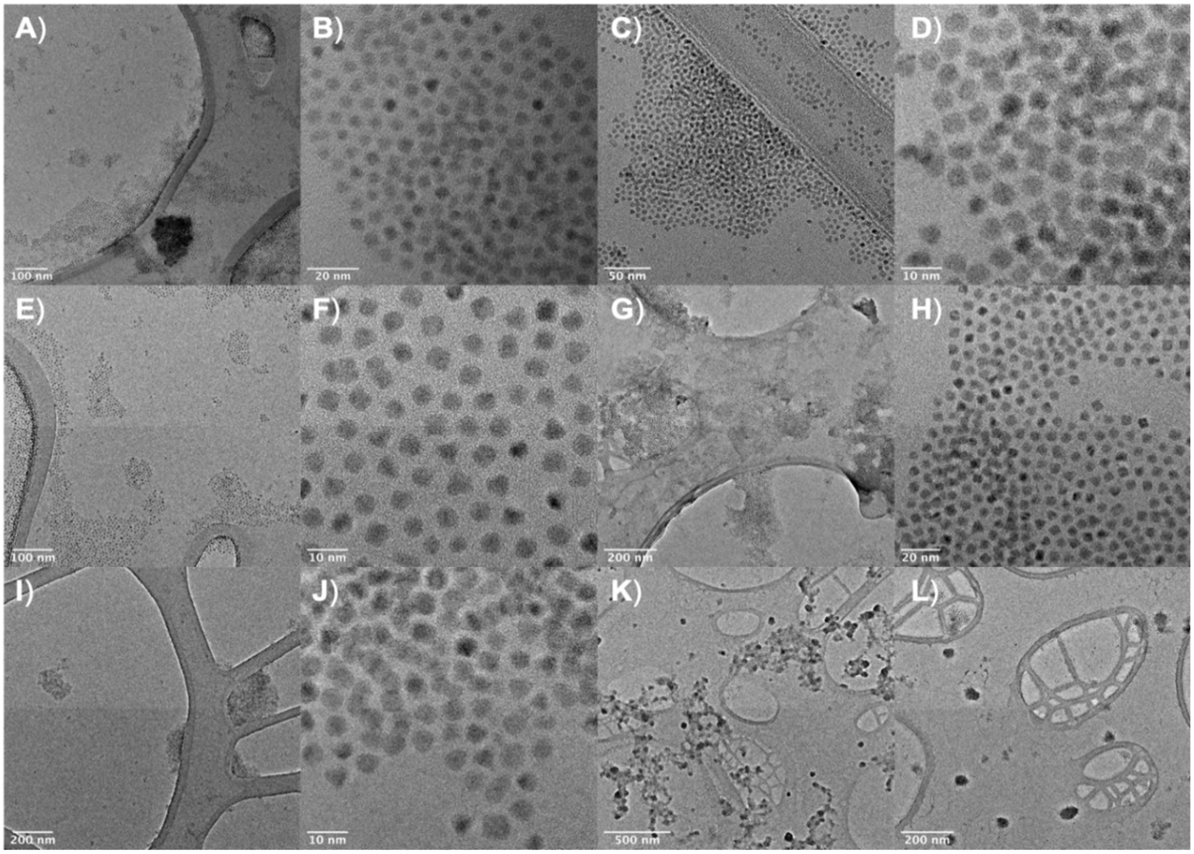

Figure 4.5. TEM images of particles following treatment of CdS QDs with different linkers. (A, B) 2,2′-bipyridine-4,4′-dicarboxylic acid. (C, D) 2,2′-biphenyl-5,5′-diacrylic acid. (E-H) terephthalic acid. (I-L) dodecanedioic acid.

4.2.4 Investigation of the Mechanism of 2D Structure Assembly

We hypothesize that the length of the bifunctional linker being very similar to the native ligands is critical in forming these anisotropic sheets from 0-dimensional particles. In fact, the combination of short bifunctional linkers (e.g., mercaptopropionic acid and ethanedithiol) and quantum dots is a common approach to create close packed QD films with strong electronic communication for device applications,[58–62] yet freestanding two-dimensional assemblies have not before been observed. In these cases, ligand shell steric hinderance is demonstrably too extreme to achieve crosslinking given the extremely short bifunctional ligands. Conversely linker molecules more than twice the native ligand length would provide no barrier at all towards random, isotropic assembly.

To test this hypothesis, aggregation was performed under standard conditions with terephthalic acid and 2,2′-bipyridine-4,4′-dicarboxylic acid, rigid bifunctional linkers, estimated to be 7 Å and 11 Å spacers by crystallographic measurement, which are approximately half the length of our standard linker. In both cases, well-defined QD sheets were not observed (Figure 4.5 A, B, E, H). The only observed aggregation occurred with a yield of <5% by volume and, in the case of 2,2′-bipyridine-4,4′-dicarboxylic, led to small, amorphous aggregates as observed by TEM (Figure 4.5 A, B) and DLS. The majority of the QDs dried in an hcp array, with better uniformity than native CdS QDs, and with a similar particle spacing of 2.0 nm (Table 4.3). Based on the above results, we conclude that, if the linker is not long enough, it cannot successfully bridge two ligand shells and lead to sheet formation.

To test the importance of linker rigidity, assembly was performed with dodecanedioic acid, a saturated bifunctional linker of comparable length to 2,2'-bipyridine-5,5'-diacrylic acid (~1.69 nm vs 1.63 nm). For the flexible linker, high quality sheets very similar to standard conditions were observed with an average spacing of 1.57 ± 0.83 nm (Figure 4.5 I-L). For all three of the above linkers tested, unlike the standard 2,2'-bipyridine-5,5'-diacrylic acid linker, only a fraction of the material crashed out during assembly. Analysis of the supernatants showed unlinked QDs in the case of 2,2′-bipyridine-4,4′-dicarboxylic, a few small sheet-like structures in the case of terephthalic acid, and abundant spherical aggregates for the dodecanedioic acid (Figure 4.5 A, B, E, H). Finally, aggregation was performed using 2,2'-biphenyl-5,5'-diacrylic acid to confirm the bipyridine binding pocket was not influencing sheet formation. As expected, two-dimensional sheets were observed analogous to standard linkage with an average particle spacing of 1.70 ± 0.83 nm (Figure 4.5 C, D). Based on these results, we conclude the linker must be long enough to efficiently penetrate the ligand shell of two particles, and it is likely that linker rigidity aids in preventing more 3D growth as seen with dodecanedioic acid.

To test the generalizability of the aggregation, sheets were made with InP/ZnSe (3.2 nm InP cores) and CdSe (3.3 nm) in addition to the standard CdS (5.9 nm) cores. In all cases, well defined sheets formed independent of particle size and composition with some particle etching seen throughout all samples. The average distance between particles in the sheets remained roughly the same between the different cores at 1.58 ± 0.83 nm and 1.63 ± 0.73 nm for InP/ZnSe and CdSe, respectively. In the case of InP/ZnSe, an aliquot after 1 day of assembly showed two populations of particles, from a previously monodisperse sample. The two sizes of cores (6 nm, shelled and 3 nm, unshelled) were seen to size-segregate, making two distinct sheet populations containing only one size of particle within a given sheet. By the 4-day and 7-day aliquots, the shelled population had completely destabilized leaving only sheets with 3 nm InP cores. Similar size-segregation was observed when assembly was performed using CdS QDs containing a bimodal distribution of particle sizes (Figure 4.6).

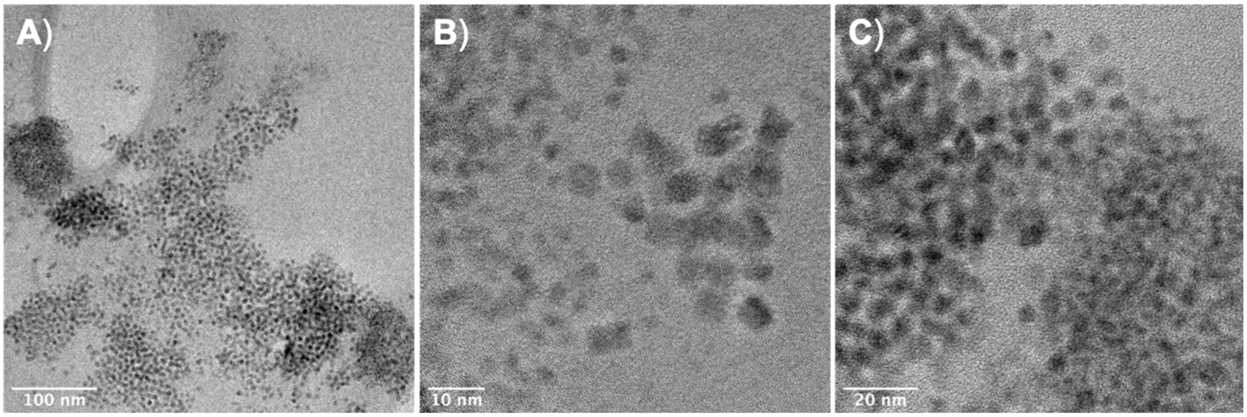

Figure 4.6. TEM images of assemblies prepared from InP/ZnSe QDs showing auto-segregation of core and core/shell QDs in separate structures.

The thickness of the two-dimensional QD assemblies was investigated using tomography to probe the 3D structure (Figure 4.7). CdS aggregates formed under standard conditions were drop-cast onto a TEM grid and dried overnight under vacuum. An area of interest containing QD sheet assemblies was identified and tilted from -65° to 65°, and images were acquired every 5° after drift and focus correction. After acquisition and further alignment, a 38.7 nm wide aggregate at neutral tilt measured 19.7 nm wide at 65°. Assuming a 5.3 nm thick QD monolayer at 40 nm wide, the expected width for the aggregate would be 19.4 nm, in good agreement with the measured results. Occasionally, bilayers were observed, appearing as overlapping QDs at 0° tilt. Tomography analysis performed on larger sheets, on the order of several hundred nanometers, showed less monolayer-like structure with more QDs binding outside the main plane. The measured width of a 231 nm aggregate at 65° tilt was 124 nm, with the expected width of a single monolayer being 102 nm and a bilayer being 187 nm. This suggests about 25% of the observed aggregate shows bilayer character, due to QDs binding outside the primary plane in a random fashion rather than the formation of an additional layer. Additionally, tomography of an aggregate with large areas of extensive overlap showed two individual monolayer-like aggregates when tilted to 65°, confirming that the presence of bilayer structures is due to discrete monolayers where sheets have dried in close proximity, with overlap.

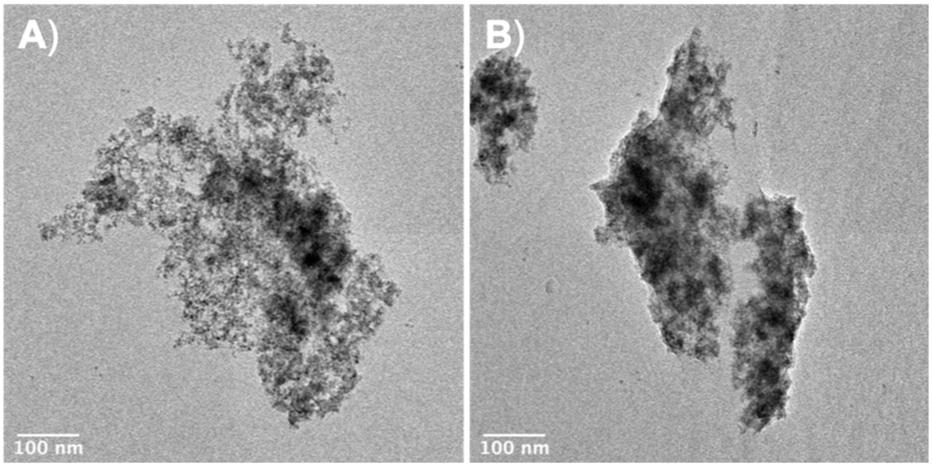

Figure 4.7. Tomography of CdS QD assemblies at 0° tilt (A) and 65° tilt (B) showing that what looks like a single assembly at 0° tilt is actually stacked 2D structures. Videos of the tomography data can be found in the Supporting Information.

One attractive feature of the 2,2'-bipyridine-5,5'-diacrylic acid linker is its ability to serve as a coordination site for transition metal ions. This feature could ultimately be used to drive tandem catalytic reactions.[63–68] and has been used here to confirm the presence of the 2,2'-bipyridine-5,5'-diacrylic acid linker. CdS assemblies deposited and dried on a TEM grid were submerged in a solution of $NiCl_2(PPh_3)_2$ and washed with CH_2Cl_2. Upon elemental mapping, high

Ni signal was seen in the assemblies co-localized with Cd and S, suggesting Ni on or near the surface of the QDs (Figure 4.8 A-D). Low background Ni signal was seen away from aggregates, likely due to peak overlap with Cu from the grid, confirming the enhanced Ni signal was due to uptake in the QD assemblies and not Ni dried non-specifically on the grid surface. We have corroborated the high affinity of the QD assemblies for Ni using ICP-MS, which showed nearly quantitative uptake relative to the concentration of the 2,2'-bipyridine-5,5'-diacrylic acid linker at low linker and Ni eq. (50 eq.), with Ni uptake relative to linker decreasing at higher linker and Ni eq. up to 250 eq. (Figure 4.8 E).

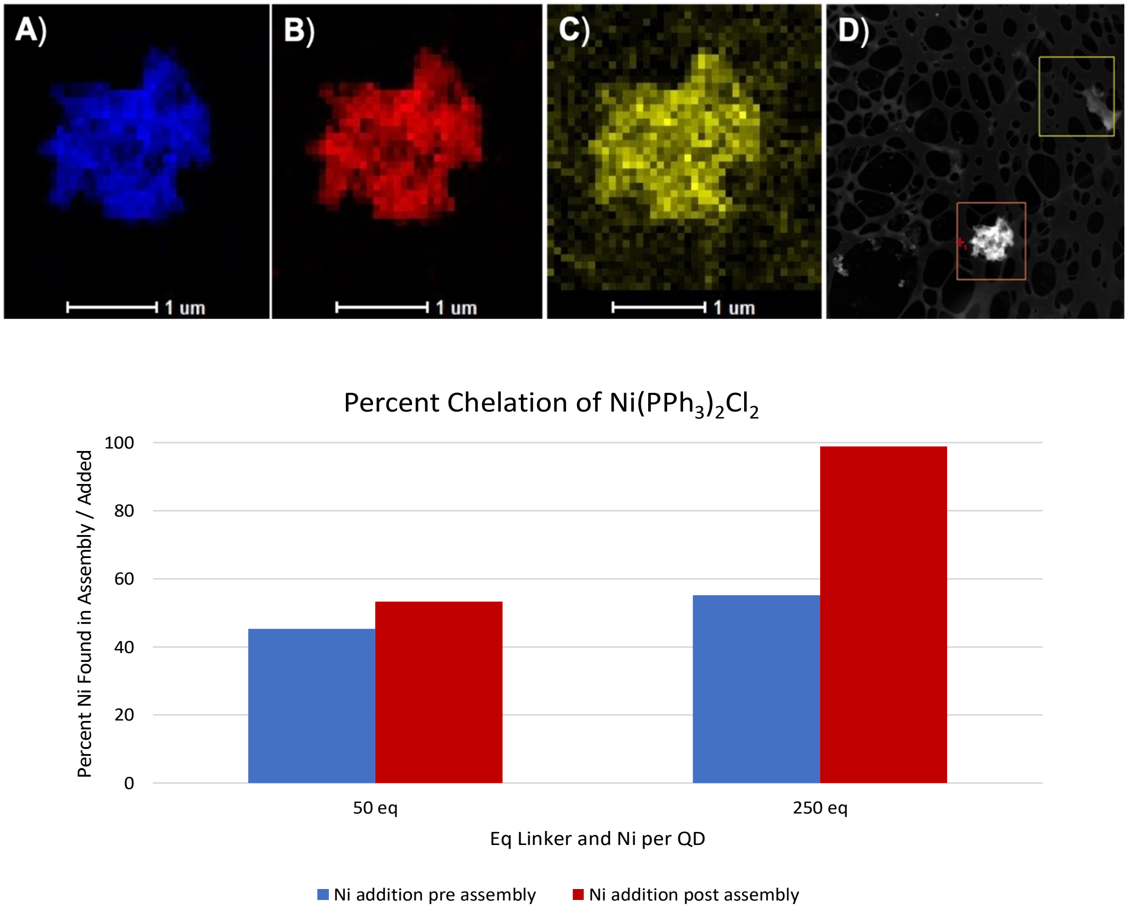

Figure 4.8. A-D) EDS mapping of CdS assemblies exposed to Ni^{2+} showing co-localization of Cd (blue), S (red), and Ni (yellow). E) ICP-MS data quantifying Ni^{2+} uptake in CdS assemblies.

Of the existing literature methods for creating directed, crystalline assemblies of nanoparticles, exploitation of either the geometry and dipole of the particle, or the use of complementary ligand interactions or templates is required. None of these mechanisms can explain the generality of spherical and quasi-spherical nanoparticles of various sizes forming anisotropic, 2D sheets with the addition of a single, symmetric, small molecule crosslinker as observed here. Moreover, multiple observations argue against an interfacial mechanism under these conditions. The solution is monophasic and stirred continuously to disrupt growth on the vessel wall or at a liquid-liquid interface, although interfacial assembly has been suggested in certain cases even in the case of agitated systems.[69] Further, the yield of sheets has a strong dependence on ligand identity (length and rigidity). Additionally, the starting aggregate morphology does not significantly rearrange to sheets at a lower concentration but with the same solution volume and vessel.

Considering these observations in conjunction with the dependence on concentration and equivalents of linker, we propose a ligand directed mechanism reliant on the formation of patchy QD surfaces. The native aliphatic ligand shell of QDs is dense, and steric repulsion is observed to dominate any Van der Waals or interdigitation effects at short distances.[24,25] In our system, the introduction of a low concentration of bifunctional linker with steric properties similar to that of the native ligand shell results in at least one thermodynamic minimum in the free energy landscape and the steric repulsion created by the ligand shell is minimized. As a result, the hierarchical assembly of isotropic units is observed and is likely controlled by the steric effects of the QD "ligands" in analogy with the electron pair repulsion model that governs geometry preferences in coordination chemistry (Scheme 4.2).[70,71] In the limit of two or three linking patches per QD, the formation of linear or hexagonal planar assemblies would be expected based on the thermodynamic preference to maximize the distance between QDs while concomitantly minimizing steric repulsion at their surfaces. While the natural valency of a QD is one to two orders of magnitude greater than that of a transition metal ion, the superlattice pseudo-valency is much smaller, in accordance with the larger 'patchy' equilibrium zones described here and in the theoretical literature.[50,72] Reorganization to the lowest energy configuration to maximize planarity requires significant ligand rearrangement at the nanoparticle surface and hundreds to thousands of kinetic steps. We therefore postulate that biscarboxylic acid linkers are ideal for these QD systems because ligand exchange for the native fatty acid ligands occurs with a K_{eq} ~1. While this value is generally reported for ligand exchange at room temperature, the temperature dependence is expected to be small given the measured value of about 30 J mol^{-1} K^{-1}.[73,74] If we were to use a linker that binds the particle irreversibly, linker redistribution would not be achievable, and the resulting products would be kinetically trapped amorphous aggregates as observed here prior to equilibration.

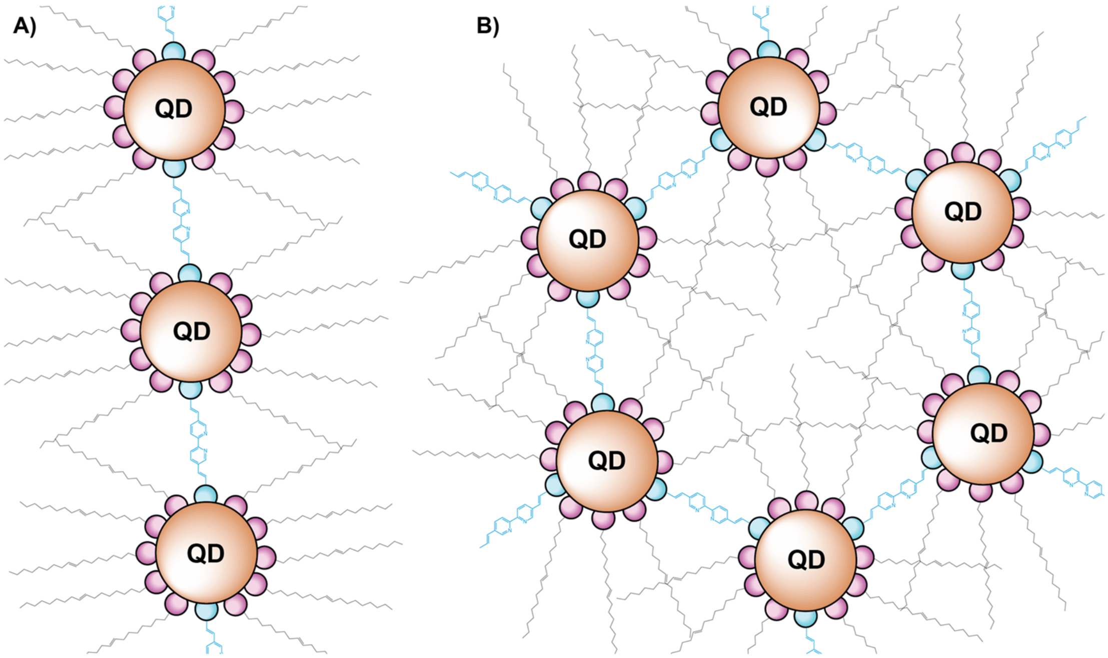

Scheme 4.2. Simplified depiction of one- (A) and two- (B) dimensional QD assemblies.

The standard conditions for the two-dimensional assembly described above used 50 eq. of linker per QD. Based on previous measurements in the literature, we can estimate that each QD has about 200 native oleate ligands per particle and an exchange equilibrium constant of ap-proximately 1. Given two binding groups per linker, the most basic theoretical equilibrium ligation sphere would comprise approximately 33% bifunctional ligands and 67% oleate ligands. By perturbing the concentration of bifunctional linker ligand to 10 eq. and 1250 eq. relative to QD, we targeted ligation spheres containing 9% and 93% bifunctional ligands respectively, assuming ideal exchange. In the case of adding only 10 eq. 2,2'-bipyridine-5,5'-diacrylic acid, two-dimensional sheets are still observed with the average sheet size being an order of magnitude larger than under standard conditions, with the low equivalence sheets averaging over 5 microns for a given sheet edge and the standard sheets averaging 500 nm (Figure 4.9 A, B, Figure 4.10). Additionally, hardly any sheets were seen to be stacking with the main population being flat monolayers. In contrast, the use of 1250 eq. 2,2'-bipyridine-5,5'-diacrylic acid yielded exclusively large, three dimensional aggregates (Figure 4.9 C). These observations are in line with our sterically based patchy ligand hypothesis as substitution of too many native oleate ligands removes the barrier to aggregation in three dimensions.

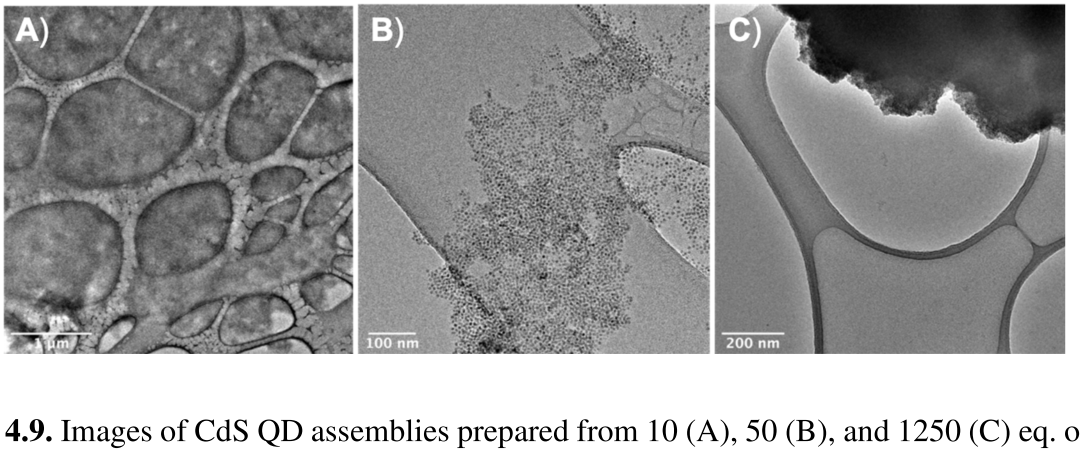

Figure 4.9. Images of CdS QD assemblies prepared from 10 (A), 50 (B), and 1250 (C) eq. of 2,2'-bipyridine-5,5'-diacrylic acid.

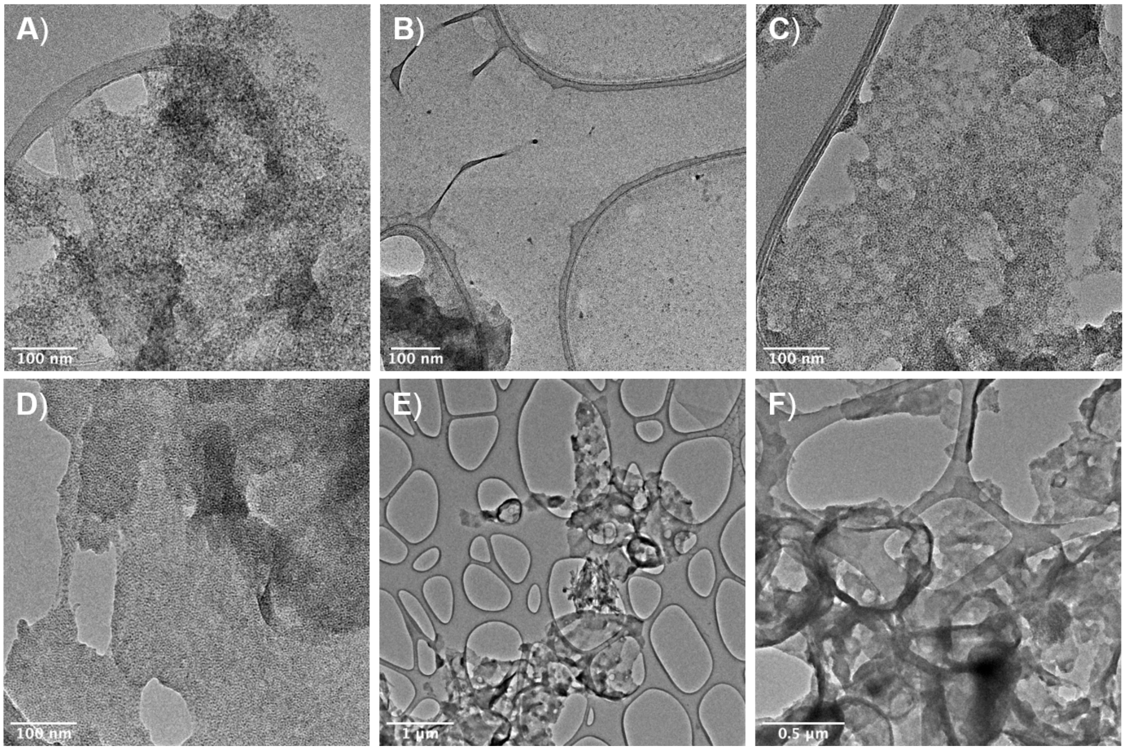

Fig 4.10. TEM Images of CdS nanoparticle sheets formed at standard conditions using 10 eq. of 2,2'-bipyridine-5,5'-diacrylic acid exhibiting relatively large monolayer areas.

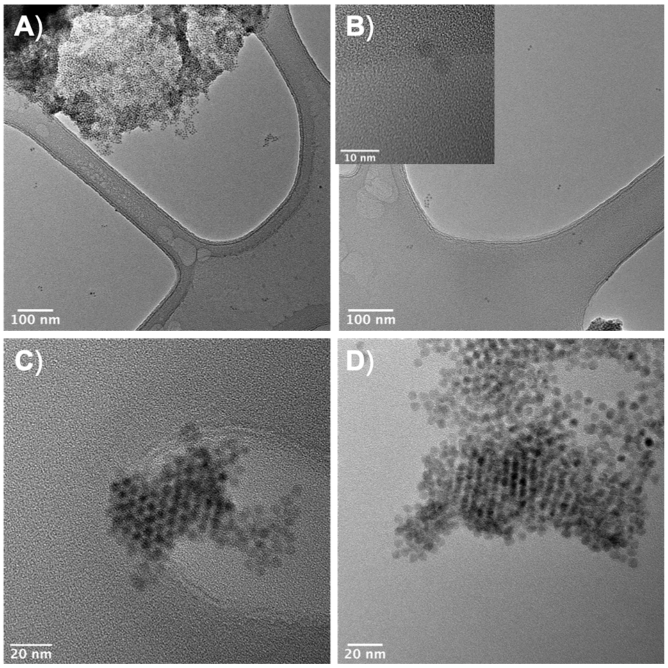

Figure 4.11. Images of CdS QD assemblies starting from 0.2 mM (A, B) and 20 mM QDs (C, D).

Finally, the dependence of QD assembly on total concentration was explored in an effort to elucidate the kinetic barrier towards 2D sheet formation. At ten times lower concentration (0.2 mM QDs) relatively few sheets were observed, and the material exhibited a predominantly unchanged morphology like the amorphous aggregates formed upon initial mixing at the standard 2 mM concentration. Notably, a population of non-aggregated particles was observed and appeared to be dimer and trimer clusters with few lone, singular particles (Figure 4.11 A, B). Inhibition of sheet formation at low concentration, with small clusters forming instead, implies that the directed self-assembly arises from particle-particle interactions and not particle-interface interaction. It is also in accordance with analysis of higher concentrations at earlier time points, implying that the mechanism is the same in both concentration regimes but with a kinetic dependence on quantum dot concentration. Performing assembly at ten times higher concentration (20 mM QDs) yielded high quality sheets that began to exhibit crystalline superlattice hcp ordering. These superlattices were only observed in areas that appeared to be multilayered suggesting the emergence of three-dimensional order. These concentration tests were otherwise run with the same volume and in the same type of vessel. The overall concentration effect on both rate and degree of assembly implies that the mechanism of sheet assembly is not dependent on interfacial effects, but instead driven by kinetically limited particle-particle interactions.

4.3 Conclusion

Using nanoparticle building blocks to construct hierarchical materials is a radical new branch point in materials discovery that promises new structures and emergent functionality. Understanding the design principles that govern nanoparticle assembly, especially in the most basic system using non-tailored, 0-dimensional nanoparticle building blocks, is critical to moving this field forward. Here we have demonstrated a novel method for the solution-based assembly of 2D QD sheets using simple molecular linkers. Furthermore, we have shown that this method is generalizable across nanoparticle sizes and compositions. Using a combination of TEM, DLS, and SAXS measurements we demonstrated that the formation of two-dimensional sheets is driven by a mechanism in which kinetically formed amorphous, three dimensional aggregates preferentially convert to the sheet morphology over time. We propose that this morphological evolution is driven by ligand redistribution to create a patchy surface that maximizes steric repulsion of neighboring QD “ligands”. By operating in an under-exchanged regime, the arising patchy-ness results in enthalpically preferred directions of crosslinking that can be accessed by thermal equilibration at moderate temperature. Essential to the success of this approach is the use of readily exchangeable surface ligands with K_{eq} close to 1 and linkers of similar length to the native surfactant on the QD surface. We believe these two-dimensional structures will provide exciting opportunities for the examination of exciton and charge transfer dynamics and will hold promise as light harvesting complexes in photoredox catalysis.

4.4 Experimental

4.4.1 General Practices

Unless stated otherwise, all chemical reactions were performed under N_2 using standard Schlenk line air-free techniques. Chemicals were stored dried in a N_2 glovebox unless stated otherwise. Purified quantum dots were stored in stock solutions in toluene and concentrations were determined by UV-Vis spectroscopy.[75,76] All other chemicals were stored dried and stock solutions for their use were made and used within 8 h.

4.4.2 Experimental Procedures, Synthetic

4.4.2.1 Synthesis of CdS QDs

CdS QDs were synthesized using an adapted literature method using tetramethyl thiourea and cadmium oleate ($CdOl_2$) precursors.[77] In a glovebox, a 500 mL three neck round-bottomed flask was charged with 2.430 g (3.60 mol, 1.2 eq.) of $CdOl_2$, 140 mL of dried octadecene (ODE), and 2.040 mL oleic acid (7.20 mmol, 2.4 eq.), and the vessel was transferred to a Schlenk line. Due to the lack of solubility in ODE, for the injection medium a mixture of 74% diphenyl ether and 26% biphenyl was prepared. In the glovebox, 396 mg (3.00 mmol, 1.0 eq.) of tetramethyl thiourea was measured and dissolved in 5.0 mL of this mixture. The reaction vessel was raised to 230 °C and the thiourea was swiftly injected and allowed to react for 2 h. QD purification was performed in air. The particles were precipitated with acetone and isolated via centrifugation at 10,000 rpm. The particles were resuspended in 60 mL hexanes (divided) and precipitated again with acetone. The particles were then resuspended in 40 mL toluene and precipitated with 90 mL acetonitrile; this was repeated a total of three times. Drying in vacuo yielded a free-flowing yellow powder. Dried yield: 576 mg. Emission 476 nm ± 14 nm FWHM, PLQY 81%.

4.4.2.2 Synthesis of CdSe QDs

CdSe QDs were synthesized using an adapted method using selenourea and cadmium oleate precursors.[77] The procedure was performed as described using diphenyl-imidazole selenourea on a 2.5 mmol $CdOl_2$ scale. The product was isolated as an orange wax. Emission 527 nm ± 16 nm FWHM, PLQY 36%.

4.4.2.3 Synthesis of InP/ZnSeS QDs

InP/ZnSeS QDs were prepared as described by in the literature.[78] The procedure was performed as described on a 0.11 mmol In scale. The product was isolated as an orange wax. Emission 605 nm ± 25 nm FWHM, PLQY 60%.

4.4.2.4 Synthesis of Linkers

2,2'-bipyridine-5,5'-diacrylate-tBu was synthesized using a palladium catalyzed double Heck cross coupling as previously reported on the 3 mmol scale.[79] The crude product was filtered and recrystallized from acetone. ^{1}H NMR (300 MHz, Methylene Chloride-d_2) δ 8.78 (d, *J* = 2.2 Hz, 2H), 8.48 (d, *J* = 8.3 Hz, 2H), 7.99 (dd, *J* = 8.4, 2.3 Hz, 2H), 7.62 (d, *J* = 16.1 Hz, 2H), 6.51 (d, *J* = 16.1 Hz, 2H), 1.54 (d, *J* = 3.1 Hz, 18H). Mass Spec Theoretical m/z (MH$^+$) 409.2122, Found: m/z (MH$^+$) 409.2118.

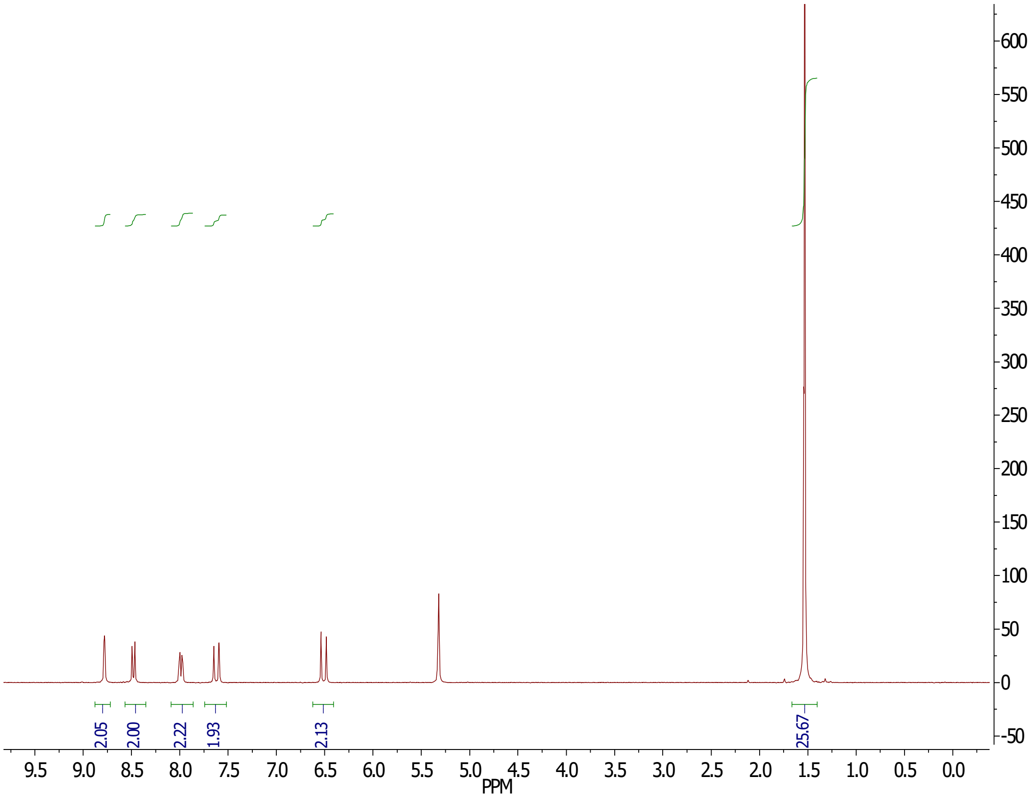

The ester group was cleaved by the addition of TFA and phenol in CH_2Cl_2 as described for $Ru(bpy)_2(bpyCOOH)Cl_2$ below, however the product is remarkably insoluble and was only observed to dissolve in basic aqueous solution and hot DMF. ^1H NMR (300 MHz, Deuterium Oxide) δ 8.64 (s, 2H), 8.14 – 7.87 (m, 4H), 7.30 (d, *J* = 16.1 Hz, 2H), 6.55 (d, *J* = 16.2 Hz, 2H).

2,2'-biphenyl-5,5'-diacrylate-tBu was synthesized using an adapted procedure involving a phosphine-free Heck cross coupling.[80] A 100 mL Schlenk flask was loaded with 1.872 g 4,4'-dibromo-biphenyl (6.0 mmol, 1.0 eq.), 1.538 g tertbutyl acrylate (12.0 mmol, 2.0 eq.), 31 mg palladium acetate (0.12 mmol, 0.02 eq.), and 24 mL triethanolamine. Triethanolamine was dried over 4 Å molecular sieves and degassed under vacuum prior to use. The vessel was equipped with a condensing column and raised to 100 °C for 14 h. The cloudy brown reaction mixture was diluted with 50 mL CH_2Cl_2 and filtered. The soluble phase was then extracted three times with 50 mL portions of H_2O. The organic layer was dried over $MgSO_4$, filtered, and the solvent was removed using a rotovap. The resulting yellow-white powder was dissolved in 4 mL CH_2Cl_2 and layered with 10 mL hexanes, immediately yielding 2,2'-biphenyl-5,5'-diacrylate-tBu as crystalline white flakes. ^1H NMR (300 MHz, Methylene Chloride-d_2) δ 7.61 (d, *J* = 15.8 Hz, 10H), 6.42 (d, *J* = 16.0 Hz, 2H), 1.53 (s, 18H).

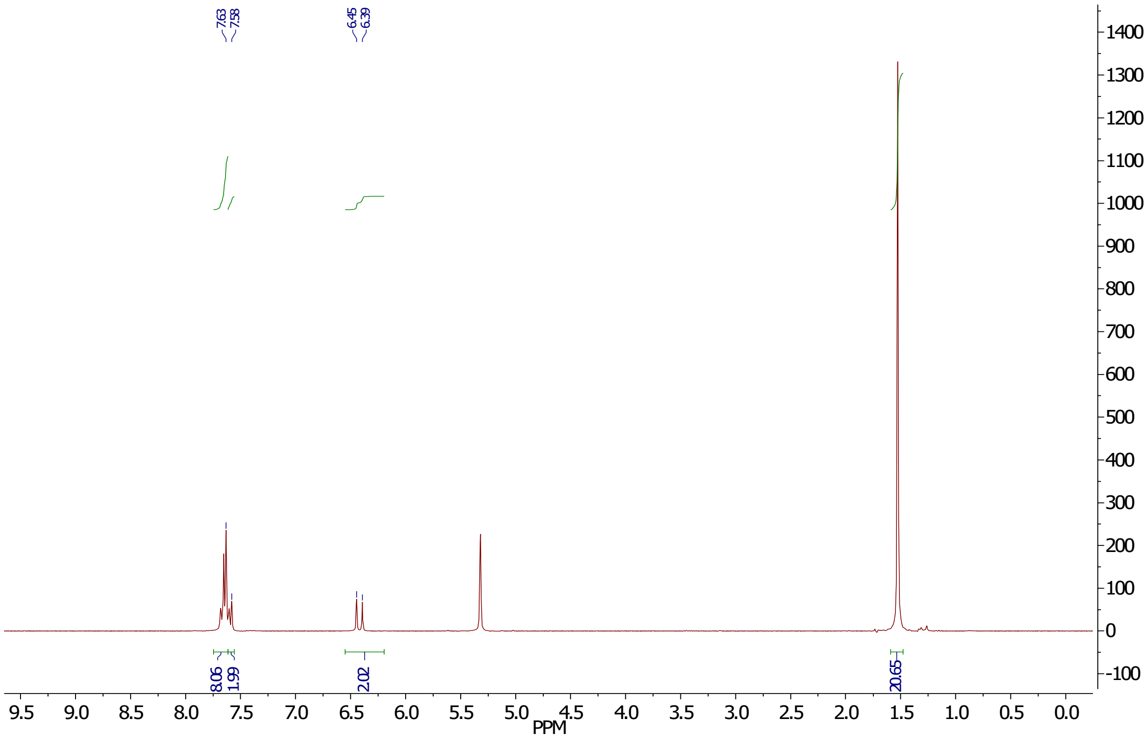

4.4.2.5 Synthesis of Ru(bpy)$_2$(2,2'-bpy-5,5'-diacrylic acid)Cl$_2$

A round bottom flask was loaded with 108 mg of Ru(bpy)$_2$Cl$_2$ (0.223 mmol, 1 eq.) and 100 mg 2,2'-bipyridine-5,5'-diacrylate-tBu (0.245 mmol, 1.1 eq.) and charged with 35 mL 200 proof EtOH. The Solution was sparged with N_2 for 10 min and then the vessel was equipped with a condensing column and connected to a Schlenk line under N_2. The solution was refluxed with stirring for 5 h. The resulting deep red solution was allowed to cool, and the solvent was removed by rotovap leaving a dark red-black solid. The solid was dissolved in 15 mL H_2O, filtered through a glass frit leaving a black solid, and the eluent was dried via rotovap at 50 °C. The product, Ru(bpy)$_2$(2,2'-bpy-5,5'-diacrylate-tBu)Cl$_2$, was isolated as a dark red powder, 73 mg, 40% yield.

For ester cleavage, the esterified complex was dissolved in 2 mL CH_2Cl_2 (82 umol, 1.0 eq.), and 166 mg phenol (1.7 mmol, 20.0 eq.), and 0.15 mL trifluoroacetic acid (0.9 mmol, 11 eq.) were added. The solution was stirred at room temperature for 2 h. Solvent and excess phenol were removed under vacuum at elevated temperature. The remaining powder was dissolved in 1 mL CH_2Cl_2, layered with 5 mL hexanes, and allowed to slowly recrystallize in a -20 °C freezer yielding red-orange single crystals that were used for single crystal X-ray diffraction analysis.

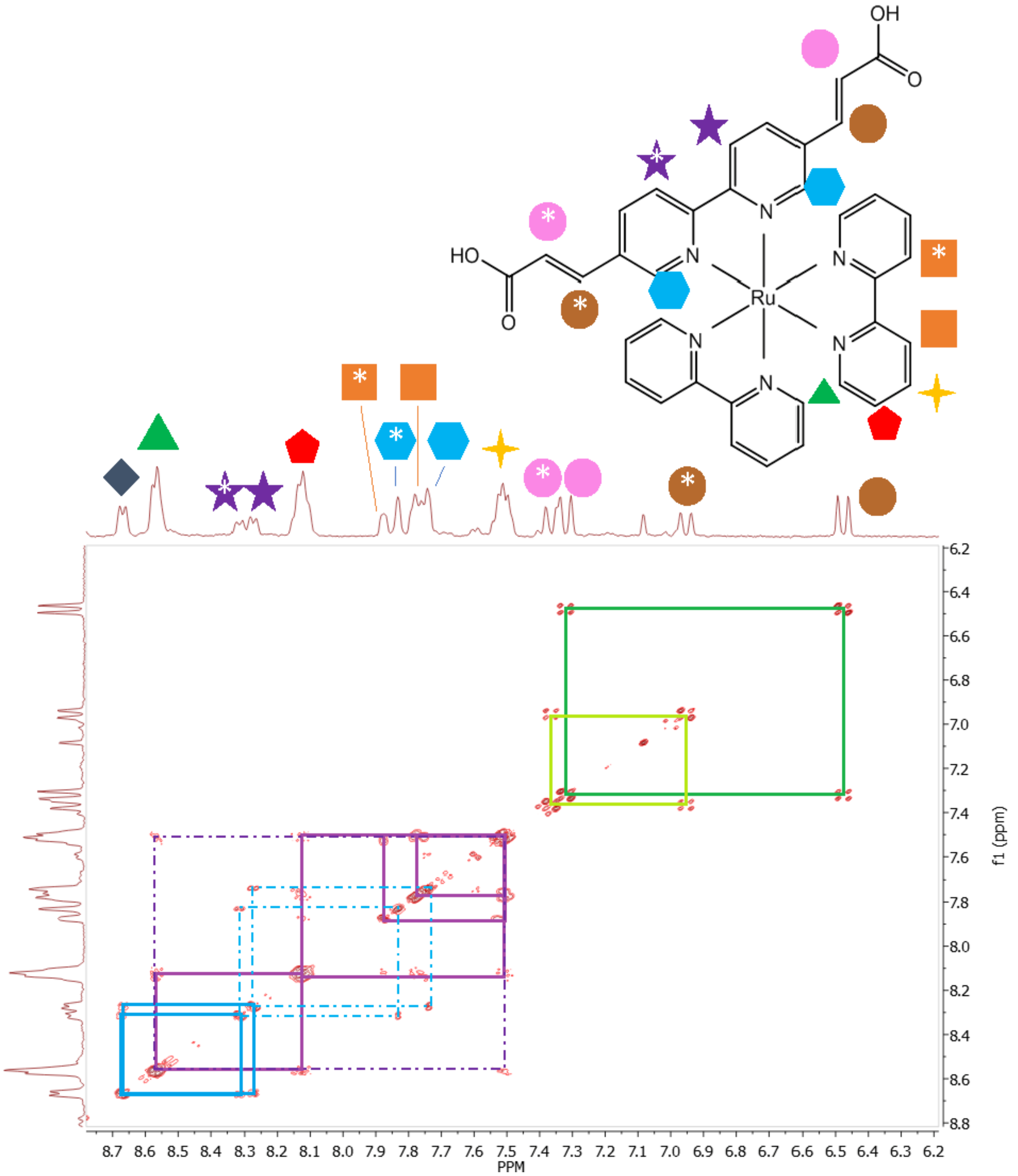

4.4.2.6 General Assembly Method

The assembly method is identical for all quantum dot compositions. Typical conditions employed CdS QDs and 2,2'-bipyridine-5,5'-diacrylate-tBu as a linker precursor. From a toluene stock solution stored in a glovebox, 0.8 - 80 nmol (8 typical) of QDs (1.0 eq.) are transferred to a glass Schlenk bomb with a magnetic stir bar. The solvent is removed by vacuum and the QDs are resuspended in 3 mL CH_2Cl_2. Stock solutions of linker were prepared the day of use using CH_2Cl_2 for esterified linkers and DMF for bis-carboxylic acids. Using a microliter syringe 10 - 1,250 eq (typical 50 eq.) of linker are measured and added to the QD solution. For esterified linkers a solution of trifluoroacetic acid (TFA) in CH_2Cl_2 is prepared and 5 eq. per carboxylate (i.e., 100 - 12,500 eq. per QD, typical 500 eq.) of TFA is added. The solution is left to equilibrate for 1 h with stirring. Solvent and excess TFA are removed by vacuum and 2 mL of each toluene and DMF are added. The Schlenk bombs are sealed and brought out of the glovebox and are then transferred to an oil bath. The vessels are heated at 90 °C for up to 7 d. Aggregates are isolated by centrifugation at 6,000 rpm usually yielding a clear supernatant without the use of antisolvent. The solid is shaken with 5 mL acetonitrile and centrifuged again a total of three times.

4.4.3 Experimental Procedures, Analytical

4.4.3.1 ICP-MS Details

Elemental analysis was performed using a Perkin Elmer NexION 2000B ICP-MS. Samples were dried and digested overnight in 67% ICP grade nitric acid then diluted to 2% concentration using 18 MΩ water and filtered. Samples were further quantitatively diluted to the 10-100 ppb range with additional pure 2% nitric acid solution.

The chelation ability of bipyridine-linked aggregates was tested using this method. Four aggregate samples were prepared in total as described by the general assembly method, two at 50 eq. linker and two at 250 eq. linker. For each series a respective amount of $Ni(PPh_3)_2Cl_2$, 50 or 250 eq, was added either before or after aggregation for a total of four samples. Prior to digestion samples were centrifuged at 10,000 rpm to separate precipitate from supernatant and each phase was tested separately.

4.4.3.2 DLS Details

Dynamic light scattering (DLS) measurements were performed using a Malvern Zetasizer Pro with a 632 nm laser, above the bandgap of the studied quantum dots to minimize fluorescent convolution. Samples were prepared in dilute solutions of toluene in a quartz cuvette and sonicated immediately prior to measurement at 22 °C. Scattering data were fit using a cumulant model in the Malvern Zetasizer software.

4.4.3.3 TEM Analysis

All imaging was done on a FEI Tecnai G2 F20 transmission electron microscope operated at 200 kV. Standard samples were prepared via drop-casting dilute aggregate suspension in toluene (5 mL) onto ultrathin carbon film on a lacey carbon support film, 400 mesh, copper grids purchased from Ted Pella Inc, allowed to dry fully then placed under vacuum overnight. Tomography samples were prepared as previously described on carbon support film, 200 mesh, copper pinpointer grids purchased from Ted Pella Inc. Analysis of aggregates was done in Image J[81] with the uncompressed .dm3 file with an average of 350 measurements (diameters and spacings) per average value reported. No enhancements or further processing was done to the images.

4.4.3.4 Synchrotron Details

Small angle X-ray scattering (SAXS) was performed using beamline 1-5 of the Stanford Synchrotron Radiation Light Source at the SLAC National Laboratory. Data were acquired using a 1 m detector distance configuration using a PILATUS 100K 2D detector and at 10.5 keV. Samples were prepared in 1 mm quartz cuvettes produced by Charles Supper Co at concentrations of about 5 mg/mL and sealed with epoxy. SAXS data were analyzed using SasView, an open source project developed in part by the NSF and NIST.[82] The background was determined using an external capillary of solvent as a baseline reference and data were normalized to the beam-stop intensity.

4.4.3.5 SAXS Fitting

SAXS data were fit using SasView software using unweighted least squares regression. Background subtraction was performed using an external solvent capillary and data were normalized to the beam-stop intensity. Polydispersity was modeled as a gaussian distribution, ranges represent one standard deviation. Polydispersity in spacing was not fit.

Sphere Model: A Guinier and G. Fournet, *Small-Angle Scattering of X-Rays*, John Wiley and Sons, New York, (1955).

Pearl-Necklace Model: R Schweins and K Huber, *Particle Scattering Factor of Pearl Necklace Chains*, *Macromol. Symp.* 211 (2004) 25-42 2004.

Structure Factor Analysis:

The procedure for extracting a structure factor for quantum dot films has been previously investigated by Murray, Kagan, and Bawendi as described in principle by Klug. Here we apply the same approach for our colloidally stable assemblies.

General total scattering by N particles is described by:

$$I(q) = I(q)_0 N\, F^2(q) S(q) \tag{4.1}$$

Where $F^2(q)$ is the form factor of an individual particle and S(q) is the structure factor relating interparticle order and scatter interference.

By first determining the form factor via a dispersed (i.e. uncorrelated) nanoparticle solution where $S(q)_{Solv} = 1$ the structure factor of the assembly may then be solved for directly by dividing the assembled total scattering by the dispersed (experimental) nanoparticle form factor:

$$\frac{I(q)_{Assembly}}{I(q)_0 N\, F^2(q)} = S(q)_{Assembly} \tag{4.2}$$

4.5 References

(1) Basic Research Needs for Synthesis Science. 178.

(2) Gröschel, A. H.; Walther, A.; Löbling, T. I.; Schacher, F. H.; Schmalz, H.; Müller, A. H. E. Guided Hierarchical Co-Assembly of Soft Patchy Nanoparticles. *Nature* **2013**, *503* (7475), 247–251. https://doi.org/10.1038/nature12610.

(3) Sanchez, C.; Soler-Illia, G. J. D. A. A.; Ribot, F.; Grosso, D. Design of Functional Nano-Structured Materials through the Use of Controlled Hybrid Organic–Inorganic Interfaces. *Comptes Rendus Chim.* **2003**, *6* (8), 1131–1151. https://doi.org/10.1016/j.crci.2003.06.001.

(4) Zhong, X.; Lee, K.; Choi, B.; Meggiolaro, D.; Liu, F.; Nuckolls, C.; Pasupathy, A.; De Angelis, F.; Batail, P.; Roy, X.; Zhu, X. Superatomic Two-Dimensional Semiconductor. *Nano Lett.* **2018**, *18* (2), 1483–1488. https://doi.org/10.1021/acs.nanolett.7b05278.

(5) Nie, Z.; Petukhova, A.; Kumacheva, E. Properties and Emerging Applications of Self-Assembled Structures Made from Inorganic Nanoparticles. *Nat. Nanotechnol.* **2010**, *5* (1), 15–25. https://doi.org/10.1038/nnano.2009.453.

(6) Hanske, C.; Tebbe, M.; Kuttner, C.; Bieber, V.; Tsukruk, V. V.; Chanana, M.; König, T. A. F.; Fery, A. Strongly Coupled Plasmonic Modes on Macroscopic Areas via Template-Assisted Colloidal Self-Assembly. *Nano Lett.* **2014**, *14* (12), 6863–6871. https://doi.org/10.1021/nl502776s.

(7) Ong, W.-L.; O'Brien, E. S.; Dougherty, P. S. M.; Paley, D. W.; Fred Higgs Iii, C.; McGaughey, A. J. H.; Malen, J. A.; Roy, X. Orientational Order Controls Crystalline and Amorphous Thermal Transport in Superatomic Crystals. *Nat. Mater.* **2017**, *16* (1), 83–88. https://doi.org/10.1038/nmat4739.

(8) Bhushan, B. Introduction: Biomimetics: Lessons from Nature - An Overview. *Philos. Trans. Math. Phys. Eng. Sci.* **2009**, *367* (1893), 1445–1486.

(9) Grzelczak, M.; Vermant, J.; Furst, E. M.; Liz-Marzán, L. M. Directed Self-Assembly of Nanoparticles. *ACS Nano* **2010**, *4* (7), 3591–3605. https://doi.org/10.1021/nn100869j.

(10) Campbell, M.; Sharp, D. N.; Harrison, M. T.; Denning, R. G.; Turberfield, A. J. Fabrication of Photonic Crystals for the Visible Spectrum by Holographic Lithography. *Nature* **2000**, *404* (6773), 53–56. https://doi.org/10.1038/35003523.

(11) Zhang, J.; Liu, Y.; Ke, Y.; Yan, H. Periodic Square-Like Gold Nanoparticle Arrays Templated by Self-Assembled 2D DNA Nanogrids on a Surface. *Nano Lett.* **2006**, *6* (2), 248–251. https://doi.org/10.1021/nl052210l.

(12) Rosseeva), E. V. S. (née; Cölfen, H. Mesocrystals: Structural and Morphogenetic Aspects. *Chem. Soc. Rev.* **2016**, *45* (21), 5821–5833. https://doi.org/10.1039/C6CS00208K.

(13) Yuwono, V. M.; Burrows, N. D.; Soltis, J. A.; Penn, R. L. Oriented Aggregation: Formation and Transformation of Mesocrystal Intermediates Revealed. *J. Am. Chem. Soc.* **2010**, *132* (7), 2163–2165. https://doi.org/10.1021/ja909769a.

(14) Vlasov, Y. A.; Yao, N.; Norris, D. J. Synthesis of Photonic Crystals for Optical Wavelengths from Semiconductor Quantum Dots. *Adv. Mater.* **1999**, *11* (2), 165–169. https://doi.org/10.1002/(SICI)1521-4095(199902)11:2<165::AID-ADMA165>3.0.CO;2-3.

(15) Shevchenko, E. V.; Talapin, D. V.; Kotov, N. A.; O'Brien, S.; Murray, C. B. Structural Diversity in Binary Nanoparticle Superlattices. *Nature* **2006**, *439* (7072), 55–59. https://doi.org/10.1038/nature04414.

(16) Jena, P.; Sun, Q. Super Atomic Clusters: Design Rules and Potential for Building Blocks of Materials. *Chem. Rev.* **2018**, *118* (11), 5755–5870. https://doi.org/10.1021/acs.chemrev.7b00524.

(17) Brock, S. L.; Arachchige, I. U.; Kalebaila, K. K. Metal Chalcogenide Gels, Xerogels and Aerogels. *Comments Inorg. Chem.* **2006**, *27* (5–6), 103–126. https://doi.org/10.1080/02603590601084434.

(18) Arachchige, I. U.; Brock, S. L. Sol–Gel Methods for the Assembly of Metal Chalcogenide Quantum Dots. *Acc. Chem. Res.* **2007**, *40* (9), 801–809. https://doi.org/10.1021/ar600028s.

(19) Nakazawa, N.; Zhang, Y.; Liu, F.; Ding, C.; Hori, K.; Toyoda, T.; Yao, Y.; Zhou, Y.; Hayase, S.; Wang, R.; Zou, Z.; Shen, Q. The Interparticle Distance Limit for Multiple Exciton Dissociation in PbS Quantum Dot Solid Films. *Nanoscale Horiz.* **2019**, *4* (2), 445–451. https://doi.org/10.1039/C8NH00341F.

(20) Lilly, G. D.; Whalley, A. C.; Grunder, S.; Valente, C.; Frederick, M. T.; Stoddart, J. F.; Weiss, E. A. Switchable Photoconductivity of Quantum Dot Films Using Cross-Linking Ligands with Light-Sensitive Structures. *J. Mater. Chem.* **2011**, *21* (31), 11492–11497. https://doi.org/10.1039/C0JM04397D.

(21) Zhou, H.-C.; Long, J. R.; Yaghi, O. M. Introduction to Metal–Organic Frameworks. *Chem. Rev.* **2012**, *112* (2), 673–674. https://doi.org/10.1021/cr300014x.

(22) Ding, S.-Y.; Wang, W. Covalent Organic Frameworks (COFs): From Design to Applications. *Chem. Soc. Rev.* **2012**, *42* (2), 548–568. https://doi.org/10.1039/C2CS35072F.

(23) Korala, L.; Li, L.; Brock, S. L. Transparent Conducting Films of CdSe(ZnS) Core(Shell) Quantum Dot Xerogels. *Chem. Commun.* **2012**, *48* (68), 8523–8525. https://doi.org/10.1039/C2CC34188C.

(24) Korgel, B. A.; Fitzmaurice, D. Condensation of Ordered Nanocrystal Thin Films. *Phys. Rev. Lett.* **1998**, *80* (16), 3531–3534. https://doi.org/10.1103/PhysRevLett.80.3531.

(25) Kodaimati, M. S.; Wang, C.; Chapman, C.; Schatz, G. C.; Weiss, E. A. Distance-Dependence of Interparticle Energy Transfer in the Near-Infrared within Electrostatic Assemblies of PbS Quantum Dots. *ACS Nano* **2017**, *11* (5), 5041–5050. https://doi.org/10.1021/acsnano.7b01778.

(26) Tang, Z.; Zhang, Z.; Wang, Y.; Glotzer, S. C.; Kotov, N. A. Self-Assembly of CdTe Nanocrystals into Free-Floating Sheets. *Science* **2006**, *314* (5797), 274–278. https://doi.org/10.1126/science.1128045.

(27) Ghezelbash, A.; Koo, B.; Korgel, B. A. Self-Assembled Stripe Patterns of CdS Nanorods. *Nano Lett.* **2006**, *6* (8), 1832–1836. https://doi.org/10.1021/nl061035l.

(28) Malakooti, R.; Cademartiri, L.; Akçakir, Y.; Petrov, S.; Migliori, A.; Ozin, G. A. Shape-Controlled Bi2S3 Nanocrystals and Their Plasma Polymerization into Flexible Films. *Adv. Mater.* **2006**, *18* (16), 2189–2194. https://doi.org/10.1002/adma.200600460.

(29) Carbone, L.; Nobile, C.; De Giorgi, M.; Sala, F. D.; Morello, G.; Pompa, P.; Hytch, M.; Snoeck, E.; Fiore, A.; Franchini, I. R.; Nadasan, M.; Silvestre, A. F.; Chiodo, L.; Kudera, S.; Cingolani, R.; Krahne, R.; Manna, L. Synthesis and Micrometer-Scale Assembly of Colloidal CdSe/CdS Nanorods Prepared by a Seeded Growth Approach. *Nano Lett.* **2007**, *7* (10), 2942–2950. https://doi.org/10.1021/nl0717661.

(30) Qiao, F.; Wang, X.; Wang, Q.; He, G.; Xie, Y. Functionalized Self-Assembly of Colloidal CdX (X = S, Se) Nanorods on Solid Substrates for Device Applications. *Nanoscale* **2017**, *9* (24), 8066–8079. https://doi.org/10.1039/C7NR01974B.

(31) Lin, Q.-Y.; Mason, J. A.; Li, Z.; Zhou, W.; O'Brien, M. N.; Brown, K. A.; Jones, M. R.; Butun, S.; Lee, B.; Dravid, V. P.; Aydin, K.; Mirkin, C. A. Building Superlattices from Individual Nanoparticles via Template-Confined DNA-Mediated Assembly. *Science* **2018**, *359* (6376), 669–672. https://doi.org/10.1126/science.aaq0591.

(32) Krajina, B. A.; Proctor, A. C.; Schoen, A. P.; Spakowitz, A. J.; Heilshorn, S. C. Biotemplated Synthesis of Inorganic Materials: An Emerging Paradigm for Nanomaterial Synthesis Inspired by Nature. *Prog. Mater. Sci.* **2018**, *91*, 1–23. https://doi.org/10.1016/j.pmatsci.2017.08.001.

(33) Li, H.; Park, S. H.; Reif, J. H.; LaBean, T. H.; Yan, H. DNA-Templated Self-Assembly of Protein and Nanoparticle Linear Arrays. *J. Am. Chem. Soc.* **2004**, *126* (2), 418–419. https://doi.org/10.1021/ja0383367.

(34) Park, J.; Lu, W. Orientation of Core-Shell Nanoparticles in an Electric Field. *Appl. Phys. Lett.* **2007**, *91* (5), 053113. https://doi.org/10.1063/1.2767191.

(35) Vigderman, L.; Khanal, B. P.; Zubarev, E. R. Functional Gold Nanorods: Synthesis, Self-Assembly, and Sensing Applications. *Adv. Mater.* **2012**, *24* (36), 4811–4841. https://doi.org/10.1002/adma.201201690.

(36) Tebbe, M.; Mayer, M.; Glatz, B. A.; Hanske, C.; Probst, P. T.; Müller, M. B.; Karg, M.; Chanana, M.; König, T. A. F.; Kuttner, C.; Fery, A. Optically Anisotropic Substrates via Wrinkle-Assisted Convective Assembly of Gold Nanorods on Macroscopic Areas. *Faraday Discuss.* **2015**, *181* (0), 243–260. https://doi.org/10.1039/C4FD00236A.

(37) Mirkin, C. A.; Letsinger, R. L.; Mucic, R. C.; Storhoff, J. J. A DNA-Based Method for Rationally Assembling Nanoparticles into Macroscopic Materials. *Nature* **1996**, *382* (6592), 607–609. https://doi.org/10.1038/382607a0.

(38) Macfarlane, R. J.; Lee, B.; Jones, M. R.; Harris, N.; Schatz, G. C.; Mirkin, C. A. Nanoparticle Superlattice Engineering with DNA. *Science* **2011**, *334* (6053), 204–208. https://doi.org/10.1126/science.1210493.

(39) Nykypanchuk, D.; Maye, M. M.; van der Lelie, D.; Gang, O. DNA-Guided Crystallization of Colloidal Nanoparticles. *Nature* **2008**, *451* (7178), 549–552. https://doi.org/10.1038/nature06560.

(40) Park, S. Y.; Lytton-Jean, A. K. R.; Lee, B.; Weigand, S.; Schatz, G. C.; Mirkin, C. A. DNA-Programmable Nanoparticle Crystallization. *Nature* **2008**, *451* (7178), 553–556. https://doi.org/10.1038/nature06508.

(41) Zheng, J.; Constantinou, P. E.; Micheel, C.; Alivisatos, A. P.; Kiehl, R. A.; Seeman, N. C. Two-Dimensional Nanoparticle Arrays Show the Organizational Power of Robust DNA Motifs. *Nano Lett.* **2006**, *6* (7), 1502–1504. https://doi.org/10.1021/nl060994c.

(42) Tian, Y.; Lhermitte, J. R.; Bai, L.; Vo, T.; Xin, H. L.; Li, H.; Li, R.; Fukuto, M.; Yager, K. G.; Kahn, J. S.; Xiong, Y.; Minevich, B.; Kumar, S. K.; Gang, O. Ordered Three-Dimensional Nanomaterials Using DNA-Prescribed and Valence-Controlled Material Voxels. *Nat. Mater.* **2020**, 1–8. https://doi.org/10.1038/s41563-019-0550-x.

(43) Sacanna, S.; Irvine, W. T. M.; Chaikin, P. M.; Pine, D. J. Lock and Key Colloids. *Nature* **2010**, *464* (7288), 575–578. https://doi.org/10.1038/nature08906.

(44) Mihut, A. M.; Stenqvist, B.; Lund, M.; Schurtenberger, P.; Crassous, J. J. Assembling Oppositely Charged Lock and Key Responsive Colloids: A Mesoscale Analog of Adaptive Chemistry. *Sci. Adv.* **2017**, *3* (9), e1700321. https://doi.org/10.1126/sciadv.1700321.

(45) Gabrys, P. A.; Zornberg, L. Z.; Macfarlane, R. J. Programmable Atom Equivalents: Atomic Crystallization as a Framework for Synthesizing Nanoparticle Superlattices. *Small* **2019**, *15* (26), 1805424. https://doi.org/10.1002/smll.201805424.

(46) Santos, P. J.; Cao, Z.; Zhang, J.; Alexander-Katz, A.; Macfarlane, R. J. Dictating Nanoparticle Assembly via Systems-Level Control of Molecular Multivalency. *J. Am. Chem. Soc.* **2019**, *141* (37), 14624–14632. https://doi.org/10.1021/jacs.9b04999.

(47) Wang, Y.; Santos, P. J.; Kubiak, J. M.; Guo, X.; Lee, M. S.; Macfarlane, R. J. Multistimuli Responsive Nanocomposite Tectons for Pathway Dependent Self-Assembly and Acceleration of Covalent Bond Formation. *J. Am. Chem. Soc.* **2019**, *141* (33), 13234–13243. https://doi.org/10.1021/jacs.9b06695.

(48) Zhang, J.; Santos, P. J.; Gabrys, P. A.; Lee, S.; Liu, C.; Macfarlane, R. J. Self-Assembling Nanocomposite Tectons. *J. Am. Chem. Soc.* **2016**, *138* (50), 16228–16231. https://doi.org/10.1021/jacs.6b11052.

(49) Larson-Smith, K.; C. Pozzo, D. Scalable Synthesis of Self-Assembling Nanoparticle Clusters Based on Controlled Steric Interactions. *Soft Matter* **2011**, *7* (11), 5339–5347. https://doi.org/10.1039/C0SM01497D.

(50) Morphew, D.; Shaw, J.; Avins, C.; Chakrabarti, D. Programming Hierarchical Self-Assembly of Patchy Particles into Colloidal Crystals via Colloidal Molecules. *ACS Nano* **2018**, *12* (3), 2355–2364. https://doi.org/10.1021/acsnano.7b07633.

(51) Grünwald, M.; Geissler, P. L. Patterns without Patches: Hierarchical Self-Assembly of Complex Structures from Simple Building Blocks. *ACS Nano* **2014**, *8* (6), 5891–5897. https://doi.org/10.1021/nn500978p.

(52) Guinier, A.; Fournet, G. *Small-Angle Scattering of X-Rays*; Wiley, 1955.

(53) Schweins, R.; Huber, K. Particle Scattering Factor of Pearl Necklace Chains. *Macromol. Symp.* **2004**, *211* (1), 25–42. https://doi.org/10.1002/masy.200450702.

(54) Murray, C. B.; Kagan, C. R.; Bawendi, M. G. Synthesis and Characterization of Monodisperse Nanocrystals and Close-Packed Nanocrystal Assemblies. *Annu Rev Mater Sci* **2000**, *30*, 545–610.

(55) Kagan, C. R.; Murray, C. B.; Bawendi, M. G. Long-Range Resonance Transfer of Electronic Excitations in Close-Packed CdSe Quantum-Dot Solids. *Phys. Rev. B* **1996**, *54* (12), 8633–8643. https://doi.org/10.1103/PhysRevB.54.8633.

(56) Jarosz, M. V.; Porter, V. J.; Fisher, B. R.; Kastner, M. A.; Bawendi, M. G. Photoconductivity Studies of Treated CdSe Quantum Dot Films Exhibiting Increased Exciton Ionization Efficiency. *Phys. Rev. B* **2004**, *70* (19), 195327. https://doi.org/10.1103/PhysRevB.70.195327.

(57) Klug, H. P.; Alexander, L. E. *X-Ray Diffraction Procedures for Polycrystalline and Amorphous Materials.* John Wiley and Sons, New York, **1974**

(58) Kagan, C. R.; Lifshitz, E.; Sargent, E. H.; Talapin, D. V. Building Devices from Colloidal Quantum Dots. *Science* **2016**, *353* (6302). https://doi.org/10.1126/science.aac5523.

(59) Colbert, A. E.; Wu, W.; Janke, E. M.; Ma, F.; Ginger, D. S. Effects of Ligands on Charge Generation and Recombination in Hybrid Polymer/Quantum Dot Solar Cells. *J. Phys. Chem. C* **2015**, *119* (44), 24733–24739. https://doi.org/10.1021/acs.jpcc.5b07828.

(60) Murphy, J. E.; Beard, M. C.; Nozik, A. J. Time-Resolved Photoconductivity of PbSe Nanocrystal Arrays. *J. Phys. Chem. B* **2006**, *110* (50), 25455–25461. https://doi.org/10.1021/jp0646123.

(61) Yu, D.; Wang, C.; Wehrenberg, B. L.; Guyot-Sionnest, P. Variable Range Hopping Conduction in Semiconductor Nanocrystal Solids. *Phys. Rev. Lett.* **2004**, *92* (21), 216802. https://doi.org/10.1103/PhysRevLett.92.216802.

(62) Kovalenko, M. V.; Manna, L.; Cabot, A.; Hens, Z.; Talapin, D. V.; Kagan, C. R.; Klimov, V. I.; Rogach, A. L.; Reiss, P.; Milliron, D. J.; Guyot-Sionnnest, P.; Konstantatos, G.; Parak, W. J.; Hyeon, T.; Korgel, B. A.; Murray, C. B.; Heiss, W. Prospects of Nanoscience with Nanocrystals. *ACS Nano* **2015**, *9* (2), 1012–1057. https://doi.org/10.1021/nn506223h.

(63) Orchanian, N. M.; Hong, L. E.; Skrainka, J. A.; Esterhuizen, J. A.; Popov, D. A.; Marinescu, S. C. Surface-Immobilized Conjugated Polymers Incorporating Rhenium Bipyridine Motifs for Electrocatalytic and Photocatalytic CO2 Reduction. *ACS Appl. Energy Mater.* **2019**, *2* (1), 110–123. https://doi.org/10.1021/acsaem.8b01745.

(64) Wang, J.-L.; Wang, C.; Lin, W. Metal–Organic Frameworks for Light Harvesting and Photocatalysis. *ACS Catal.* **2012**, *2* (12), 2630–2640. https://doi.org/10.1021/cs3005874.

(65) Zhu, Y.-Y.; Lan, G.; Fan, Y.; Veroneau, S. S.; Song, Y.; Micheroni, D.; Lin, W. Merging Photoredox and Organometallic Catalysts in a Metal–Organic Framework Significantly Boosts Photocatalytic Activities. *Angew. Chem.* **2018**, *130* (43), 14286–14290. https://doi.org/10.1002/ange.201809493.

(66) Li, Z. J.; Li, X. B.; Wang, J. J.; Yu, S.; Li, C. B.; Tung, C. H.; Wu, L. Z. A Robust "Artificial Catalyst" in Situ Formed from CdTe QDs and Inorganic Cobalt Salts for Photocatalytic Hydrogen Evolution. *Energy Env. Sci* **2013**, *6*, 465–469.

(67) Kodaimati, M. S.; Lian, S.; Schatz, G. C.; Weiss, E. A. Energy Transfer-Enhanced Photocatalytic Reduction of Protons within Quantum Dot Light-Harvesting–Catalyst Assemblies. *Proc. Natl. Acad. Sci.* **2018**, *115* (33), 8290–8295. https://doi.org/10.1073/pnas.1805625115.

(68) Huang, C.; Li, X.-B.; Tung, C.-H.; Wu, L.-Z. Photocatalysis with Quantum Dots and Visible Light for Effective Organic Synthesis. *Chem. – Eur. J.* **2018**, *24* (45), 11530–11534. https://doi.org/10.1002/chem.201800391.

(69) Sanii, B.; Kudirka, R.; Cho, A.; Venkateswaran, N.; Olivier, G. K.; Olson, A. M.; Tran, H.; Harada, R. M.; Tan, L.; Zuckermann, R. N. Shaken, Not Stirred: Collapsing a Peptoid Monolayer To Produce Free-Floating, Stable Nanosheets. *J. Am. Chem. Soc.* **2011**, *133* (51), 20808–20815. https://doi.org/10.1021/ja206199d.

(70) Gillespie, R. J. The Electron-Pair Repulsion Model for Molecular Geometry. *J. Chem. Educ.* **1970**, *47* (1), 18. https://doi.org/10.1021/ed047p18.

(71) Gillespie, R. Teaching Molecular Geometry with the VSEPR Model. *J Chem Educ* **2004**, 1–4. https://doi.org/10.1021/ed081p298.

(72) De Nolf, K.; Cosseddu, S. M.; Jasieniak, J. J.; Drijvers, E.; Martins, J. C.; Infante, I.; Hens, Z. Binding and Packing in Two-Component Colloidal Quantum Dot Ligand Shells: Linear versus Branched Carboxylates. *J. Am. Chem. Soc.* **2017**. https://doi.org/10.1021/jacs.6b11328.

(73) Knauf, R. R.; Lennox, J. C.; Dempsey, J. L. Quantifying Ligand Exchange Reactions at CdSe Nanocrystal Surfaces. *Chem. Mater.* **2016**, *28* (13), 4762–4770. https://doi.org/10.1021/acs.chemmater.6b01827.

(74) Ritchhart, A.; Cossairt, B. M. Quantifying Ligand Exchange on InP Using an Atomically Precise Cluster Platform. *Inorg. Chem.* **2019**, *58* (4), 2840–2847. https://doi.org/10.1021/acs.inorgchem.8b03524.

(75) Yu, W. W.; Qu, L.; Guo, W.; Peng, X. Experimental Determination of the Extinction Coefficient of CdTe, CdSe, and CdS Nanocrystals. *Chem Mater* **2003**, *15*, 2854–2860.

(76) Xie, L.; Shen, Y.; Franke, D.; Sebastián, V.; Bawendi, M. G.; Jensen, K. F. Characterization of Indium Phosphide Quantum Dot Growth Intermediates Using MALDI-TOF Mass Spectrometry. *J. Am. Chem. Soc.* **2016**, *138* (41), 13469–13472. https://doi.org/10.1021/jacs.6b06468.

(77) S. Hamachi, L.; Yang, H.; Plante, I. J.-L.; Saenz, N.; Qian, K.; P. Campos, M.; T. Cleveland, G.; Rreza, I.; Oza, A.; Walravens, W.; M. Chan, E.; Hens, Z.; C. Crowther, A.; S. Owen, J. Precursor Reaction Kinetics Control Compositional Grading and Size of CdSe 1−x S x Nanocrystal Heterostructures. *Chem. Sci.* **2019**, *10* (26), 6539–6552. https://doi.org/10.1039/C9SC00989B.

(78) Lim, J.; Bae, W. K.; Lee, D.; Nam, M. K.; Jung, J.; Lee, C.; Char, K.; Lee, S. InP@ZnSeS, Core@Composition Gradient Shell Quantum Dots with Enhanced Stability. *Chem. Mater.* **2011**, *23* (20), 4459–4463. https://doi.org/10.1021/cm201550w.

(79) Ali, A.; Hussain, M.; Malik, I.; Villinger, A.; Fischer, C.; Langer, P. Double Heck Cross-Coupling Reactions of Dibrominated Pyridines. *Helv. Chim. Acta* **2010**, *93* (9), 1764–1772. https://doi.org/10.1002/hlca.201000108.

(80) Li, H. J.; Wang, L. Triethanolamine as an Efficient and Reusable Base, Ligand and Reaction Medium for Phosphane-Free Palladium-Catalyzed Heck Reactions. *Eur. J. Org. Chem.* **2006**, *2006* (22), 5099–5102. https://doi.org/10.1002/ejoc.200600561.

(81) Schneider, C. A.; Rasband, W. S.; Eliceiri, K. W. NIH Image to ImageJ: 25 Years of Image Analysis. *Nat. Methods* **2012**, *9* (7), 671–675. https://doi.org/10.1038/nmeth.2089.

(82) SasView. SasView https://sasview.github.io/ (accessed Mar 13, 2020).